August 2017

Continuum Models of Collective Migration in Living Tissues

Kazage J. Christophe Utuje
Syracuse University

Abstract

This dissertation investigates the physical mechanics of collective cell migration in monolayers of epithelial cells. Coordinated cell motion underlies a number of biological processes, including wound healing, morphogenesis and cancer metastasis, and is controlled by the interplay of single cell motility, cell-cell adhesions, cell-substrate interaction, and cell contractility modulated by the acto-myosin cytoskeleton. Here we examine the competing roles of these mechanisms via a continuum model of a tissue as an active elastic medium, where mechanical deformations are coupled to and feed back onto chemical signaling.

We begin in Chapter 1 with a brief review of cell migration at both the single-cell and many-cell levels, and of the experimental tools used to probe the mechanical properties of cells and tissues. In Chapter 2 we formulate our minimal continuum model of a tissue as an overdamped active elastic medium on a frictional substrate. The model couples mechanical deformations in the tissue to myosin-based contractile activity and to cell polarization. Two new ingredients of our model are: (i) a feedback between the on-off dynamics of myosin motors and the active contractile stresses they induce in the tissue, and (ii) the coupling of cell directed motion or polarization to tissue strain. In the following two chapters we employ this model to describe collective cell dynamics in expanding (Chapter 3) and confined (Chapter 4) tissues and compare with experiments. In expanding monolayers, as realized for instance in wound healing assays where an initially confined tissue is allowed to expand freely on a substrate, our model reproduces the propagating waves of mechanical stress observed in experiments and believed to play a key role in controlling the transmission of information across the tissue and mediating coordinated cell motion. Combining analytical and numerical work we construct a phase diagram that identifies various dynamical regimes in terms of single-cell properties, such as contractility and stiffness. In Chapter 4, we use our model to describe collective dynamics of cells confined to a circular geometry. In this case the propagating waves are replaced by standing sloshing waves guided by both contractility and polarization. The work on confined tissues was carried out in collaboration with the experimental group of Jeff Fredberg at the Harvard School of Public Health. By combining theory and experiment we can provide a quantitative understanding of how contractility and polarization regulate the mechanics of the tissue by renormalizing the tissue elastic moduli and controlling the frequency of oscillatory modes.

Continuum Models of Collective Migration in Living Tissues

by

Kazage J. Christophe Utuje

B.S., National University of Rwanda, 2008

DISSERTATION

Submitted in partial fulfillment of the requirements for the degree of
Doctor of Philosophy in Physics

Syracuse University
August 2017

Acknowledgements

The present work, the result of a period of labour and patience, would not be what it is today without the involvement of all of those, who in a way or another contributed their valuable assistance to lead it to the end.

First and foremost I would like to offer my sincerest gratitude to my advisor Prof. M. Cristina Marchetti who introduced me to the topic of soft condensed matter physics and patiently guided me through my graduate student years. I heartily express my profound appreciation to Prof. Msarchetti and the Physics Department for the amazing opportunity they offered to me and their incessant support through my Ph.D program. A very special gratitude goes to Dr. Shiladitya Banerjee who mentored me through my program and contributed to the completion of my project. I am grateful to my dissertation committee - Profs. Teng Zhang, Jennifer M. Schwarz, Alan Middleton, Matthew LaHaye and Joseph D Paulsen - for taking time out of their busy schedule to critically read my dissertation. I am also very grateful to Prof. J. J. Fredberg and the members of his lab for their contribution to Chapter 4 of this dissertation.

A very special thanks goes to my friends for all the good times and interesting conversations, specially Forrest Smith, Nathan Jurik, Adam Patch, Prashant Mishra and David Mayett. To the members of Prof. Marchetti Research Group and other graduate students and post docs in the Physics Department who made my stay at Syracuse most enjoyable, I express my profound gratitude. Last but certainly not least, I would like to express my special gratitude to my siblings for their unconditional love, endless support and encouragement. I am deeply indebted to them.

Dedicated to my late parents and my late brother

Contents

List of Figures

Chapter 1

Introduction

1.1 Scope

Many developmental processes, such as morphogenesis [8], embryogenesis [9], wound healing [10] and cancer metastasis [11], involve collective cell migration [12] and long-range force generation, which in turn arise from the interplay of cell-cell interaction, cell adhesion to the extracellular matrix, and myosin based contractility [13, 14]. A complete understanding of the mechanisms through which cells coordinate their motion is still lacking. Consequently, many theoretical and experimental studies have been conducted to understand the subject [7, 15–18]. Both biochemical signaling and the transmission of mechanical forces among cells and of cells with their surroundings are key in governing collective migration, but their relative role is not well understood.

The physical properties of individual cells have been studied for some time. Key in controlling both a cell's mechanical behavior and its motility is the cell cytoskeleton, a network of long filamentary proteins crosslinked by molecular motor proteins that use energy derived from adenosine triphosphate (ATP) hydrolysis to perform mechanical work on cytoskeletal filaments [19, 20]. Motor activity regulates the spontaneous contractility of individual cells and their adaptive response to mechanical forces. It also controls the ability of cells to move on substrates or through extracellular matrix.

When individual cells assemble into tissues their mechanical properties change significantly. Measurements of cultured epithelial cell monolayers (one-cell-thick layers of tissue) have shown for example that the monolayer stiffness (20 ± 2kPa) can be two orders of magnitude larger than the stiffness of its individual cells [21]. The stiffness, or rigidity, of a material is defined as its resistance to deformations in response to an applied force. In dense tissues cells often coordinate their motion as seen in the coherent

expansion of epithelial tissues to fill a wound. But what are the mechanisms through which cells communicate to coordinate their motion? The larger stiffness of tissues as compared to isolated cells may be due to intercellular adhesions by mediated-cadherins, a family of calcium-dependent adhesion proteins responsible for cell-cell interaction in tissues. Although experiments have given insight in what happens inside a tissue as it expands, it remains unclear if a tissue should be regarded as an active fluid or an active contractile elastic medium. For instance, recent experiments have shown that during tissue expansion cellular stress and cellular strain tend to be in phase [7], which suggests that a tissue behaves as an elastic medium. In other instances, experiments have shown that cells continuously exchange neighbors, which gives fluid-like properties to tissues [22], and some authors have modeled tissues as fluids [15]. In my work, tissues are modeled as elastic materials. Another observation reported in wound healing assays [7] is that that during unconstrained monolayer expansion the tissue supports waves propagations that build-up intercellular stresses. Mechanical waves such as sound waves arise from the interplay of inertia and elasticity, but a tissue constitutes an overdamped medium (the inertia of cells is negligible). It is surprising to observe propagating stress waves in an overdamped medium, which poses a fundamental physical question: how do mechanical waves arise in overdamped active media? In this dissertation, I propose a minimal physical model of tissues as active elastic media that explains the emergence of mechanical waves and other experimentally observed properties of living tissues.

1.2 Mechanical Properties of Cells and Tissues

All living organisms are made up of cells as basic building blocks. Cells are divided into two main groups; those with a nucleus (eukaryotic cells, e.g., animal and plant cells) and those without it (prokaryotic cells, e.g., bacteria). Typical animal cells, which are the focus of this dissertation, are made up of a nucleus and a cytoplasm (See Fig. 1.1). The nucleus contains chromosomes which carry the cell's genes. The cytoplasm is surrounded by a plasma membrane which separates the cell from its surroundings. The plasma membrane is a fluid lipid bilayer crossed by many large proteins that control transport in and out of the cell. Underneath this is the cortical actin network, a dynamical network of crosslinked actin filaments that forms a polymer gel and is the main player in controlling cell mechanics and in providing stability to cells. The cytoplasm also contains other filamentary proteins namely microtubules and intermediate filaments, briefly discussed in Section 1.2.1. The cytoplasm includes also the endoplasmic reticulum (ER) where ribosome molecules produce proteins, and mitochondria where ATP, source of energy, is produced [20, 23].

1.2.1 Cytoskeleton

The cytoskeleton is a network of filamentary proteins that forms a scaffold within the cell and serves a number of important functions, such as mediating the transport of intracellular cargo, controlling the cell's shape and its resistance to deformations [24]. It is a cross-linked polymer gel made of semi-flexible filaments. In general any semi-flexible polymer can be characterized by a basic mechanical property quantifying its stiffness, called persistence length. The persistence length of a polymer is the distance along which the polymer's direction persists before changing its orientation [25]. Filaments with persistence length large compared to their overall length are considered rigid, while those with smaller persistence length are flexible. Three cytoskeletal filaments, namely actin filaments (also called F-actin), microtubules and intermediate filaments (Fig 1.1), are the main constituents of the cytoskeleton and responsible for the cell's mechanical properties. Microtubules are the most rigid of the cytoskeletal filaments, with a persis-

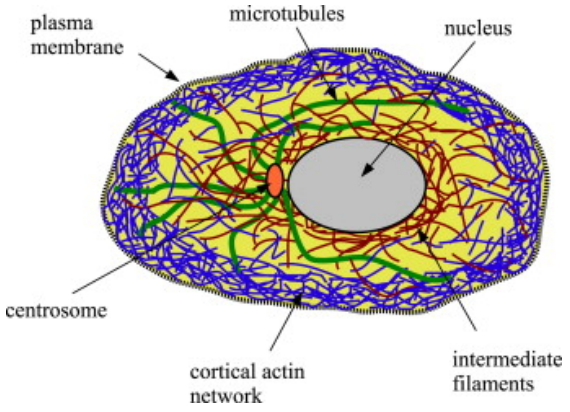

FIGURE 1.1: Schematic of a eukariotic cell's cytoskeletal filaments with actin labeled blue, microtubule in green and intermediate filaments in red [1].

tence length of the order of $1mm$. Their role in controlling the mechanical properties of the cell is not as important as that of the highly crosslinked actin gel, but play a key role in regulating cell division [1]. The intermediate filaments are the most flexible with persistence length of the order of $1\mu m$. They play an important role in regulating cell shape, especially in epithelial cells which have to resist high elastic stresses [1]. Actin proteins are one of the most abundant proteins in eukaryotic cells and form actin filaments [2]. Actin filaments are the thinnest among the cytoskeletal filaments and have a persistence length of the order of the cell size $\sim 17\mu m$ [26]. Actin filaments can be crosslinked by various passive proteins (e.g., $\alpha-$actinins and filamins) which can enhance the elasticity of the network even at low concentraction [1, 27, 28]. Cytoskeletal filaments are additionally cross-linked by motor proteins. There are three main classes of active cytoskeletal motor proteins: myosin motors, kinesins and dyneins. They form

temporary cross-links between cytoskeletal filaments and control most of the mechanical processes in the cytoskeleton. Kinesin and dynein motors bind to microtubule. Ksinesins walk along microtubules to move cargos inside the cell away from nucleus, while dyneins walk along microtubules to move cargos towards the cell nucleus. The association of microtubule filaments with these protein motors play an important role during cell division [24]. Myosin motors bind to actin filaments to form the actomyosin network which generates active intracellular stresses and leads to cell motility and resistance to cellular deformations. The actomyosin network is located at the periphery of the cytoskeleton (Fig. 1.1) and is called the cortex. Cortical tension, which is a tension in the cortex that tends to minimize the cell surface area by pulling it into a spherical shape, depends largely on actomyosin contraction [29–32], on the density of the cortex and on its structure [29, 33, 34]. The contraction of actomyosin filaments in the cortex also creates intracellular pressure [35]. Recent experiments show that actomyosin complexes increase cortical tension and intracellular pressure and stiffen the cortex, while crosslinked actin networks decrease cortical tension and intracellular pressure and soften the cortex [36]. For simplicity, our model focuses on the actomyosin network as responsible for the cellular mechanical properties. Cross-linked actomyosin networks have been studied extensively *in vitro* as models for the cell cytoskeleton [37]. Their elasticity, i.e, shear stiffening, can arise either when thermally fluctuating filaments do not have enough available configurations, for example when they are stretched (entropic elasticity), or when the space between molecules that make up the filaments changes, for example when they are bent (enthalpic elasticity) [24]. Applying shear stresses to the actin filament networks or to networks of intermediate filaments increases the networks stiffness and generates resistance to additional deformations [38]. Applying compressive forces to actin filament networks results in nonlinear stress stiffening of the network followed by stress softening at high stresses [39].

1.2.2 Measuring Mechanical Properties of Living Cells

The mechanical properties of a cell are extremely rich. A living cell is a soft highly heterogeneous object, with stiffness controlled by the cytoskeletal structure [40], myosin activity [41] and other subcellular processes. It has been found that changes in cell mechanical properties can lead to various disease conditions, such as tumor formation and metastasis [42–44]. Understanding and measuring mechanical cell properties such as stiffness can then provide a novel way to detect and diagnose diseases [42] and to optimize the effectiveness of drug treatment [45, 46].

Cell mechanics is determined by both the elasticity of the passive actin network and the active forces induced by myosins. Cells adhering to a substrate carry a finite tensile stress even without the application of an external load. This is known as prestress and it arises from the active contractile forces exerted by myosin motors. It controls the ability of cells to retain their shape and their (often nonlinear) response to external deformations (e.g., strain stiffening). Due to the presence of prestress and the heterogeneity of the cell interior, quantifying the mechanical properties of cells as a material has proven to be difficult and requires a combination of a variety of techniques. Multiple techniques have been developed over the past decades to measure the cell mechanical properties. These techniques can be divided into two groups: techniques that measure *local* elastic properties and those that measure the elasticity of the cell *as a whole*. The latter techniques are problematic because cells are neither homogeneous nor isotropic and they are active.
The techniques that probe the local mechanical properties of cells include:

Atomic Force Microscopy **(AFM).** AFM uses a microscale tip connected to a cantilever beam to deform and interact with a sample (Fig. 1.2a) [2]. It can probe the viscoelastic response of a cell by applying indentations of about 50 nm and forces in the range of 0.1-1 nN [47–51]. The most used AFM technique is the AFM Force Spec-

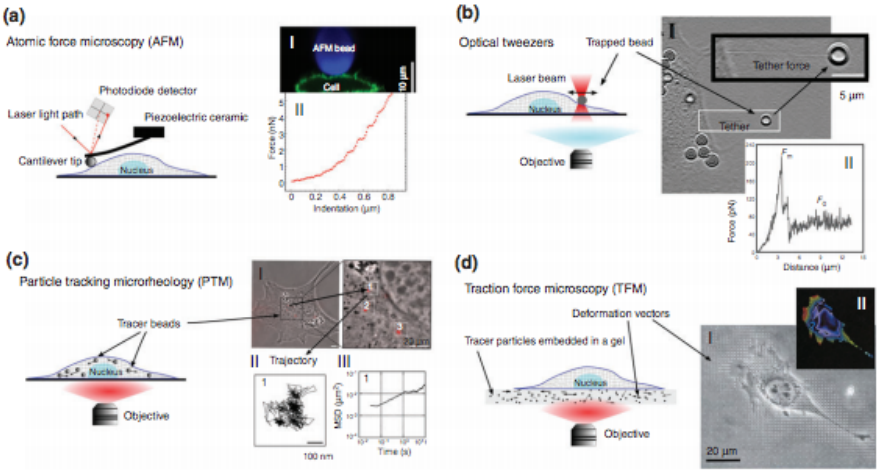

FIGURE 1.2: Different techniques to measure cell mechanical properties. (a) Atomic Force Microscopy. Indentation model is used to estimate cell elasticity. (b) Optical Tweezers. A bead is deformed optically and manipulated with a light source. (c)Particle Tracking Microrheology. Mechanical measurement inside cytoplasm is achieved by tracking embedded tracer particles. (d) Traction Force Microscopy. Cellular traction forces are calculated from the bead displacement [2].

troscope which measures the cell elasticity by pressing the tip of the AFM cantilever against the cell. Elasticity is calculated by comparing the measured forces to indentation

data [52].

Other techniques rely on deformation or displacement of beads placed in cells. They include:

Optical Tweezers. The technique of optical tweezers (Fig. 1.2b) is another technique used often in biology to measure forces of order of piconewtons generated by myosin motors or to measure the local mechanical properties of cell organelles [53–55]. Using optical tweezers, a cell is deformed by attaching a pair of beads at the two endpoints of the cell and pulling on the beads by means of laser traps. The cell stiffness can be determined by following the Brownian motion of the beads in the trap.

Particle Tracking Microrheology **(PTM).** PTM is another passive technique used to extract local viscoelastic parameters by tracking the random Brownian motion of organelles or of microparticles injected in the cell [56–58]. At least two beads are tracked simultaneously (Fig. 1.2c) in order to measure intracellular stress fluctuations [1, 59]. Elastic and viscous properties of the cell are calculated from the beads displacement by means of the fluctuation-dissipation theorem [60, 61]. One of the problems of this technique is that like any other Brownian motion based technique it can be biased by active intracellular processes that maintain the cell out-of-equilibrium, and is more reliable when used for cells that have been depleted of ATP i.e, dead cells [61].

All these techniques, and many others not mentioned here, provide results that consistently show that the cell is a viscoelastic material. At very short timescales (from fractions of a second to several tens of seconds), the cell is predominantly an elastic material [60, 62]. At longer timescales ($>$ 30 seconds), remodeling [63] leads to additional relaxation [47, 64]. Some active response, such as change in cell stiffness and contractility, is generated over timescales of seconds to tens of seconds as a result of external forces applied to cells [65, 66]. To understand these active viscoelastic responses comprehensive theoretical models which account for all components contributing to cell mechanics are needed.

Recent experiments have shown that cells stiffen when they are stretched [67], in agreement with earlier experiments which related cell elasticity to internally generated prestress [68]. These observations suggest that cell elastic behavior might be determined by cytoskeletal prestress. Techniques used to probe the whole cell mechanical properties and the prestress include:

Traction Force Microscopy **(TFM).** TFM measures traction forces exerted by the cell on the substrate by probing the deformations induced on micropillar arrays [69] or soft gels (Fig. 1.2d). It is used to determine the prestress in the cytoskeleton. It provides a powerful tool to extract intracellular forces. It relies on force balance and it has shown that the properties of the substrate affect the prestress [70]. On an inverted optical microscope, cell-generated displacements of fluorescent markers previously embedded near the surface of the substrate, are recorded. Then using Fourier Transform of the equilibrium equation for displacement field traction force are obtained from the displacements. The solution of traction forces are the inverse of the classical Boussinesq forward solution which gives displacement field in function of traction forces. In this technique, the displacements induced by the cell on the substrate are measured by comparing images of fluorescent microbeads embedded in the substrate in the undeformed and deformed configurations. Assuming that the substrate is a linear elastic medium one then calculates the traction forces that the cell must exert to generate such displacements. Upon finding the traction forces, the cell-substrate equilibrium equations are used to determine the stresses in cell.

*Optical Stretcher***.** Optical stretcher is another technique used to measure the whole cell mechanical properties. It uses a double beam trap in which two identical and opposite laser beams trap a cell in the middle without any physical contact with the device [71]. It uses the principle of conservation of momentum where momentum from the beam is transferred at the cell interface and, by Newton's second law, a force is exerted on the interface. Image analysis is used to determine the cell deformation and extract mechanical properties by dividing the applied force by the deformation.

1.3 Cell Migration

Cell motility is a phenomenon that is essential to many biological processes such as morphogenesis, wound healing or immune response. In this section we describe two different kinds of cell migration. The first part is devoted to single cell migrating in isolation. The second part is devoted to collective cell migration. Cells can move in isolation for example when fibroblasts (cells that synthesize collagen, the structural framework of animal tissues) pass through connective tissues or when leukocytes (white blood cells) move during immune response [72]. Cells move collectively for example in wound healing or cancer metastasis.

1.3.1 Single Cell Motility

The migration of individul cells has been a subject of extensive studies over many decades[73–75]. In brief, a typical cell motion on a substrate follows the steps shown in Fig. 1.3: the cell expands by making protrusions at the leading edge. These protrusions are generally driven by actin polymerization, a process by which actin filament monomers assemble to form an elongated actin filament. Next, the cell adheres its leading edge to the surface on which it is moving and then exerts a pulling force which translocates the cell body forward and de-adheres at its rear [3, 16]. Cell adhesion to the substrate is facilitated by large macromolecular assemblies called focal adhesions through which chemical signals and mechanical forces are transmitted between the cell and the substrate. The focal adhesions are collection of protein receptors called integrins which are linked to the actomyosin network in the cytoskeletal cortex. These integrins form a mechanical linkage between the cytoskeleton and the substrate.

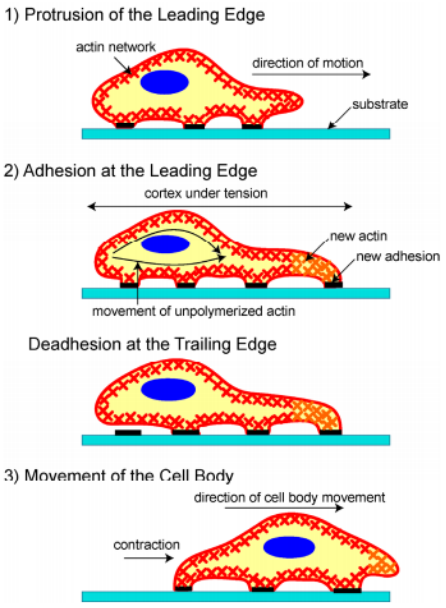

FIGURE 1.3: A schematic of the stages of cell motility. Protrusion at the leading edge due to actin polymerization, followed by adhesion of the protruded edge on the surface of motion, followed by movement of the cell body [3].

A cell starts moving in response to an external signal (physical, chemical, diffusible or not diffusible) in its environment. Integrins, located on the cell membrane, detect the signal and transmit it to the cell interior [20]. Integrins also plays a role in regulating cell polarization during directional motion by controlling the protrusions that are formed at the leading edge. The cell polarization is realized through the formation of front and back ends as the cell moves [76]. As the cell continues to move, the actin cytoskeleton transitions in a cyclic fashion between a solid-like material (gel) and a viscous material (sol) [3]. These gel-sol transitions are crucial for cell motility [77]. They are likely

due to a net constant actin polymerization (depolymerization) and network assembly (disassembly) at the leading edge (at the rear edge). These transitions may be also driven by myosin motors[78].

1.3.2 Collective Cell Migration

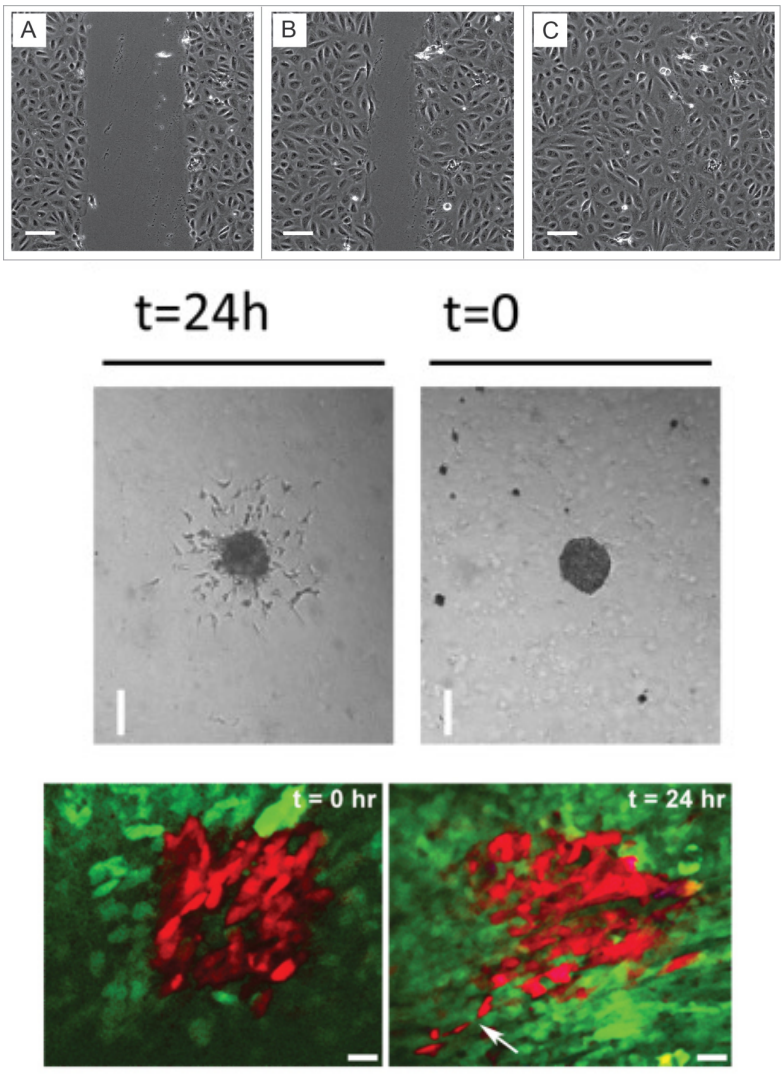

FIGURE 1.4: Top: A sequence of representative images from a wound healing assay of endothelial cells from initial time (A) where the gap is large, several hours later (B), the gap narrows and ultimately closes (C) [4]. Middle: Lymphatic endothelial cells in spheroid sprouting assay, where the initial spheroid (0hr) and the spheroid at the end of the assay (24hrs) are shown [5]. Note that in this figure, the direction of spheroid invasion is from right to left. Bottom: Streaming assay of carcinoma cells. The white arrow shows carcinoma cells (red image) in a stream. The initial stream (0hr) and stream at the end of the assay (24hrs) are shown [6].

In many biological processes such as wound healing, cancer invasion and morphogenesis, cells move in a coordinated manner[8, 9, 17, 79, 80]. There are many categories of collective cell migration. In epithelial sheet migration (Fig. 1.4, top frame), cells maintain

close contact and continuity and move as a single sheet. This sheet movement occurs in physiological processes such as wound healing, dorsal closure in Drosophila and early morphogenesis [4, 81–83]. Other types of collective cell migration include sprouting and

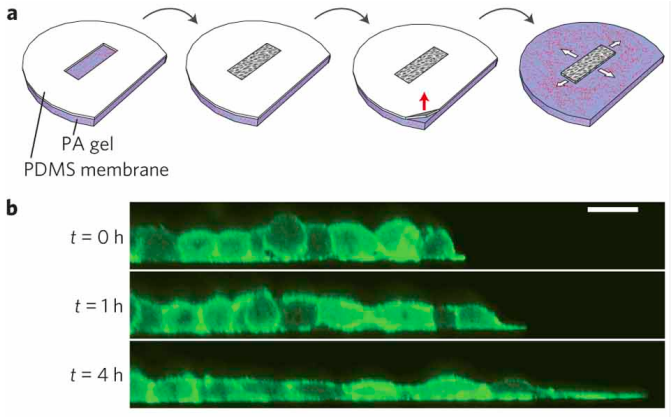

FIGURE 1.5: (a) A PDMS membrane is deposited on a collagen-coated PA substrate, Cells are cultured allowed to attach and move upon confluence. (b) Transversal View of MDCK cells during tissue expansion [7].

branching (Fig. 1.4, middle frame), characterized by a tip cell or leading sprout which maintains connection to other cells [5, 16], and streams (Fig. 1.4, bottom frame) where cells move together but in loose arrangement[6, 16, 84]. In this dissertation, unless otherwise specified, collective cell migration will refer to sheet migration. Traditional assays for studying collective cell migration rely on tissue culture where cells are plated on a substrate and their motility is observed and analyzed (Fig. 1.5). In [7] for example, the authors studied the dynamics of epithelial cell expansion by developing an experimental approach combining soft lithography, traction force microscopy and Particle Image Velocimetry (PIV). This approach relies on preparing the substrate on which the cells will be cultured, then tracks the cellular layer expansion and measures the intercellular stresses. A now popular wound healing assay for studying the dynamics of an expanding epithelial sheet was developed in the lab of Pascal Silberzan [83]. It consists of fabricating a polydimethylsiloxane (PDMS) membrane with a rectangular opening in it. The membrane is then deposited on a collagen coated-polyacrylamide (PA) gel substrate (Fig. 1.5a, far left frame). Cells (in this case Madin-Darby Canine Kidney (MDCK) epithelial) are then cultured in the hole on the PA substrate (Fig. 1.5a, second left frame). After the opening is fully covered by cells (confluence), the PDMS mask is removed to allow cells to expand (Fig. 1.5a, second right, and far right frame). Cells move collectively as one epithelial sheet (Fig. 1.5b). Using Traction Force Microscopy described in Section 1.2.2, monolayer stresses can be measured. The midline stresses oscillates in phase with fluctuations in cell area, which determines the cellular strain, showing that the epithelial monolayer behaves as an elastic medium. From the cellular strain, the authors in [7] computed the strain rate which exhibited mechanical waves

propagating away from and back to the leading edge in X-shape. The cellular velocity can be determined by means of Particle Image Velocimetry (PIV), a technique where cell displacements are determined by means of image analysis and the time intervals between images are recorded. The time interval and the displacement field give the cellular velocity. In these particular experiments, one of the most interesting discoveries was the observation of mechanical waves that propagate within the monolayer as the latter expands [7]. Many experimental findings show that in cohesive cell layers, stress and strain tend to be in phase, as in elastic materials [7, 13] and the active tension of a cell monolayer scales linearly with the size of the constituent cells. One can extract the active tensile modulus from the slope of this relationship [85]. Besides experimental models, there are theoretical models that study collective cell migration. They are reviewed in Chapter 2.

1.4 Outline

In this dissertation we develop continuum models of migrating cell monolayers and use them to describe quantitatively experimental observations. We show that the deformation of the cell layer, described as an elastic medium coupled to the myosin based cell contractility, can account for mechanical waves observed in monolayer during collective migration. The dissertation comprises three main parts. The first part (Chapter 2), formulates a minimal continuum model of collective cell migration. In Chapter 3 we apply the model to expanding cell monolayers and demonstrate that the model accounts for the propagating mechanical waves observed in these systems. In Chapter 4 we apply the same model to the case of confined cell monolayers, where confinement yields standing waves of cellular stress.

Chapter 2

Mechanochemical Model of Collective Cell Migration

2.1 Introduction

Recent experiments have revealed that (a) during collective cell migration oscillating waves of mechanical stress arise spontaneously and propagate through the layer in spite of strong frictional damping [7], and (b) as cells move the direction of their velocity deviates systematically from the direction of the traction force cells exert on the substrate [86]. Motivated by these observations we have developed a simple yet rich dynamical model of epithelial tissues as active gels. This model can describe both expanding and confined cell monolayers. In this chapter we will introduce the model. The implementation of the model to describe the dynamics of expanding cell monolayers as relevant to wound healing assays is discussed in Chapter 3. Chapter 4 is reserved to the application of the model to a confined cell monolayer.

In our model we propose a theory that connects forces and motions using two internal state variables, one of which describes an effective cellular polarization, and the other an effective cellular inertia that arises from the on/off dynamics of motor proteins that drive cell contractility. This simple mechanochemical interaction allows us to capture the experimentally observed propagating stress waves during collective cell motion. There are other models that have been developed in order to study this very phenomenon of collective cell migration. The comparison with previous work is discussed in Section 2.4

2.2 Cell Layer as an Active Elastic Medium

We consider a cell monolayer extending on a substrate in the x-y plane. We model the cell layer as an continuum elastic sheet of extents L and d in the x and y directions, respectively, and thickness $h \ll L, d$, as shown in Fig. 2.1. The assumption of elasticity of the cell monolayer is supported by experimental evidence that in cohesive cell layers stress and strain tend to be in phase (See Fig. 2.2, top frame), as they are in elastic materials [7, 13, 85]. In the absence of external forces, force balance gives,

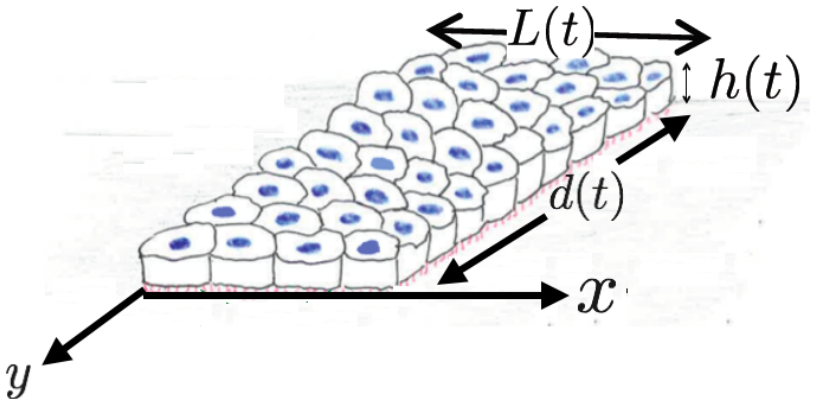

FIGURE 2.1: A schematic of a cell monolayer, with height $h(t)$, length $L(t)$ and width $d(t)$.

$$\partial_j \Sigma_{ij} + \partial_z \Sigma_{iz} = 0 \ , \tag{2.1}$$

where Σ_{ij} is the stress tensor of the tissue and Latin indices denote in-plane coordinates x and y. For $h \ll L, d$, we average the force balance equation across the thickness of the layer, assuming that the top surface of the monolayer at $z = h$ is stress free, i.e. $\Sigma_{iz}|_{z=h} = 0$. This gives,

$$h \partial_j \sigma_{ij} = \Sigma_{iz}|_{z=0}, \tag{2.2}$$

where

$$\sigma_{ij}(x, y) = \frac{1}{h} \int_0^h dz \ \Sigma_{ij}(x, y, z), \tag{2.3}$$

is the thickness-averaged stress tensor of the monolayer. The shear stress at the cell-substrate interface, $\Sigma_{iz}|_{z=h}$, is the traction force T_i exerted by the cell on the substrate, which is measured in TFM experiments. This gives us the following relation between monolayer stress and traction,

$$T_i = h \partial_j \sigma_{ij} \ . \tag{2.4}$$

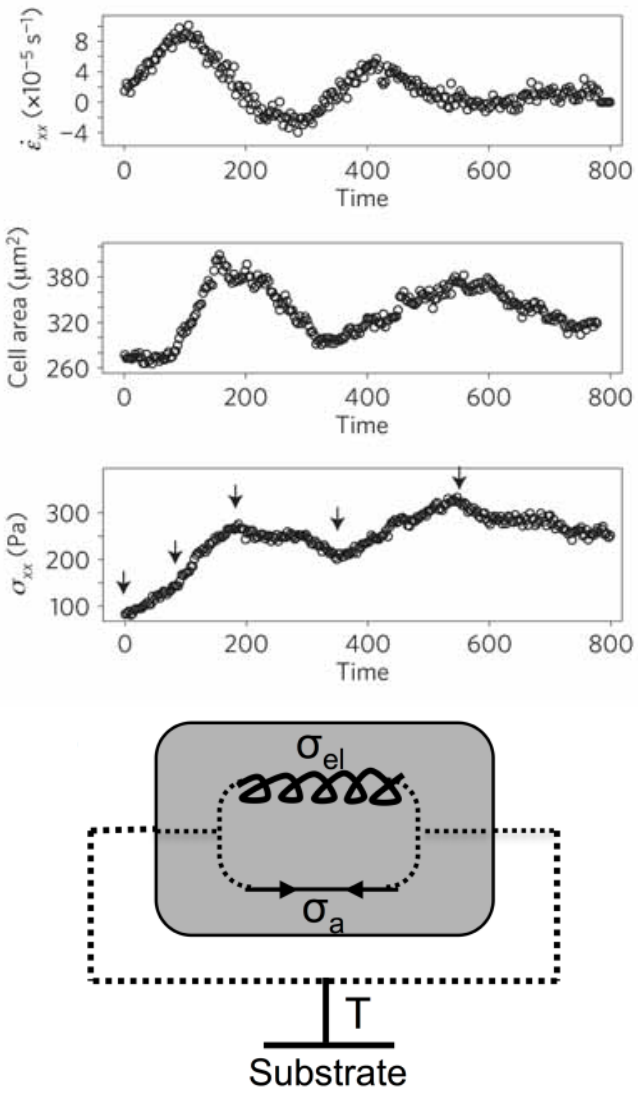

FIGURE 2.2: Top: Average values of strain rate (Top), cell area (Middle) and cellular stress (Bottom) at the midline of the cell monolayer [7]. The cellular oscillations of the monolayer stress at the midline are in phase with fluctuations of cell area (proportional to strain) and out of phase with strain rate, suggesting that on the timescale of cell layer migration, elastic cellular stresses are dominant. Bottom: Constitutive elements of the mechanochemical model. The elastic and active elements exert stresses in parallel, and a local gradient in stress is balanced by the traction exerted by the cell on the substrate.

The monolayer stress tensor is given by the sum of passive elastic and active stresses, corresponding to a situation where elastic and active contractile elements are connected in parallel, as shown in Fig. 2.2, bottom frame,

$$\sigma_{ij} = \sigma_{ij}^{\mathrm{el}} + \sigma_{ij}^{\mathrm{a}} \, . \tag{2.5}$$

Here $\sigma_{ij}^{\mathrm{el}}$ is the stress tensor of a passive linear elastic material [87]. We neglect, for simplicity, nonlinear elasticity of the monolayer [18] and assume that the passive stress is isotropic and homogeneous. The active stress σ_{ij}^{a} arises mainly from forces that myosin

motors exert on actin filaments. We describe both the active and passive contributions of the total cellular stresses in the section below.

2.3 Continuum Mechanochemical Model

We model the tissue as an elastic active gel described in terms of a displacement field, $\mathbf{u}(\mathbf{r}, t)$, characterizing local deformations. The elastic (passive) component of the stress is then given by,

$$\sigma_{ij}^{\mathrm{el}} = B\varepsilon_{kk}\delta_{ij} + 2G\left(\varepsilon_{ij} - \frac{1}{2}\delta_{ij}\varepsilon_{kk}\right) \ . \tag{2.6}$$

where B and G are, respectively, the in-plane bulk and shear elastic moduli of the monolayer, ε_{ij} the symmetrized strain tensor,

$$\varepsilon_{ij} = \frac{1}{2}\left(\partial_i u_j + \partial_j u_i\right) \ . \tag{2.7}$$

and δ_{ij} the Kronecker delta.

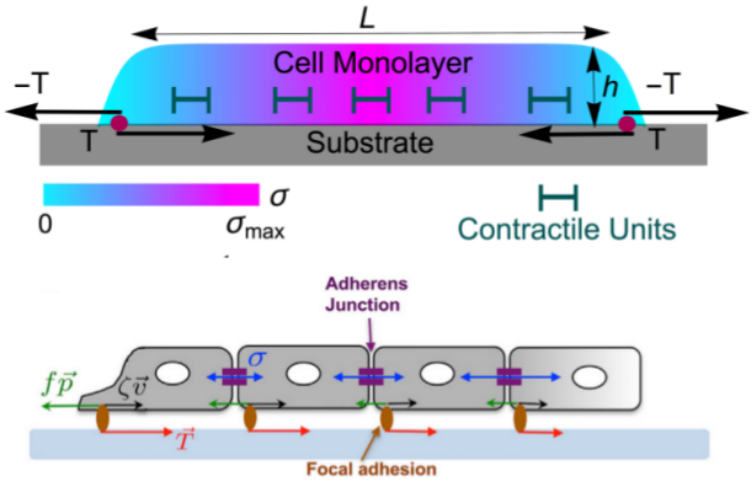

FIGURE 2.3: Top: Schematic of a spreading cell monolayer. Traction stresses ($\mathbf{T}$) are indicated by arrows and the color map denotes local magnitude of monolayer stress. Active stresses are generated by contractile units. Bottom: Schematic of the forces acting on the cell monolayer. Tractions exerted by the monolayer on the substrate point inward (red arrows) at the monolayer edge and balance the forces due to viscous friction, $\zeta\mathbf{v}$ (black arrows), and propulson $f\mathbf{p}$ (green arrows). The monolayer is in mechanical equilibrium, such that the tractions are locally balanced by the divergence of the monolayer stress, $T_i = h\partial_j\sigma_{ij}$.

Cells exert forces on substrates through the action of focal adhesion complexes (Fig. 2.3) that have their own on/off dynamics. The simplest description of the resulting strong frictional effect is then obtained by writing $\mathbf{T} = \zeta\mathbf{v}$, where $\mathbf{v} = \partial_t\mathbf{u}$ is the local velocity of the monolayer. This would yield $\zeta v_i = h\partial_j\sigma_{ij}$. However, experiments show that local

cell traction is often not aligned with local cell velocity [88], indicating that there must be an additional internal driving force in the equation of motion for the monolayer. This motivates the introduction of a cell polarization field $\mathbf{p}(\mathbf{r}, t)$. The magnitude of $\mathbf{p}$ describes the local degree of polarization in the cell monolayer, whereas its orientation defines the local direction of the propulsive thrust internally generated by each cell through its adhesion to the substrate (Fig. 2.3, bottom frame) [18, 89, 90]. The local traction $\mathbf{T}(\mathbf{r}, t)$ exerted by the cell layer on the substrate is then written as the difference between the viscous friction and the thrust,

$$\mathbf{T} = \zeta \partial_t \mathbf{u} - f\mathbf{p} \ , \tag{2.8}$$

where ζ describes viscous friction with the substrate and f is the strength of the coupling between cell polarization and thrust (Fig. 2.3, bottom frame). Both ζ and f are controlled by integrin-mediated cell-environment interactions. Combining Eqs.(2.4) and (2.8), we get the thickness-averaged dynamics of the cellular deformation field $\mathbf{u}(\mathbf{r}, t)$ given by,

$$\zeta \partial_t u_i = f p_i + h \partial_j \sigma_{ij} \ . \tag{2.9}$$

In order to close Eq. (2.9) we still need a constitutive equation for the active stress, σ^a_{ij}. Active stresses arise because the actin cytoskeleton is driven out of equilibrium by the action of myosin motors, such as myosin-II, which convert the chemical energy produced during ATP hydrolysis into mechanical work via a cycle of attachment/detachment processes to F-actin filaments. Hence ATP hydrolysis drives both actomyosin contractility and treadmilling of actin filaments. Retaining terms to lowest order in the gradients, the active stress is given by [91]

$$\sigma^a_{ij} = \beta \Delta\mu \delta_{ij} + \beta_1 \Delta\mu \ p_i p_j + \beta_2 \boldsymbol{\nabla} \cdot \mathbf{p} \ \delta_{ij} + \frac{\beta_3}{2} \left(\partial_i p_j + \partial_j p_i \right) \ , \tag{2.10}$$

where $\Delta\mu$ is the chemical potential difference between ATP and its products and β, β_1, β_2 and β_3 are microscopic parameters. The parameters β_2 and β_3 also depend on the chemical potential difference $\Delta\mu$. The term proportional to $\beta > 0$ describes the isotropic part of the contractile stress exerted by actomyosin units. This corresponds to a sort of 'negative pressure' that yields spontaneous contraction of cellular material. The terms proportional to β_2 and β_3 describe tensions induced by local gradients in the polarization field. The term proportional to β_1 is the material anisotropic part of the active stress. We will neglect it in the following where we assume that the monolayer is an isotropic material. The assumption of isotropic stress is consistent with the stress field measured in experiments using monolayer stress microscopy [88]. The principal stress analysis of experimental data in [88] reveals that the stress ellipses in the monolayer (See Fig. 2.4c)

typically have low aspect ratio with a quotient of maximum shear to tension less than 0.2 (Fig. 2.4d).

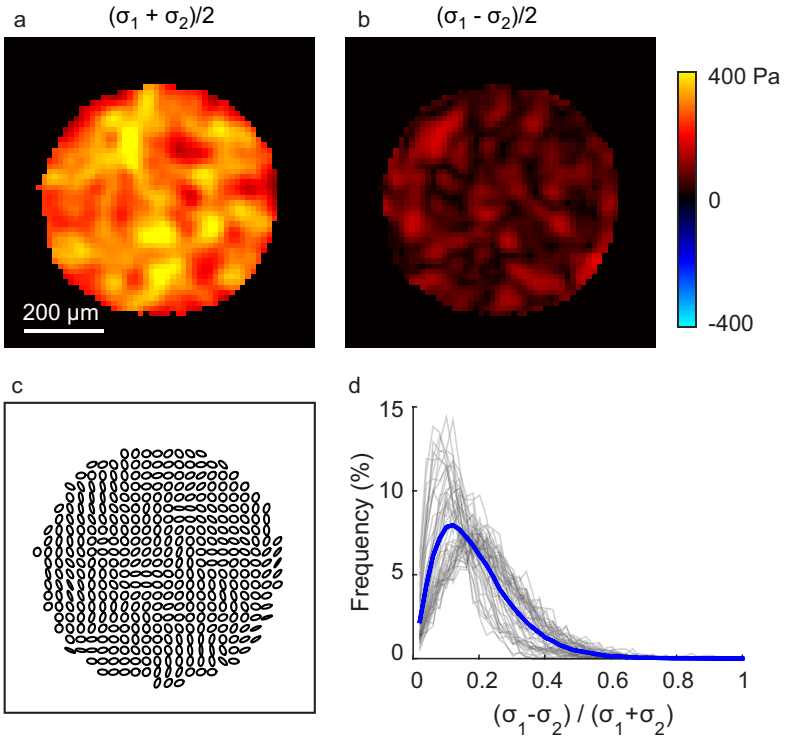

FIGURE 2.4: The stress tensor within the circular monolayers is isotropic. The first and second principal stresses, σ_1 and σ_2, are computed. (a, b) Representative plots of (a) the mean principal stress, $(\sigma_1+\sigma_2)/2$ and (b) the maximum shear stress, $(\sigma_1-\sigma_2)/2$ for a circular monolayer at one point in time. (c) Visualization of the stress tensor in the monolayer where the major and minor axes of each ellipse correspond to the magnitude of σ_1 and σ_2, and the orientation of the major axis corresponds to the orientation of the first principal stress σ_1. (d) As a measure of stress isotropy, the difference in the principal stresses is divided by the sum of the principal stresses with a value of zero indicating a fully isotropic state. Histograms of $(\sigma_1 - \sigma_2)/(\sigma_1 + \sigma_2)$ are generated for each point in time (gray lines) and for all time points (blue line). The mean and median are <0.2, indicating the stress tensor is nearly isotropic.

The chemical potential difference $\Delta\mu$ is controlled by the concentration of the active units (e.g., phosphorylated myosins), which has been assumed to be constant in much of previous work. Here instead we explicitly consider the dependence of $\Delta\mu$ on the concentration $c(\mathbf{r}, t)$ of active units and treat $c(\mathbf{r}, t)$ as a dynamical variable.

Although we are not aware of any direct measurement of active stress in live cells and their relationships with myosin concentration and chemical potential of ATP, we model the dependence of active stress on concentration on the basis of two simple assumptions. First, we assume that for weak to moderate activity the active stress depends linearly on the chemical potential difference $\Delta\mu$ between ATP and its products. Second, we assume the chemical potential difference is related logarithmically to the concentration

of reactants and products. The logarithmic dependence can be justified as follows. ATP hydrolysis involves conversion of high-energy ATP molecules to ADP and inorganic phosphate P, ATP $\rightarrow$ ADP + P. The change in chemical potential $\Delta\mu$ during ATP hydrolysis is given by the difference in chemical potentials of the reactant and the products as,

$$\Delta\mu = \mu_{\mathrm{ATP}} - \mu_{\mathrm{ADP}} - \mu_{\mathrm{P}} \ . \tag{2.11}$$

Treating the collection of molecules of each species as an ideal gas, the chemical potential of species i is related to the concentration of molecules as $\mu_i = \mu_i^0 + RT \log(c_i)$ where the subscript i represents the molecule type (ATP, ADP or P), R is the universal gas constant, T is the temperature and μ_i^0 is the chemical potential at the standard thermodynamic state [92]. We thus have,

$$\Delta\mu = RT \log\left(\frac{c_{\mathrm{ATP}} c_s}{c_{\mathrm{ADP}} c_{\mathrm{P}}} e^{\Delta\mu_0/RT}\right) \equiv RT \log\left(c_{\mathrm{ATP}}/c^0_{\mathrm{ATP}}\right) , \tag{2.12}$$

where c^0_{ATP} is the ATP concentration in chemical equilibrium given by $c^0_{\mathrm{ATP}} = \frac{c_{\mathrm{ADP}} c_{\mathrm{P}}}{c_s} e^{-\Delta\mu_0/RT}$, with c_s being the standard thermodynamic concentration and $\Delta\mu_0$ the standard change in chemical potential. With this identification, active stresses are generated by molecular motors for $c_{\mathrm{ATP}} > c^0_{\mathrm{ATP}}$. A positive value of $\Delta\mu$ can trigger phosphorylation of myosin light-chain kinase causing myosin-II to assume an extended state, thereby promoting its assembly into bipolar filaments leading to cell contraction [20]. This leads to the assumption that the concentration c_{ATP} of hydrolysed ATP is proportional to the concentration c of phosphorylated myosins. We thus have $\Delta\mu \propto \log(c/c_0)$, where c is the concentration of the active units (e.g. phosphorylated myosins) and c_0 is the equilibrium concentration. Although we could have used a linear dependence of c and still observe propagating waves as the monolayer expands, the linear dependence gives non-physical quantitative values of the active stress. One can argue that linear dependence of the concentration of active units to the active stress does not capture the generation of active stresses by the complex actomyosin network.

The dynamics of the concentration field $c(\mathbf{r}, t)$ is then described by a reaction-advection equation,

$$\partial_t c + \boldsymbol{\nabla} \cdot (c \partial_t \mathbf{u}) = -\frac{1}{\tau}(c - c_0) + D\nabla^2 c + \alpha \varepsilon_{kk} + \alpha' \boldsymbol{\nabla} \cdot \mathbf{p} \ , \tag{2.13}$$

where $\boldsymbol{\nabla} \cdot (c \partial_t \mathbf{u})$ is the convective flux, describing that cell layer motion can change the local concentration of active units, τ is the timescale of turnovers of active units, $\alpha > 0$ and $\alpha' > 0$ are the rates of production of c due to compressive mechanical and polarization strains, respectively, and D is an effective diffusion constant, describing the tendency of

neighboring cells to equalize activity levels. The assumption that $\alpha, \alpha' > 0$ means that a local increase in cell area generates a local increase in c, hence in the contractile stress σ^a. This is in agreement with experimental data on confined cell monolayers [88] and previous results for single cells [93] and multicellular monolayers [85] showing a growth of the active stress with the size of constituent cells.

Finally, the dynamics of the polarization field $\mathbf{p}(\mathbf{r}, t)$ is given by,

$$\partial_t p_i = \left(a - b|\mathbf{p}|^2\right) p_i + \kappa \nabla^2 p_i - w_1 \partial_j \varepsilon_{ij} - w_2 \partial_i \varepsilon_{kk} + w' \partial_i (c/c_0) \ , \tag{2.14}$$

where the first two terms (with $b > 0$) allow for the onset of a homogeneously polar state, $|\mathbf{p}| = \sqrt{b/a}$, when $a > 0$. The local cost of fluctuations in polarization is characterized by an isotropic stiffness κ; w_1, w_2 and w' describe the tendency of cell polarization to align with gradients of elastic strain and concentration, respectively.

We summarize the coupled equations of our model here,

$$\zeta \partial_t u_i = f p_i + h \partial_j \sigma_{ij} \ , \tag{2.15a}$$

$$\partial_t c + \boldsymbol{\nabla} \cdot (c \partial_t \mathbf{u}) = -\frac{1}{\tau}(c - c_0) + D\nabla^2 c + \alpha \varepsilon_{kk} + \alpha' \boldsymbol{\nabla} \cdot \mathbf{p} \ , \tag{2.15b}$$

$$\partial_t p_i = \left(a - b|\mathbf{p}|^2\right) p_i + \kappa \nabla^2 p_i - w_1 \partial_j \varepsilon_{ij} - w_2 \partial_i \varepsilon_{kk} + w' \partial_i (c/c_0) \ . \tag{2.15c}$$

with

$$\sigma_{ij} = \sigma_{ij}^{\mathrm{el}} + \sigma_{ij}^{\mathrm{a}} \tag{2.16}$$

where

$$\sigma_{ij}^{\mathrm{el}} = B \varepsilon_{kk} \delta_{ij} + 2G \left(\varepsilon_{ij} - \frac{1}{2} \delta_{ij} \varepsilon_{kk} \right) \ , \tag{2.17a}$$

$$\sigma_{ij}^{a} = \beta \log(c/c_0) \delta_{ij} + \beta_2 \boldsymbol{\nabla} \cdot \mathbf{p} \ \delta_{ij} + \frac{\beta_3}{2} \left(\partial_i p_j + \partial_j p_i \right) \ . \tag{2.17b}$$

Eqs. (2.15)-(2.17) describe the dynamics of the cell monolayer. This model is applied to the collective cell migration in expanding tissues in Chapter 3 and the collective cell migration in confined tissues in Chapter 4.

2.4 Previous Models of Collective Cell Migration

Various models have been developed to describe collective cell migration. Most can be divided into two groups: models that study collective cell migration by treating cells

as particles [94–97] and models like ours that treat the cell monolayer as a continuum [15, 18, 98–100]. Additionally, early models of epidermal (rather than epithelial) wound healing use reaction-diffusion equation to describe collective migration and proliferation as the response to a diffusive chemical signal generated by the wound [98]. These models cannot capture the measured mechanical forces that expanding monolayers exert on their environments. Mark *et al.* proposed a one dimensional model to describe the finger-like shapes that are observed in some experiments during monolayer expansion [100]. The cell monolayer interface is treated as continuous one-dimensional contour characterized by its curvature and surface tension. This work demonstrates that the feedback between restoring forces and the curvature-induced motility drives a dynamic instability that gives rise to finger-like protrusions qualitatively similar to those seen in some experimental wound healing assays. This model does not, however, describe what happens throughout the cell monolayer since it focuses on the dynamics of the advancing tissue edge. Arciero *et al.* developed a two-dimensional continuum mechanical model of cell migration that takes into account compressional elasticity of the fluid, cell proliferation and cell apoptosis [15]. The cell layer is modeled as a compressible fluid whose bulk modulus depends logarithmically on the cell density. The model reproduces the experimental finding that cell density and cell stress are larger at the center of the tissue. These authors did not, however, investigate the origin of mechanical waves during tissue expansion.

It is especially useful to compare our model to the work by Köpf and Pismen [18] and to that of Lee and Wolgemuth [89]. The model of Ref. [18] is very similar to the one used here. Both models describe a tissue as an active elastic medium in terms of coupled equations for displacement field, polarization, and an internal scalar degree of freedom describing a deformation-induced chemical signal. Our model is a minimal version of that of Ref. [18] where many of the non-essential nonlinearities and anisotropies are ignored. In Ref. [89], in contrast, the authors describe the tissue as a fluid and retain the anisotropic part of the active stress proportional to polarization. Internal dynamics is introduced by assuming that the stress is viscoelastic with dynamics described by a Maxwell model. This has a similar effect to our assumption of relaxational dynamics for the chemical signal that controls the isotropic active stress. Both introduce an additional time scale that provides an effective inertia for the overdamped monolayer, be it a liquid or an elastic medium.

In comparison, our minimal model contains a much smaller number of parameters and yet is capable of validating two main experimental observations that were not to my

knowledge studied in previous theoretical models: (i) During monolayer expansion, mechanical stress waves propagate to span the cell layer. Our model demonstrates that the feedback between deformations of the cell layer and the myosin-based contractility at the cellular level creates an effective inertia that allows these propagating waves. Our model also predicts that the cell layer responds to these propagating waves by undergoing periods of stiffening and softening which have been observed in experiments. (ii) Our model explains that a systematic misalignment between local velocity and local traction, which is evident in confined layer, is due to cell polarization. Our model also predicts the observed standing waves of cellular motion in confined monolayers.

Chapter 3

Wave Propagation in Expanding Cell Monolayers

This chapter is based on a paper published in ***Physical Review Letters 114, 228101 (2015)*** *with S. Banerjee and M. C. Marchetti as co-authors. My contribution was to perform numerical simulations and provide numerical results, make necessary analytical calculations and contribute to the discussion of the results and the writing of the manuscript.*

3.1 Introduction

In the previous chapter we proposed and discussed a mechanochemical model of collective cell migration. In this model the cell monolayer is described as as an elastic continuum coupled to an internal degree of freedom, the concentration of active contractile units. In this chapter we apply the model to an expanding cell monolayer which is relevant to wound healing assay experiments. Recent wound healing assay experiments reveal that unconstrained tissue expansion is accompanied by propagating mechanical waves and build-up of intercellular stresses [7]. These waves are controlled by expressions of myosin activity, cell-cell adhesion and cytoskeletal remodeling. Previous work has also shown that the dynamics of active materials which include cell tissues, predict a broad class of non-equilibrium states including spontaneous flow, wave propagation and pattern formation [101–104]. It remains unclear, however, how cell contractility, polarization or tissue cohesion influence stress generation and wave propagation.

In this chapter we approximate the dynamics of the cell monolayer in one dimension, since in wound healing assays, cells move unidirectionally. We then show how the mechano-chemical feedback between local strain and contractility successfully captures the experimentally observed stress waves [7]. We show this in series of results that include kymographs of monolayer stresses and monolayer velocity. We analyze these waves by means of linear stability analysis which gives us a phase diagram exhibiting a region of parameters where these propagating waves can occur. The linear stability analysis gives a wave equation that shows how the coupling between cell contractility and cellular deformations yields an effective inertia necessary to generate propagating stress waves. We then use a scaling model for the expanding cell layer to study how the cell monolayer responds to propagating waves. The scaling model captures the mechanical oscillations and predicts self-sustained periods of stiffening and fluidization in the tissue.

3.2 Minimal Continuum Model for Spreading Cell Monolayer

3.2.1 Simplifying the Model to One Dimension

We begin by specializing the model introduced in Chapter 2 to one dimension. This is appropriate for wound healing assays where cells move in one direction to close the rectangular gap as shown in Fig. 4, top frame in Chapter 2. We thus consider one dimensional model of an expanding cell monolayer by assuming translational invariance along the y direction. The cell monolayer is described as a self-propelled medium coupling the dynamics of the deformation of the medium, the concentration of force-generating agents and the local polarization and is expanding in x-direction with velocity $v(x,t)$ as shown in Fig. 3.1.

3.2.2 Dynamical Equations Governing the Model

The monolayer is treated as an elastic continuum whose displacement field $u(x,t)$ is actively forced by polarization field $p(x,t)$ and contractile stress. The equations of motion governing the displacement field, polarization field and the concentration field are respectively given by,

$$\zeta \partial_t u = f p(x,t) + h(t)\partial_x \sigma \ , \tag{3.1a}$$

$$\partial_t p = (a - bp^2)p + \kappa \partial_x^2 p - w\partial_x \varepsilon + w' \partial_x (c/c_0) \ , \tag{3.1b}$$

$$\partial_t c + \partial_x (cv) = -\frac{1}{\tau}(c - c_0) + \alpha \varepsilon + D\partial_x^2 c \ . \tag{3.1c}$$

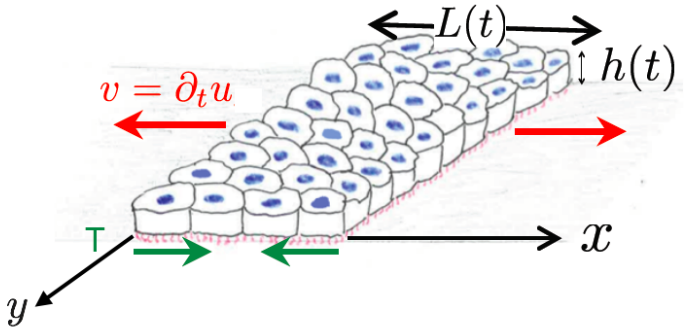

FIGURE 3.1: A schematic of a cell monolayer, with height $h(t)$ and length $L(t)$ expanding in x direction with velocity $v(x,t) = \partial_t u$, where u is the cell layer displacement. The cell monolayer exerts a traction T on the substrate.

with $\sigma(x,t)$ the internal stress in the monolayer, given by

$$\sigma = B\varepsilon + \beta \log\left(c/c_0\right) , \tag{3.2}$$

The left hand side of Eq. (3.1a) describes viscous friction with the substrate with ζ the friction constant. The first term of the right hand side (R.H.S) of Eq. (3.1a) describes the propulsion force due to cell polarization, the second term describes the traction forces. The first term of R.H.S of Eq. (3.1b) with $b > 0$ allow for the onset of a homogeneous polarized state $p = \sqrt{a/b}$ when $a > 0$. The stiffness constant κ in the second term characterizes the cost of local deformations in the polarization. The last two terms in Eq. (3.1b) define active couplings of p to the strain and the concentration field, with $w, w' > 0$, such that p aligns with the gradient of monolayer density and the concentration field $c(x,t)$. The convective flux on the left hand side of Eq (3.1c) describes that the monolayer expansion can change the local concentration of active units. The first term of the R.H.S describes the relaxation of active units to equilibrium concentration c_0 in a timescale τ. The parameter $\alpha > 0$ in the second term describes the rate of production of c due to cellular stretching. The parameter D in the last term of Eq. (3.1c) is an effective diffusion constant, describing the tendency of neighboring cells to equalize activity levels. The internal stress $\sigma(x,t)$ in Eq. (3.2) is given by the sum of an elastic stress, with B the compressional elastic modulus and $\varepsilon = \partial_x u$ the strain field, and an active stress that depends logarithmically on the concentration c of active contractile units, such as phosphorylated myosins interacting with actin filaments and whose magnitude depends on $\beta > 0$.

3.2.3 Initial and Boundary Conditions

We consider the stress free boundary conditions i.e., $\sigma(\pm L/2, t) = 0$ at all times. We assume that the monolayer is initially undeformed, $u(x, 0) = 0$, with an equilibrium concentration of contractile elements, $c(x, 0) = c_0$, and choose a no-flux boundary condition for c, $\partial_x c(\pm L/2, t) = 0$. Together Eqs. (3.1a) and (3.1c) define the dynamics of the spreading monolayer, given the form of $p(x, t)$ in Eq (3.4), the boundary and initial conditions. The length of the spreading layer at time t is given by,

$$L(t) = L_0 + u(L_0/2, t) - u(-L_0/2, t) \,, \tag{3.3}$$

and the height is determined by the condition of volume conservation, $h(t)L(t) = h_0 L_0$, with L_0 and h_0 the initial length and height of the monolayer prior to expansion, respectively.

3.2.4 Approximation of the Polarization Field

We assume that the polarization field relaxes more quickly than the monolayer density or the concentration field, i.e, we consider that $t \gg a^{-1}$ and let $w = w' = 0$. The polarization profile is then time-independent, and for $L \gg \sqrt{\kappa/a}$ can be approximated as,

$$p_\infty(x) \simeq \sqrt{(a/b)} \tanh(x/\lambda) \,, \tag{3.4}$$

where $\lambda = \sqrt{\kappa/a}$ is a length scale controlling the width of the transition zone from left moving to right moving cells (Fig. 3.2) at the center of the monolayer. For simplicity we let $a = b$ which means $p \longrightarrow \pm 1$ at the cell edges. We first use this approximation in studying the tissue spreading. We later study the effects of time-dependent polarization field in Section 3.6.

3.3 Steady State Solutions

The homogeneous steady-state of Eqs. (3.1a) and (3.1c) is given by $u = 0$ and $c = c_0$. This is a quiescent steady-state when the cell layer does not spread ($f = 0$). To determine the inhomogeneous steady-state describing an expanded cell monolayer ($f \neq 0$), we seek solutions of Eqs. (3.1a) and (3.1c) by setting $\partial_t u = 0$ and $\partial_t c = 0$. The analytical steady state solution for Eq. (3.1a) gives,

$$\sigma_\infty = -\frac{\lambda f}{h_\infty} \ln\left(\frac{\cosh x/\lambda}{\cosh L_\infty/2\lambda}\right), \tag{3.5}$$

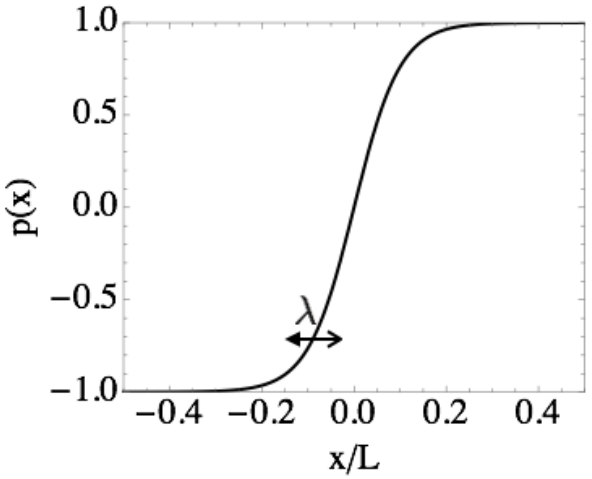

FIGURE 3.2: Profile of time independent cell polarization. The parameter λ describes the length scale controlling the width of transition zone between left and right moving cells at the center of the monolayer.

To make analytical progress, we first consider a cell monolayer of length much larger than the length scale of variations in the polarization, i.e $L >> \lambda$. In this limit the spreading force can be described by a signum function, $\tanh(x/\lambda) \sim \text{sign}(x/L)$ for $\lambda << L$. Next we linearize the active stress by considering small deviation of c from its rest-state c_0, $\log(c/c_0) \sim (c - c_0)/c_0$. The steady-state solution for the local stress is then given by,

$$\sigma_\infty(x) = -\frac{f}{h_\infty}\left(|x| - \frac{L_\infty}{2}\right), \tag{3.6}$$

where L_∞ and h_∞ are respectively the length and the height of the cell monolayer at

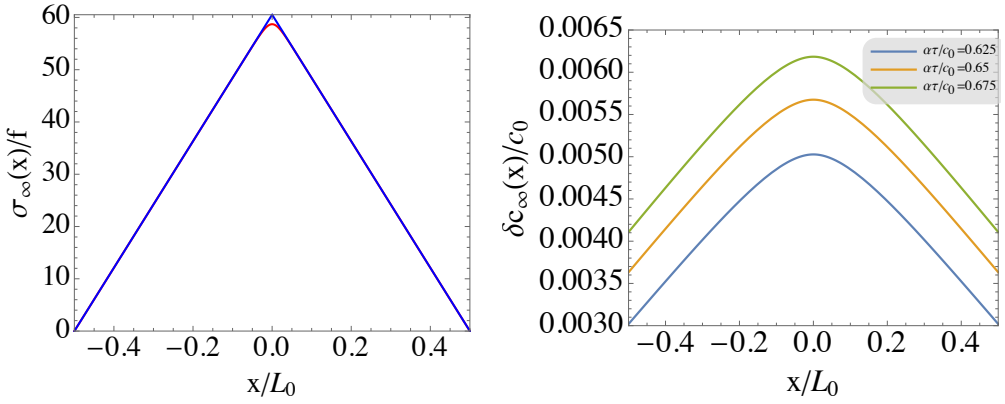

FIGURE 3.3: Left: Profile of the steady state stress. In red we consider the nonlinear solution in Eq. (3.5), in blue we use the linear limit of stress in Eq. (3.6). Right: Profile of $\delta c_\infty = c_\infty - c_0$, change in steady state concentration field for different values of the time scale of turnover of the contractile elements. Parameters: β/f =49; B/f =30; h_0/L_0 =0.0083, λ/L_0 =0.05 and $D\tau/L_0^2$ =0.025.

$t \to \infty$, given by $L_\infty = L_0(1 + \langle\varepsilon_\infty\rangle)$ and $h_\infty = h_0/(1 + \langle\varepsilon_\infty\rangle)$. The spatial average of

the steady-state strain $\langle\varepsilon_\infty\rangle$ is given by,

$$\langle\varepsilon_\infty\rangle = \frac{1}{L_\infty}\int_{-L_\infty/2}^{L_\infty/2} \mathrm{d}x\varepsilon_\infty(x)\ . \tag{3.7}$$

Combining Eqs.(3.1a), (3.1c) and (3.6) we obtain a second order ordinary differential equation in c_∞ whose analytical solution is,

$$c_\infty(x) = \frac{\alpha\tau}{B_{\text{eff}}}\left[-\frac{f}{2h_\infty}\left(|x| - \frac{L_\infty}{2} + \xi\frac{\left(\mathrm{e}^{-L_\infty/2\xi}-1\right)\cosh(x/\xi)}{\sinh(L_\infty/2\xi)} + \xi\mathrm{e}^{-|x|/\xi}\right) + \beta + \frac{Bc_0}{\alpha\tau}\right]\ , \tag{3.8}$$

where $B_{\text{eff}} = B + \alpha\beta\tau/c_0$ is the effective elastic modulus renormalized by active contractility and $\xi = \sqrt{\frac{BD\tau}{B_{\text{eff}}}}$ is a characteristic length scale associated with the spatial variation of the active agents. The analytical solution of the steady state shows that longer turnover timescale gives more concentration of contractile units (Fig. 3.3) as one would assume. The steady-state solution for the average strain is,

$$\varepsilon_\infty(x) = \frac{1}{B}\left(\sigma_\infty - \frac{\beta}{c_0}c_\infty + \beta\right)\ . \tag{3.9}$$

The condition for the cell monolayer to expand is given by $\langle\varepsilon_\infty\rangle > 0$ which leads to a critical value for the force density, $f_0^c = 8\beta h_\infty B_{\text{eff}}/BL_\infty$ above which the cell monolayer spreads.

3.4 Propagating Waves

3.4.1 Linear Stability Analysis of the Quiescent Homogeneous State

To understand the origin of wave propagation and estimate the wave frequency, it is useful to examine the linear fluctuations in the strain field, $\delta\varepsilon$ and the concentration field δc, about the quiescent homogeneous state, $u = 0$, $c = c_0$ and no spreading force. Using Eqs. (3.1a) and (3.1c), one can then eliminate δc from such linearized equations to obtain the linearized dynamics of strain fluctuations,

$$\tau\zeta\partial_t^2\delta\varepsilon + \zeta\partial_t\delta\varepsilon = h_0\left(B_{\text{eff}} + \eta_{\text{eff}}\partial_t - \tau BD\partial_x^2\right)\partial_x^2\delta\varepsilon\ , \tag{3.10}$$

The above equation shows that the coupling of strain to concentration field yields an effective mass density (inertia), $\tau\zeta$, and viscoelasticity characterized by an effective elastic modulus, $B_{\text{eff}} = B + \alpha\beta\tau/c_0$, and an effective viscosity $\eta_{\text{eff}} = (B - \beta + D\zeta/h_0)\tau$. The dynamics of strain fluctuations resembles a damped Kelvin-Voigt oscillator with a

characteristic frequency of oscillations,

$$\omega_0 = q\sqrt{h_0\left(B_{\text{eff}} + \tau q^2 BD\right)/(\tau\zeta)}\,, \tag{3.11}$$

with q the wavevector. The estimate for the time period $2\pi/\omega_0$ agrees well with the time period determined from numerics for $q \simeq 4\pi/L_0$ (see Fig. 3.4) and with the value measured in recent experiments [7]. Finally, we note that if the concentration c is

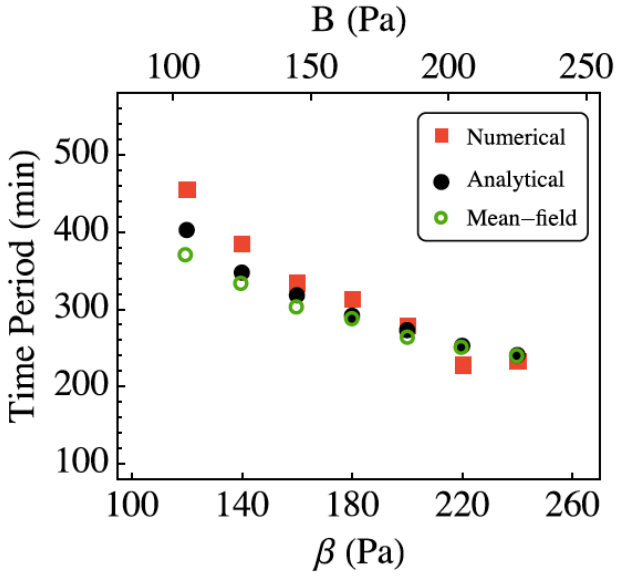

FIGURE 3.4: Period of oscillation determined from the numerical solution to Eqs. (3.1a,3.1c) (red squares), obtained from the analytical expression in Eq. (3.11) (black solid circles), and as predicted by the mean-field model (green open circles) for various values of β and B. The numerical value for the time period is obtained by performing a fast fourier transform on the strain rate at the midline of the monolayer. Parameters: $B = 120$ Pa, $\beta = 200$ Pa, $\tau = 350$ min, $\alpha/c_0 = 1/560$ min^{-1}, $L_0 = 600$ μm, $h_0 = 5$ μm, $f = 4$ Pa, $\lambda = 30$ μm, $\zeta = 0.009$ nN min/μm^3, $D = 26$ μm^2/min and $\lambda_0 = L_0/2$.

conserved ($\tau \to \infty$; $\alpha = 0$), stable propagating waves are spontaneously generated for $0 < B - \beta + D\zeta/h_0 < 2\sqrt{DB\zeta/h_0}$. If diffusion is slow compared to elastic relaxation, $D\zeta/Bh_0 \ll 1$, stable propagating waves are not observed. In the opposite limit of infinitely fast turnovers in contractility ($\tau \to 0$), strain fluctuations decay diffusively at a rate $\simeq Bh_0/\zeta L^2$. A linear stability analysis of the homogeneous stationary solution $(\varepsilon_\infty(x), c_\infty(x))$ yields the range of parameter values where propagating waves can occur. The resultant phase diagram is shown in Fig. 3.5, as functions of the contractile activity β and the compressional modulus B. For $\alpha > 0$ and a fixed value of elastic modulus B, the phase diagram in Fig. 3.5 shows that the propagating waves occur at finite values of the wavenumber and are not observed in the long wavelength limit ($q \to 0$). The oscillations are unstable when the effective damping coefficient in Eq. (3.10), $\zeta_{\text{eff}} \simeq \zeta + \eta_{\text{eff}}/L^2$, changes sign for $\beta > \zeta L^2/\tau + B + D\zeta/h_0$. If $\alpha < 0$, the waves disappear and there exists a long wavelength *contractile* instability for $\beta > Bc_0/\alpha\tau$, describing material

failure [105]. In the absence of contractility ($\beta = 0$) the long-wavelength instabilities do not arise for $\alpha < 0$, as discussed in Ref. [106].

3.4.2 Numerical Solution

In the absence of propulsion force ($f = 0$), the cell layer is in a quiescent homogeneous state, with $u = 0$ and $c = c_0$. When $f \neq 0$, the cell layer spreads and reaches a steady-state at long times. We have integrated numerically Eqs. (3.1a,3.1c) with the given initial and boundary conditions, using the Runge-Kutta-Fehlberg method. The model parameters are chosen to quantitatively describe the available experimental data for MDCK colonies [7]. The phase diagram shown in Fig. 3.5 displays three dynamical regimes in terms of contractile activity β and compressional modulus B (controlled by cell-cell adhesion): a region where fluctuations are stable and diffusive at low contractility, an intermediate region where the system supports propagating waves, and a region where the propagating waves become unstable at high contractility. There is good

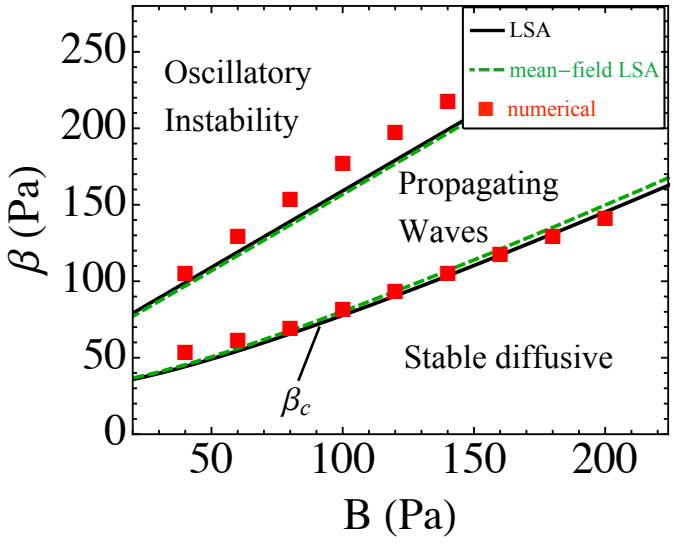

FIGURE 3.5: Phase diagram of the spreading gel. The vertical axis represents the contractile activity β and the horizontal axis is the compressional modulus B. Three behaviors are observed: stable diffusive, stable propagating waves, and oscillatory instability. The red squares are obtained from the numerical solutions of the full nonlinear model, the black solid lines are the results of the linear stability analysis (LSA) of the equilibrium state (at $q = 13.5/L_0$) , and the dashed green lines refer to the LSA of the mean-field model given in Eqs. (3.12). Parameters: $B = 120$ Pa, $\beta = 200$ Pa, $\tau = 350$ min, $\alpha/c_0 = 1/560$ min^{-1}, $L_0 = 600$ μm, $h_0 = 5$ μm, $f = 4$ Pa, $\lambda = 30$ μm, $\zeta = 0.009$ nN min/μm^3, $D = 26$ μm^2/min.

agreement between the boundaries obtained via numerical solution of the full nonlinear equations (red diamonds) and those determined by the linear instability of fluctuations

about the equilibrium, undeformed state [1] and about the long-time solution of the mean-field model in Eqs.(3.12). In the region of propagating waves, the stress initially shows a few local maxima (Fig. 3.6, top right frame), which evolve towards a single maximum at the center of the monolayer, as observed in experiments [7, 107]. The concentration of contractile elements also oscillates and builds up at the center of the monolayer (Fig. 3.6, top left frame). The stress waves propagate nearly in phase with the strain

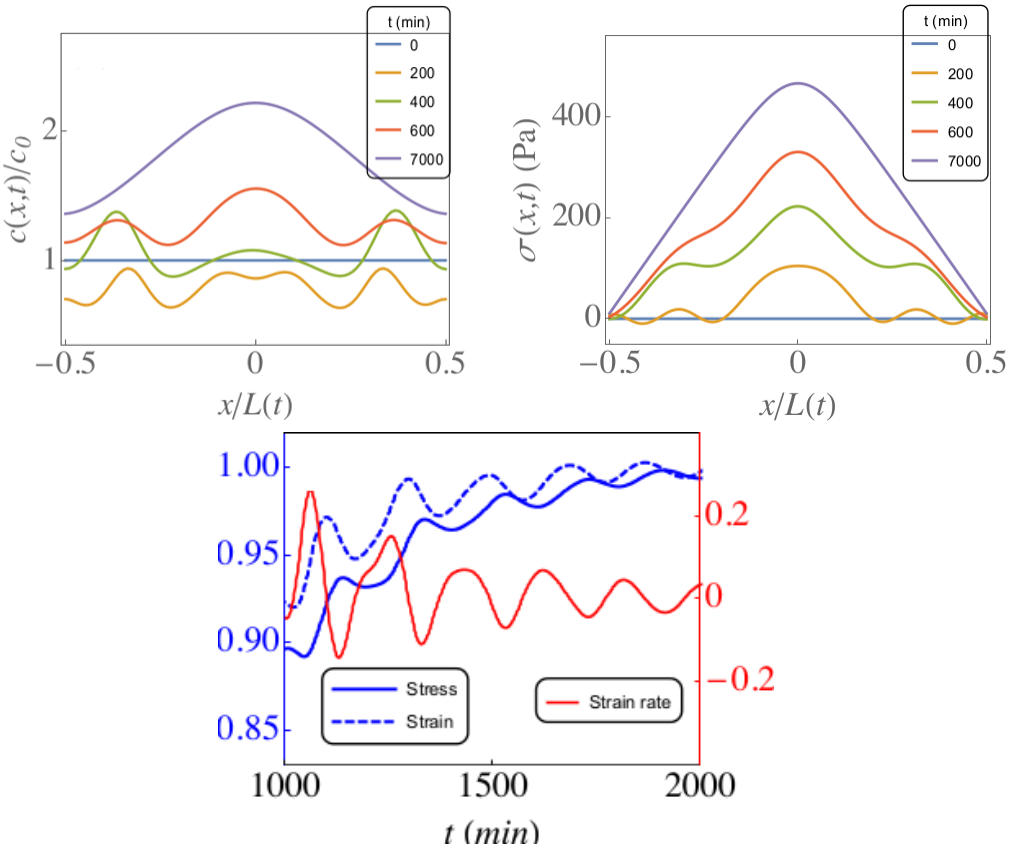

FIGURE 3.6: Top: (Left) Time-evolution of the concentration of contractile units , $c(x,t)$, normalized by its equilibrium value. (Right) Time-evolution of the internal stress $\sigma(x,t)$ in the monolayer. Bottom: Midline stress $\sigma(0,t)/\sigma_\infty(0,t)$ (blue solid), midline strain $\varepsilon(0,t)/\varepsilon_\infty(0,t)$ (blue dashed) and midline strain rate $\dot{\varepsilon}(0,t)$ (red solid, units 10^{-4} s^{-1}) as functions of time. The parameter values are taken to be the same as in Fig. 3.5

field, whereas the strain rate fluctuates nearly out of phase with the stress (Fig. 3.6, bottom frame). Thus the response of the material is dominated by elastic relaxation with dissipation induced by turnovers in contractility on a timescale τ. The waves span the entire length of the monolayer and consist of a strain rate wavefront that propagates inwards from the edge, and then travels back to the edge, resembling an X-pattern, as observed experimentally [7]. With the given parameter values our numerical simulations capture the mechanical waves as evident in the kymographs of velocity, stress, strain rate and concentration of contractile units (Fig. 3.7A-D).

[1] More details in Section 3.4.1 for Linear Stability Analysis

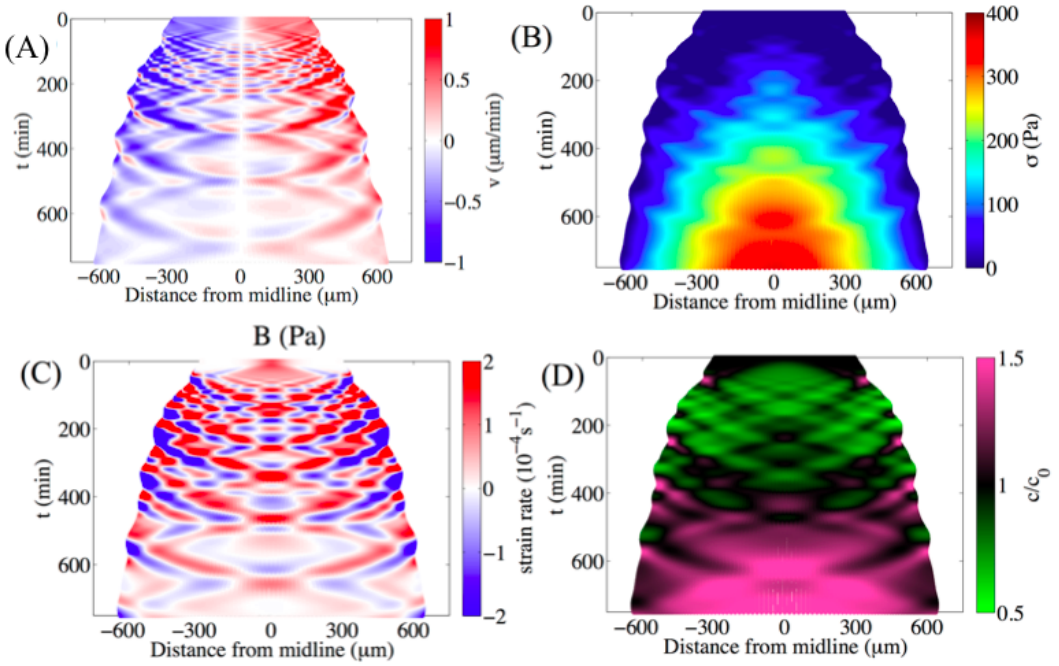

FIGURE 3.7: Kymographs of (A) the monolayer velocity field (B) monolayer stress field, (C) monolayer strain rate $\partial_t \varepsilon(x,t)$, and (D) the concentration field $c(x,t)/c_0$. The parameter values are taken to be the same as in Fig. 3.5.

3.5 Mean Field Model

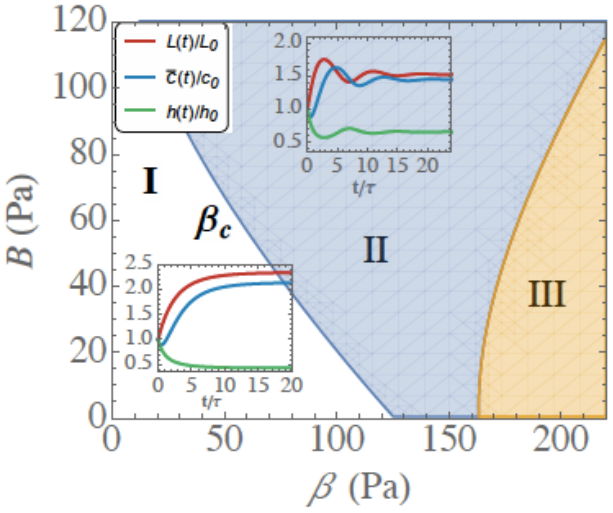

FIGURE 3.8: A phase diagram of the mean-field model in the $B-\beta$ plane: I - stable diffusive, II - propagating waves, III - oscillatory instability. Inset: Dynamics of length (red), height (green) and concentration (blue) normalized by their initial values for $\beta =$ 100 Pa (region II) and $\beta = 30$ Pa (region I). Oscillatory solutions appear for $\beta > \beta_c(B)$, defining the phase boundary between regions I and II. Parameters: Parameters: $B = 60$ Pa, $\tau = 350$ min, $c_0/\alpha = 780$ min, $F_0 = 8$ nN, $\gamma = 9$ nN min/μm, $dh_0/L_0^2 = 0.1$.

The mean field limit of the continuum model is obtained by neglecting spatial variations

in c and ε and it is formulated in terms of the length (L), height (h), and the average concentration of contractile elements, $\bar{c}(t) = \frac{1}{L}\int_0^L dx\ c(x,t)$, with

$$\gamma \frac{dL}{dt} = F_0 - A(t)\sigma(t)\ , \tag{3.12a}$$

$$\frac{d\bar{c}}{dt} + \frac{\bar{c}}{L}\frac{dL}{dt} = -\frac{1}{\tau}(\bar{c} - c_0) + \alpha\varepsilon\ , \tag{3.12b}$$

with F_0 the propulsion force, γ the friction, $A(t) = dh(t)$ the cross-sectional area, $\varepsilon(t) = L(t)/L_0 - 1$ the strain and $\sigma(t)$ the internal stress given by $\sigma(t) = B\varepsilon(t) + \beta(\bar{c}(t)/c_0 - 1)$. The height is determined using the incompressibility condition, with the size in the y direction, d, fixed. The steady state solution is $L_\infty = L_0/(1-\Lambda)$, $h_\infty = h_0(1-\Lambda)$ and $c_\infty = c_0 + \alpha\tau\Lambda/(1-\Lambda)$, with $\Lambda = c_0F_0/dh_0(Bc_0 + \alpha\beta\tau)$ the net compressive strain in the z-direction. For a given value of elastic modulus B, the mean-field model predicts oscillatory solutions for $\beta > \beta_c$ (See Fig. 3.8), where $\beta_c(B)$ defines the phase boundary in (B, β) plane separating the regions of propagating waves and diffusive spreading (dashed line in Fig. 3.5). The stress waves manifest as shape oscillations in the growing length and the shrinking height of the cell monolayer (Fig. 3.8). For $\beta < \beta_c$ the monolayer diffusively approaches the steady state (c_∞, L_∞) (See Fig. 3.8). This simple mean-field approach allows us to study the material response of the monolayer characterized by an effective elastic modulus, $B_{\mathrm{MF}} = d\sigma/d\varepsilon$. The oscillatory regime ($\beta > \beta_c$) exhibits sustained oscillations in the material rigidity, B_{MF}, with a slow period of stiffening followed by a sharp turnover (see Fig. 3.9). For $\beta < \beta_c$, the material gradually stiffens with B_{MF} asymptotically approaching the value B_{eff}. These oscillations reflect self-sustained turnovers in the cytoskeleton with periodic reinforcement and fluidization on different timescales, which was invoked to be the underlying mechanism of wave propagation in Ref. [7].

3.6 Time-dependent Propulsion Forces

Finally, we consider time variations of the propulsion force, as arising from the dynamics of cell polarization $p(x,t)$ given by

$$\partial_t p = (a - bp^2)p + \kappa\partial_x^2 p - w\partial_x\varepsilon + w'\partial_x(c/c_0)\ , \tag{3.13}$$

where the first two terms with $b > 0$ allow for the onset of a homogeneous polarized state when $a > 0$. The stiffness constant κ characterizes the cost of local deformations in the polarization. The last two terms in Eq. (3.13) define active couplings of p to the strain and the concentration field, with $w, w' > 0$, such that p aligns with the gradient of monolayer density and the concentration field. In other words, cell polarization is

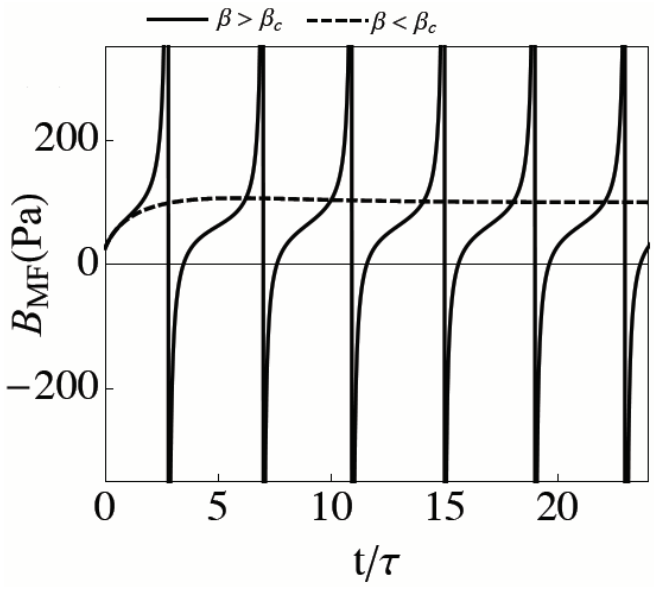

FIGURE 3.9: Mean-field elastic modulus B_{MF} of the cell monolayer as a function of time, showing oscillatory stiffening or fluidization for $\beta = 100$ Pa (solid) and steady stiffening for $\beta = 30$ Pa (dashed).

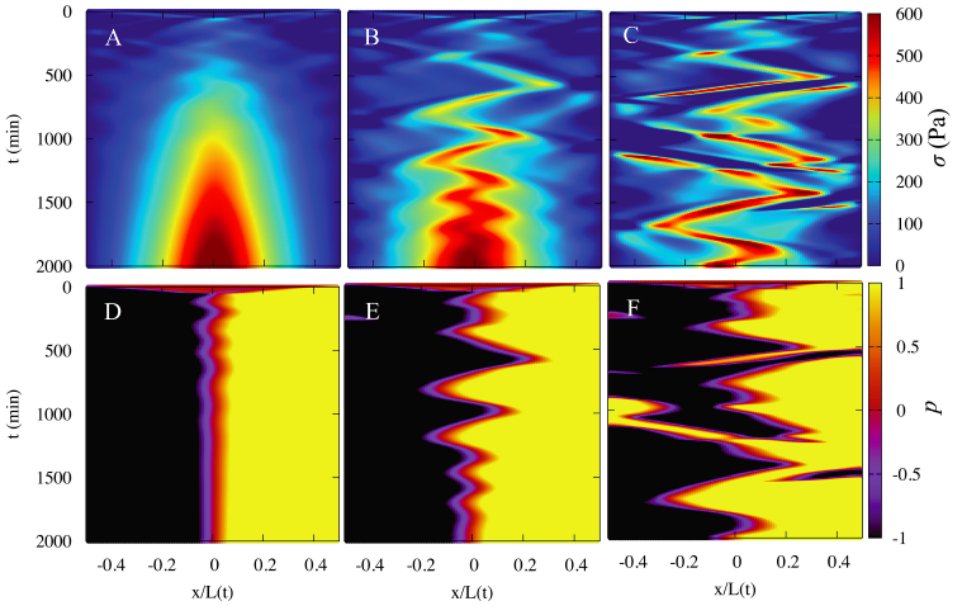

FIGURE 3.10: Spatio-temporal evolution of internal stress (A-C) and polarization (D-F) as the polarization induced tension β' is increased (left to right). (A,D) X-waves, $\beta' = 12$ nN/μm; (B,E) traveling stress pulse, $\beta' = 17$ nN/μm; (C,F) complex oscillatory patterns, $\beta' = 24$ nN/μm. Parameters: $w = 4.3$ μm/min, $w' = 0.21$ μm/min, $\kappa = 193$ μm^2/min, $a = 0.07$ min^{-1}, $b = 0.03$ min^{-1}. Other parameter values are the same as in Fig. 3.5. See Section.. for kymographs of strain rate, velocity and the traction stress.

enhanced in the direction opposite to that of elastic restoring forces. Additionally, polarization gradients can induce mechanical stresses, and the stress tensor is modified to read, $\sigma = B\varepsilon + \sigma_a(c) + \beta'\partial_x p$, where $\beta' > 0$ is a contractile tension induced by

polarization gradients. We assume a no-flux boundary condition, $\partial_x p(\pm L/2) = 0$.

When the coupling of polarization to strain and contractility is turned on, various spatiotemporal patterns emerge as the active tension β' is varied. For small β', the stress patterns are qualitatively similar to Fig. 3.7B (with time-independent propulsion), and p asymptotically approaches p_∞ with initial oscillations near the midline (Fig. 3.10 A,D). For intermediate β', a traveling stress pulse emerges in the layer and the location of stress maxima oscillate around the midline (Fig. 3.10B). This is accompanied by large amplitude oscillations of net polarity that attenuate in time to generate a symmetric steady state polarization profile (Fig. 3.10E). These traveling pulses persist even in the case $\beta = 0$. For even higher values of β' complex oscillatory patterns emerge in the monolayer stress and polarization (Fig. 3.10C,F).

3.7 Discussion

We have developed a simple yet rich dynamic model for an active spreading gel, based on a linear feedback between local strain and contractility. A local increase in length due to spreading promotes the assembly of active elements that in turn induce contraction. We propose that a finite turnover rate in the active contractile elements can yield an effective inertia and viscoelasticity in the gel that vanishes for infinitely fast turnover rates. This simple mechano-chemical model allows us to capture the experimentally observed propagating stress waves during tissue expansion without invoking nonlinear elasticity [7]. These stress waves are characterized by strain rate wavefronts that initiate from the leading edge and periodically travel into and away from the midline of the monolayer. Our findings also elucidate that the effective material rigidity of the tissue undergoes sustained periods of stiffening and softening as the waves propagate. Using a minimal phenomenological model we are able to draw important general conclusions regarding the mechanics of cellular materials. First, a finite turnover rate in the constituent contractile elements can yield an effective inertia and viscoelasticity in an otherwise non-inertial elastic medium. Secondly, the existence of mechanical waves depends upon a local feedback between material strain and contractility. We emphasize that spreading is not crucial for wave propagation and that oscillations can also occur under confinement but the dynamics of the concentration field is crucial in order to get propagating waves. However in contrast to our model, Ref. [108] recently proposed that oscillatory modes in confined layers can also be generated by stochastic motion of cells. Experimental tests that inhibit myosin based contractility or cell directionality can help discriminate between these different models.

Appendix A

A.1 Volume conservation and kinetic constraints

In the mean field model, we begin by considering an ideal wound-healing geometry where the dimensions of the cell layer are by the instantaneous height $h(t)$ (in the z-direction), x-length $L(t)$, and a y-length d. We further consider a thin film, letting $h(t) \ll L(t) \ll d$, such that the changes in d are negligible compared to L and h and assume that there is translational invariance along the y-direction. If the initial height of the cell layer is h_0 and the length is L_0, we define vertical and horizontal strains as,

$$\varepsilon_h(t) = h(t)/h_0 - 1 \,, \tag{A.1a}$$

$$\varepsilon_L(t) = L(t)/L_0 - 1 \,. \tag{A.1b}$$

Volume conservation implies, $h(t)L(t)$ =constant. This leads to the following (related) kinetic constraints,

$$\frac{\dot{h}}{h} = -\frac{\dot{L}}{L} \,, \tag{A.2a}$$

$$\varepsilon_h = -\frac{\varepsilon_L}{1+\varepsilon_L} \,. \tag{A.2b}$$

A.2 Details of Linear Stability Analysis

In this section we examine the linear stability of the homogeneous steady-state. We render our system of equations dimensionless by letting $x \to x/L_0$ and $t \to ft/\zeta L_0$. Then new dimensionless parameters are $\tilde{B} = B/f$, $\tilde{\beta} = \beta/f$, $\tilde{\alpha} = \alpha\zeta L_0/fc_0$, $\tilde{\tau} = f\tau/\zeta L_0$, $\tilde{h}_0 = h_0/L_0$ and $\tilde{D} = D\zeta/fL_0$. In these units, stress is measured in the units of f and the concentration of contractile agents are expressed in units of c_0. In the following we drop the tilde notation over the dimensionless parameters for simplicity. Letting $\varepsilon(x,t) = \delta\varepsilon(x,t)$ and $c(x,t) = 1 + \delta c(x,t)$, the linearized equations for the strain and

the concentration fields are given by,

$$\partial_t \delta\varepsilon = h_0 \left(B\partial_x^2 \delta\varepsilon + \beta \partial_x^2 \delta c \right) \ , \tag{A.3a}$$

$$\partial_t \delta c + \partial_t \delta\varepsilon = -\frac{1}{\tau}\delta c + \alpha \delta\varepsilon + D\partial_x^2 \delta c \ . \tag{A.3b}$$

Taking two spatial derivatives in Eq. (A.3b) and substituting the expression for $\partial_x^2 \delta c = [h_0^{-1}\partial_t \varepsilon - B\partial_x^2 \varepsilon]/\beta$ (obtained from Eq. A.3a), we obtain the effective dynamics of strain fluctuations,

$$\tau\Gamma\partial_t^2 \delta\varepsilon + \Gamma\partial_t \delta\varepsilon = h_0 \left(B_{\text{eff}} + \eta_{\text{eff}}\partial_t - \tau B D \partial_x^2 \right) \partial_x^2 \delta\varepsilon \ , \tag{A.4}$$

where $B_{\text{eff}} = B + \alpha\beta\tau/c_0$ and $\eta_{\text{eff}} = (B - \beta + D\Gamma/h_0)\tau$. The dynamics of strain fluctuations are isomorphic to the dynamics of an driven damped Kelvin-Voigt material, with a characteristic frequency of oscillation ω_0 given as a function of the wavelength λ_0,

$$\omega_0(\lambda_0) = \frac{2\pi}{\lambda_0}\sqrt{\frac{h_0}{\tau\Gamma}\left[B_{\text{eff}} + \tau \left(\frac{2\pi}{\lambda_0}\right)^2 BD \right]} \ . \tag{A.5}$$

We compare the analytical prediction for the time period, $2\pi/\omega_0$, with the time period determined numerically by performing a Fast Fourier Transform on the solution for the strain rate at the center of the cell monolayer. The two values are in good agreement as shown in Fig. 3.4 for $\lambda_0 = L_0/2$.

Next we look for solutions in the form $\delta\varepsilon, \delta c \sim \mathrm{e}^{i\omega t + iqx}$. The two eigenvalues controlling the dynamics of fluctuations are given by the following dispersion relations,

$$i\omega_\pm(q) = -\frac{b(q)}{2} \pm \frac{1}{2}\sqrt{[b(q)]^2 - \frac{4h_0}{\tau}\left[(1 + D\tau q^2)B + \alpha\beta\right] q^2} \tag{A.6}$$

where $b(q) = \dfrac{1}{\tau} + \left[h_0 \left(B - \beta\right) + D\right] q^2$. If the coupling to the concentration of contractile elements is neglected ($\beta = 0$), $i\omega_+ = -h_0 B q^2$ and $i\omega_- = -\frac{1}{\tau}$ (we neglect the diffusion constant D for simplicity assuming that its contribution is small). In this case the elastic deformations are stable and diffuse through the cell layer and no oscillations are observed. When the coupling to the concentration field is considered, we find a region in the parameter space, $\mathcal{I}_m[\omega_\pm] > 0$, where the linear fluctuations are unstable. The system is purely diffusive when $\mathcal{R}_e[\omega_\pm] = 0$ and $\mathcal{I}_m[\omega_\pm] < 0$. The region in the parameter space defined by the complex values of the fourier modes, i.e $\mathcal{R}_e[\omega_\pm] \neq 0$, describe oscillatory solutions. Furthermore, these propagating waves are stable when $\mathcal{I}_m[\omega_\pm] < 0$.

A.3 Oscillatory Condition in Mean Field Model

The mean-field model admits an expanded steady-state solution for the gel with strain ε_∞, and an average concentration of contractile agents $\bar{c}_\infty$. The strain fluctuations decay with similar dynamics as in Eq. (A.4). With $\delta\varepsilon = (L - L_\infty)/L_0$, we get for the dynamics of $\delta\varepsilon$,

$$\tau\gamma\frac{d^2\delta\varepsilon}{dt^2} + (\gamma + h_\infty\eta_{\text{eff}}^{\text{MF}})\frac{d\delta\varepsilon}{dt} + h_\infty B_{\text{eff}}^{\text{MF}}\delta\varepsilon = 0\,, \tag{A.7}$$

where, $B_{\text{eff}}^{\text{MF}} = B - B\varepsilon_\infty - \beta(c_\infty/c_0 - 1) + \alpha\beta\tau/c_0$ and $\eta_{\text{eff}}^{\text{MF}} = \tau(B - B\varepsilon_\infty - \beta c_\infty/c_0)$. The time-period for oscillations is given by,

$$\omega_0^{\text{MF}} = \sqrt{h_\infty B_{\text{eff}}^{\text{MF}}/\tau\gamma}\,, \tag{A.8}$$

Since the mean-field model neglects diffusion, the effective viscosity $\eta_{\text{eff}}^{\text{MF}}$ characterizing the dissipation of strain-rate is less than η_{eff}. We thus add an additive correction η_D to $\eta_{\text{eff}}^{\text{MF}}$ in order to accurately estimate the numerical value for the effective viscosity in our numerical analyses. Thus the condition for oscillatory solutions in Fig. A.1 is given by,

$$4\tau\gamma h_\infty B_{\text{eff}}^{\text{MF}} > [\gamma + h_\infty(\eta_{\text{eff}}^{\text{MF}} + \eta_D)]^2. \tag{A.9}$$

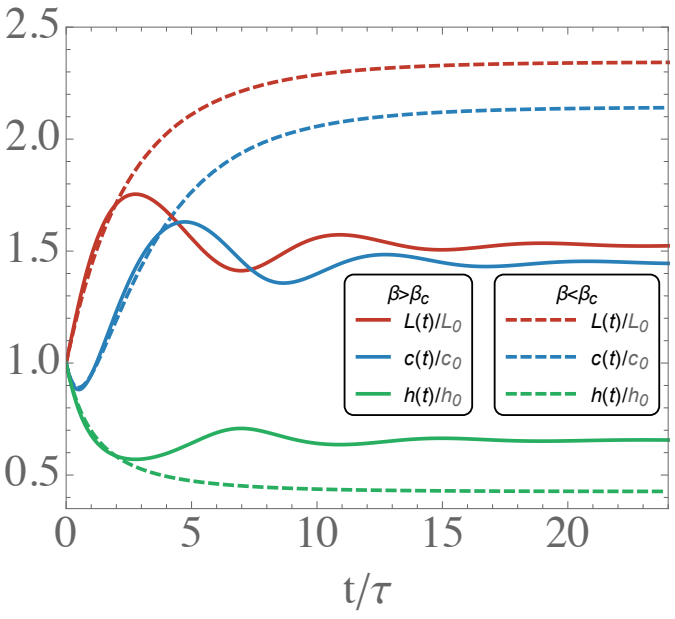

FIGURE A.1: Mean-field length (red), height (green) and concentration normalized by their initial values for $\beta = 100$ Pa (solid) and $\beta = 30$ Pa (dashed) as a function of time, showing oscillatory stiffening or fluidization for $\beta = 100$ Pa (solid) and steady stiffening for $\beta = 30$ Pa (dashed).

A.4 Turnovers in Contractility are Essential for Stress Wave Propagation

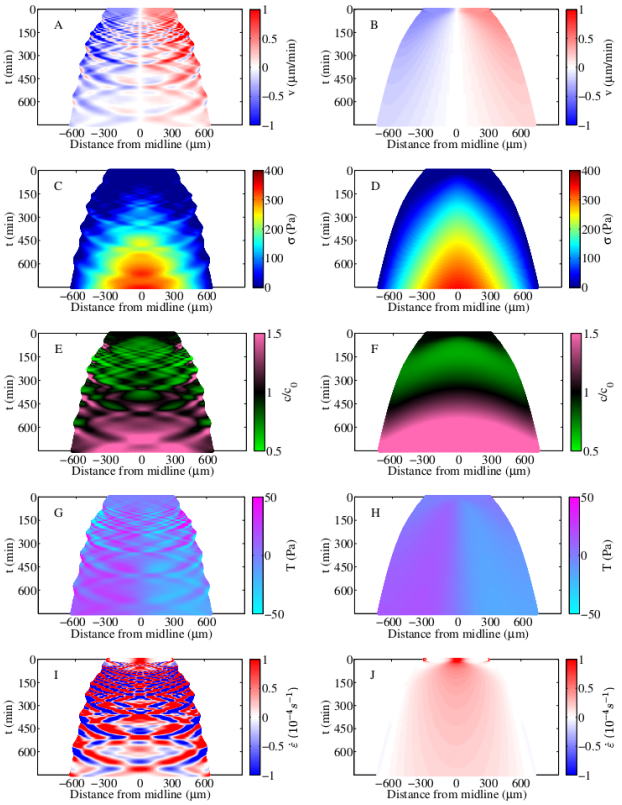

FIGURE A.2: Kymographs of (A,B) monolayer velocity $v(x,t)$, (C,D) monolayer stress $\sigma(x,t)$, (E,F) concentration of contractile elements, (G,H) traction stress $T(x,t)$ and (I,J) strain rate $\dot{\varepsilon}(x,t)$ in the non conserved case (left column) and conserved case (right column) of active units. Parameters: $B = 120$ Pa, $\tau = 350$ min, $(c_0/\alpha) = 560$ min, $L_0 = 600$ μm, $h_0 = 6$ μm, $f = 40$ Pa, $\zeta = 0.09$ nN min/μm^3, $D = 26$ μm^2/min. For the magnitude of the contractile stress, we used $\beta = 200$ Pa for the non conserved case and $\beta = 30$ Pa for the conserved case.

If the concentraction field is concerved ($\tau \to \infty$; $\alpha = 0$), and diffusion is slow compared to elastic relaxation, $D\zeta/Bh_0 \ll 1$, stable propagating waves are not observed as can be see in Fig. A.2B,D,F,H,J. Therefore turnovers in contractility are essential in order to have propagating stress waves.

A.5 Complex Oscillatory Flows due to Polarization Fluctuations

As discussed in Section 3.6 and observed in Fig. 3.10, for small value of the contractile tension β', the patterns in Fig. A.3A,D,G for velocity, concentration and strain rate

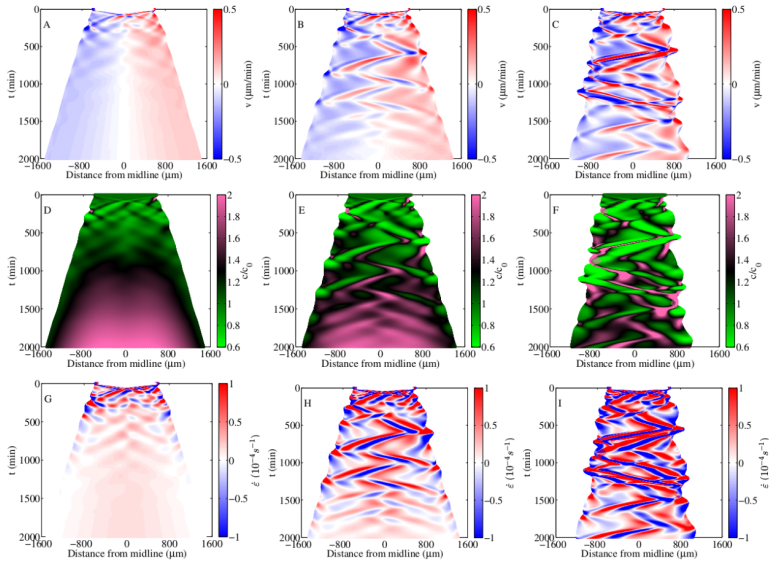

FIGURE A.3: Kymographs of local velocity (A-C), concentration of contractile elements (D-F) and strain rate (G-I) as the polarization induced tension β' is increased (left to right). (A,D,G) X-waves, $\beta' = 12$ nN/μm; (B,E,H) traveling stress pulse, $\beta' = 17$ nN/μm; (C,F,I) complex oscillatory patterns, $\beta' = 24$ nN/μm. Parameters: $w = 4.3$ μm/min, $w' = 0.21$ μm/min, $\kappa = 193$ μm^2/min, $1/a = 14$ min, $1/b = 28$ min. Other parameter values are the same as in Fig. 3.5.

respectively are qualitatively similar to Fig. 3.7 (where the propulsion force is time-independent). For intermediate value of β' (Fig. A.3B,E,H), the patterns of v, c and $\dot{\varepsilon}$ exhibits travelling pulses which lead to complex oscillatory patterns for higher β' (Fig. A.3C,F,I). These patterns persist in the case of zero contractile stress ($\beta = 0$) which means that the complex oscillatory flow depend on the fluctuations in polarization field.

A.6 Choice of Model Parameters

While the model parameters are cell-type dependent, their values are chosen to quantitatively capture available experimental data in MDCK colonies [7]. The model parameters are tuned to capture the experimental data on velocity, strain rates, traction stress and intercellular stresses, while the remaining values are chosen within the order of magnitudes reported in prior literature. Specifically, we choose an initial length of the monolayer $L_0 = 600$ μm, cross-sectional area $A = 1000$ μm^2, spreading force $F_0 = fA = 4$ nN and friction $\gamma = \zeta A = 9$ nN min/μm. The timescale to reach a spread steady-state is thus $\tau_s = L_0\zeta/f \simeq 1400$ min. The timescale controlling activity turnover, τ, and the timescale controlling the strain-concentration feedback, c_0/α, are chosen smaller than τ_s but of the same order. We assume that diffusion is negligible and represents the tendency of neighboring cells to equalize the concentration of active

agents. In our simulation we set the diffusion length to be ~ 5 μm (one grid size) per minute.

Chapter 4

Collective Cell Migration in Confined Cell Monolayers

This chapter is based on a paper published in ***Biophysical Journal 110, 2729 (2016)*** *with J. Notbohm, B. Gweon, H. Jang, Y. Park, J. Shin, J.P. Butler and J.J. Fredberg contributing on the experimental part and S. Banerjee and M.C. Marchetti contributing on the theoretical part as co-authors. My contribution was to perform numerical simulations and provide numerical results, write the theoretical part of the supplementary materials and contribute to the discussion of the results.*

4.1 Introduction

Far from any boundary each cell exerts local tractions upon its substrate that tend to align with the direction of local motion [86, 109]. Near a boundary, in contrast, tractions tend to align systematically towards the cell-free region regardless of the direction of local cellular motion [86].

Working with the experimental group of Prof. J. J. Fredberg at Harvard, we have examined this phenomenon by studying the dynamics of confined tissues. The experiments have provided further evidence showing that each cell polarizes so as to apply local traction in a direction that can deviate systematically from its local velocity, and that this systematic deviation is a general property of collective cellular motion. If local traction and local velocity are not aligned, it follows logically that tractions cannot result solely

from viscous friction between the moving cell and its motionless substrate; rather, tractions must be regulated by variables in addition to velocity [18, 89, 110].

We use our mechanochemical model described in chapter 2 and apply it to a confined cell monolayer to study the misalignment between traction and velocity. We use the confined system because experiments [86, 88] have shown that in confined cell monolayers, the misalignment becomes evident. To account for this local angular deviation between cell traction and velocity, we use the time-dependent cell polarization in our model. To my knowledge we are the first to show how the polarization field in confined environment makes the systematic misalignment between the local velocity and local traction become more conspicuous. Some previous theoretical models [18, 89, 90, 110], but not all [111] have recognized that local tractions can align in a direction that deviates *transiently*, but *not systematically*, from that of the local velocity. This transient misalignment has been modeled by introducing noisy fluctuations around a tendency toward realignment [90, 112]. We conclude that the collective modes of cellular motion result from an interplay between cell contraction and polarization. This chapter comprises results from both experiments and our theoretical model. We start by showing experimentally that the cell monolayer behaves elastically. We then describe the minimal model in circular geometry and discuss the results from the model and compare them to experimental results. The appendix includes the methods and materials used in experiments. Both the model and the experiments show that the dynamics of the polarization field is crucial to generate the standing waves observed in experiments and to capture the misalignment between local traction and local velocity.

4.2 Elastic Behavior of the Cell Monolayer

To study the dynamics of tissues in confinement, masks were prepared with circular holes (diameter = 700 μm) using standard techniques in soft lithography, similar to those described previously in Ref. [7]. These masks were placed onto the polyacrylamide gels before functionalizing with collagen, thus leaving a circular island of collagen to which the cells adhered. Imaging of the Madin-Darby Canine Kidney (MDCK) cell monolayers began approximately one hour after seeding and continued for $\sim$ 30 h (See Fig. 4.1, bottom frame).

We tracked the position of each cell's nucleus to compute the average distance between each nucleus and its neighbors. From these distances, we then computed the local area covered by each cell. Within the confined islands, cellular areas increased as cells collectively moved outward and then decreased as they moved inward (Fig. 4.2a). We

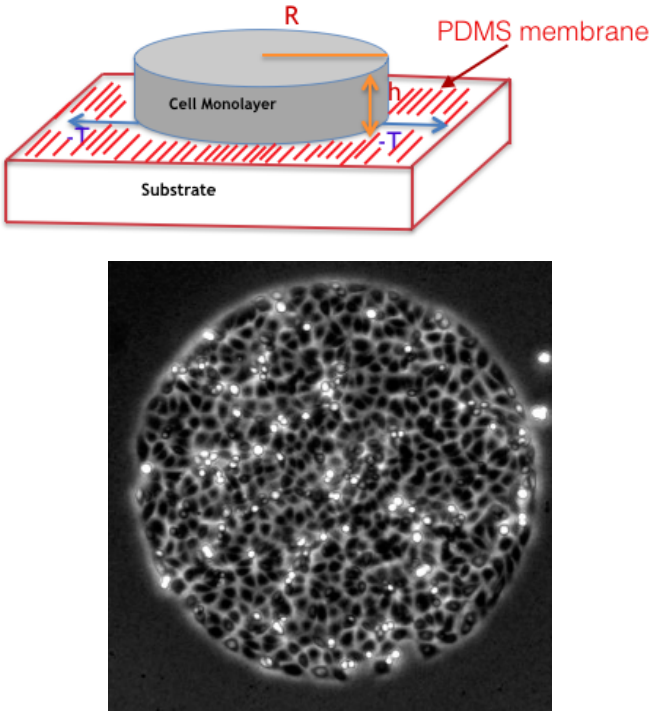

FIGURE 4.1: Top: Schematic of the tissue confined in circular geometry. cells are cultured on a circular opening of the collagen-coated PA substrate with radius R, the tissue has a thickness h. The surrounding of the tissue is a PDMS membrane, so that cells are not allowed to invade new spaces outside the opening. Cells extert a traction T on the substrate. Bottom: MDCK cells in a confined island .

compared the cellular areas to the stresses within the monolayer, which we measured using monolayer stress microscopy [109, 113]. Monolayer stress microscopy applies the principle of force equilibrium to the cell monolayer to compute the in-plane monolayer stresses from the cell-to-substrate tractions.

We found that the tension σ (defined as the mean of the two principal stresses within the cell monolayer) periodically increased and decreased with the same frequency as the radial waves in cellular velocity and with the same phase as the cellular area (Fig. 4.2b), thus implying an elastic relationship. To investigate further the elastic behavior of the monolayer, we examined the relationship between stress and strain rate, and found no correlation (Fig. 4.3).

The lack of correlation implied that viscous contributions to the monolayer stress are negligible.

We then compared the time derivative of stress to the strain rate. Specifically, we plotted the time derivative of the tension $\left(\frac{\mathrm{d}\sigma}{\mathrm{d}t}\right)$ and the trace of the strain rate tensor $\left(\frac{\mathrm{d}\varepsilon}{\mathrm{d}t}\right)$, which were well correlated over time along a single radial position (Fig. 4.2c). The correlation is further evident by a scatter plot (Fig. 4.2d). The elastic modulus K of

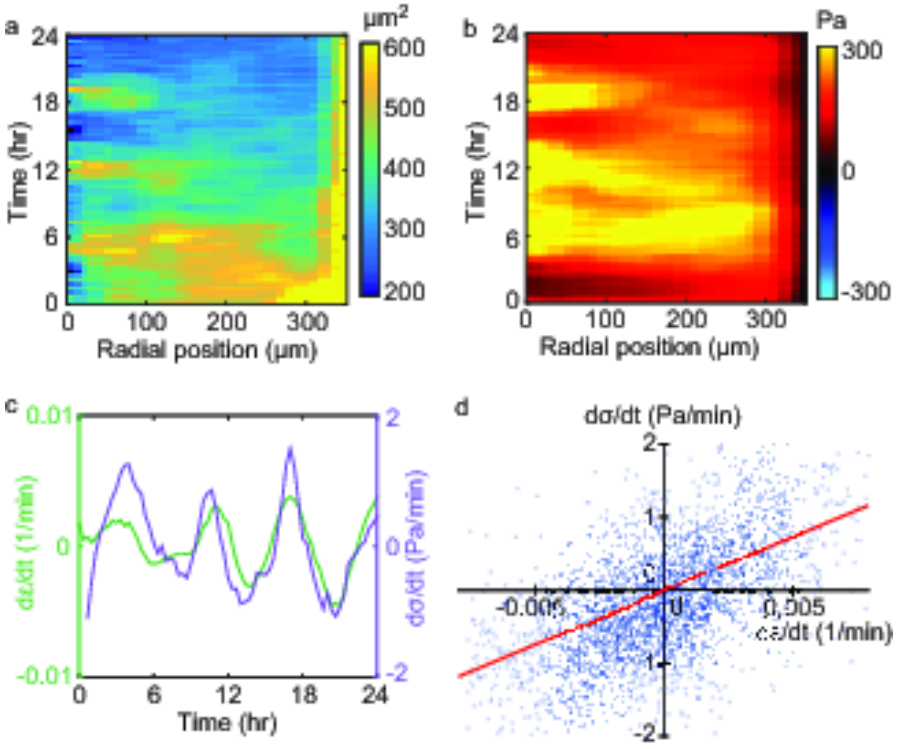

FIGURE 4.2: Elastic behavior of the cell monolayer. (a) The oscillatory motion causes expansion and contraction of each cell, shown by the oscillations in the kymograph of cell area. (b) Contractile tension within the monolayer oscillates in phase with the cell areas. (c) The area strain rate ($\frac{d\varepsilon}{dt}$, defined as the trace of the rate-of-strain tensor) and the time derivative of tension ($\frac{d\sigma}{dt}$) are computed by averaging around a circle 100 μm from the center of the island and plotting over time. $\frac{d\varepsilon}{dt}$ and $\frac{d\sigma}{dt}$ are well correlated (Pearson's correlation coefficient R = 0.77). (d) A scatter plot of $\frac{d\sigma}{dt}$ vs. $\frac{d\varepsilon}{dt}$ for all cell positions at all times shows a positive correlation (R = 0.59). The slope of a linear fit (red line) is equal to the effective elastic modulus of the monolayer, given by K=152 Pa for this cell island. Experiments for n=8 islands give an average value of $K = 113 \pm 28 Pa$ (mean $\pm$ standard deviation). The kymograph of velocity for this cell monolayer is shown in Fig. 4.8d.

the cell monolayer is given by the slope of a line fit to the scatter plot, K=113 $\pm$ 28 Pa (mean standard deviation of n=8 islands).

4.3 Mimimal Model to Model the Experiments

We have numerically solved the equations described in Chapter 2 in a circular geometry by assuming in-plane rotational symmetry (See Fig. 4.1) such that all quantities depend solely on the radial coordinate, r. Rotational symmetry in polar coordinates implies that shear stresses $\sigma_{r\theta}$ vanish and the dynamics of the radial displacement field are solely governed by normal stresses, in agreement with the experiments. The equation of

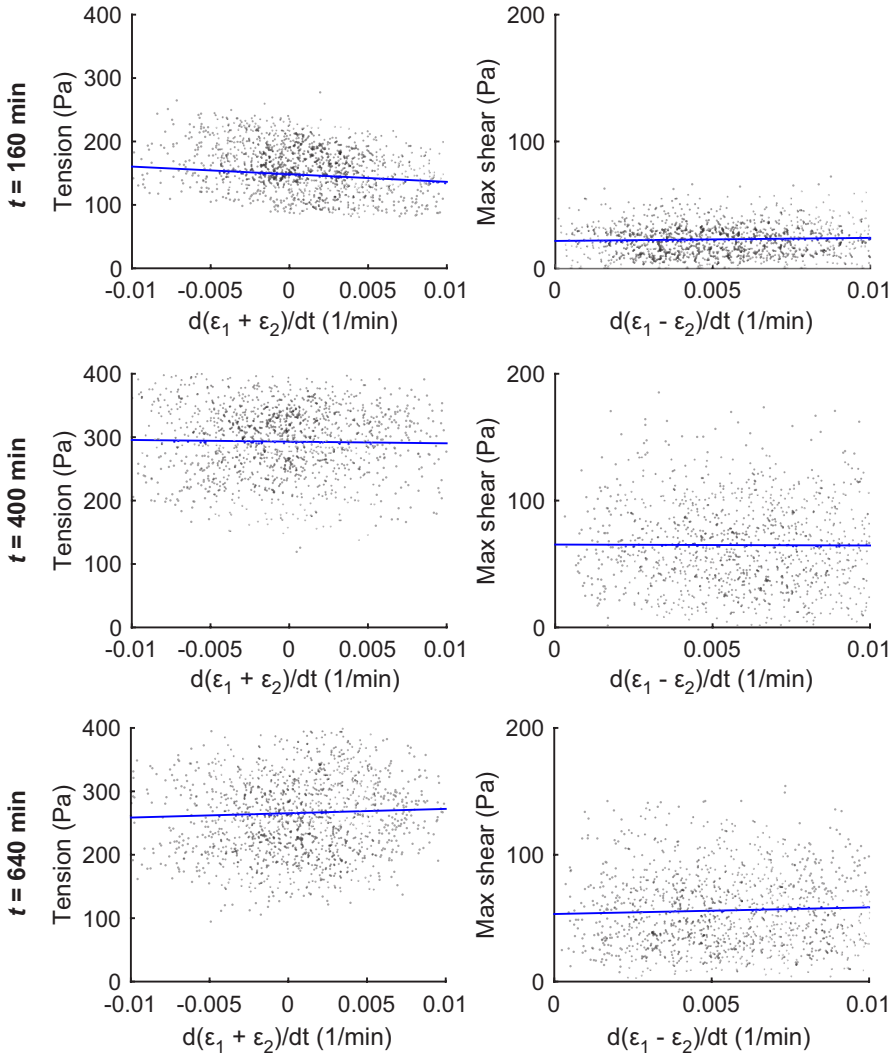

FIGURE 4.3: Negligible viscous stress in the monolayer. To investigate the role of viscosity in the monolayer, the tension (defined as the mean of the principal stresses) is compared to the sum of the principal strain rates, and the maximal shearing stress (defined as half the difference of the principal stresses) is compared to the difference of the principal strain rates. The data shown is for the cell island of Fig. 1 at time points 160, 400, and 640 min. Each dot represents a different location in the island; the blue lines show linear fits. Correlation coefficient magnitudes are typically smaller than 0.1, indicating viscosity has a negligible contribution to the stress tensor.

motion for radial displacements u_r is given by,

$$\zeta \partial_t u_r = f p_r + h \left(\partial_r \sigma_{rr} + \frac{1}{r} \left(\sigma_{rr} - \sigma_{\theta\theta} \right) \right) , \tag{4.1}$$

where σ_{rr} and $\sigma_{\theta\theta}$ define the radial and orthoradial components of the normal stress in the monolayer, given by,

$$\sigma_{rr} = B \left(\partial_r u_r + \frac{u_r}{r} \right) + G \left(\partial_r u_r - \frac{u_r}{r} \right) + \beta \log(c/c_0) , \tag{4.2}$$

$$\sigma_{\theta\theta} = B\left(\partial_r u_r + \frac{u_r}{r}\right) - G\left(\partial_r u_r - \frac{u_r}{r}\right) + \beta \log(c/c_0) \ . \tag{4.3}$$

The equation governing the dynamics of c is given by,

$$\partial_t c + \frac{1}{r}\partial_r \left(rc\partial_t u_r\right) = -\frac{1}{\tau}\left(c - c_0\right) + \alpha c_0 \left(\partial_r u_r + \frac{u_r}{r}\right) \ . \tag{4.4}$$

Finally, the equation governing the dynamics of radial polarization, p_r, is given by

$$\partial_t p_r = a\left(1 - p_r^2\right) p_r + \frac{\kappa}{r}\partial_r(r\partial_r p_r) + w\partial_r(c/c_0) \ . \tag{4.5}$$

The homogeneous solutions to the above equation, $p_r = \pm 1$, describe uniformly polarized states of the cell monolayer with the cell motion pointing radially outwards for $p_r = 1$ and inward for $p_r = -1$. The solution $p_r = 1$ describes the tendency of cell motion to polarize towards the free space at the exterior of the cell island, consistent with *kenotaxis* [114]. To solve the above equations, we assume that no external forces act at the outer boundary such that $\sigma_{ij} n_j = 0$ where n_j is the outward unit normal vector to the boundary. This translates to the boundary condition $\sigma_{rr}(R) = 0$ in circular geometry. We model adhesion with the micropattern by anchoring a hookean spring of stiffness 0.03 Pa/μm at the boundary of the cell monolayer. We choose a no-flux boundary condition for c and p_r, such that $\partial_r c(R) = 0$, and the gradients of the polarization variable at the outer boundary is zero, $\partial_r p_r(R) = 0$. We also assume that the monolayer is initially undeformed, $u(r, 0) = 0$, and unpolarized, $p_r(r, 0) = 0$, with an equilibrium concentration of contractile elements, $c(r, 0) = c_0$. We then integrate numerically Eqs. (4.1), (4.4) and (4.5) with the given initial and boundary conditions by means of the Runge–Kutta–Fehlberg method. We solve three different implementations of the model:

- **u-p** *model.* Radial displacement u_r is coupled only to p_r and the concentration field is assumed to be constant, $c = c_0$. In this case no wave-like behavior is obtained (4.6d–f), indicating that the mechanochemical coupling between c and u_r is crucial to reproduce the waves of oscillatory motion.

- **u-*c*** *model.* Displacement u_r is coupled to c only. The polarization field and hence the propulsion force fp_r are set to zero. In this case we obtain standing waves qualitatively similar to those seen in experiments (Fig. 4.6a-c). However, the traction is proportional to velocity, in contrast to the misalignment observed in experiments.

- **u-*c*-p** *model.* Here we use the full equations of motion, coupling u_r to both c and p_r and are able to quanitatively reproduce the experimental trends (Fig. 4.4).

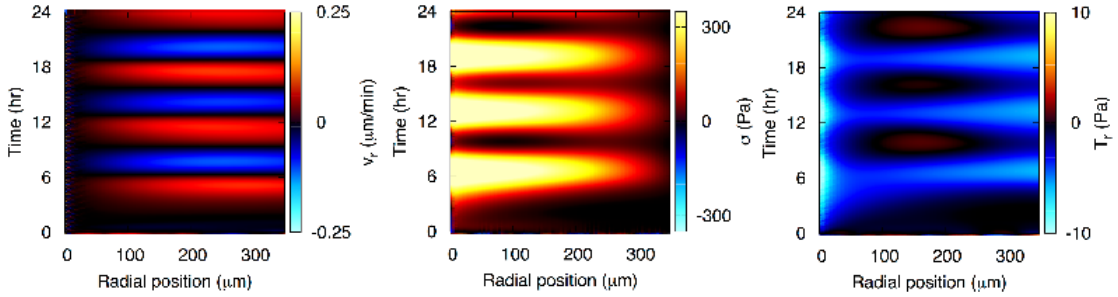

FIGURE 4.4: Left: Kymograph of radial velocity in the cell monolayer captures the experimentally observed collective inward and outward cellular motions. Middle: Kymograph of cellular tension in the monolayer, which increases and decreases periodically with the same frequency as the velocity. Right: Kymograph of radial traction. See Supplementary Table 1 for a complete list of the model parameter values.

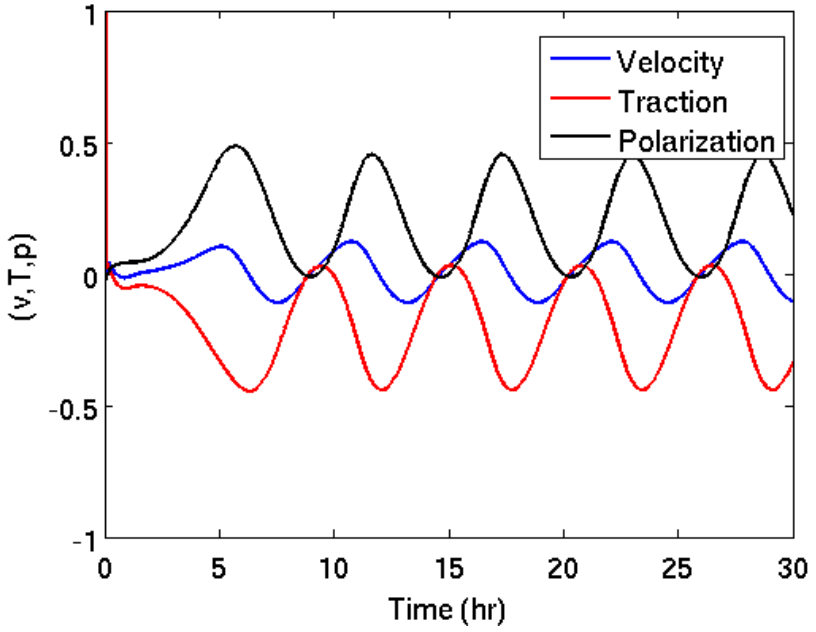

FIGURE 4.5: Midline local velocity $v(x,t)$ (blue), midline local traction $T(x,t)$ (red) and midline local polarization $p(x,t)$ (black) as function of time.

By solving the coupled system given by Eqs. (4.1), (4.4) and (4.5) assuming in-plane circular symmetry, we applied this model to the confined monolayers in our experiments. The results are displayed in a series of kymographs showing the spatiotemporal evolution of the radial velocity, the monolayer tension, and the traction (Fig. 4.4). The model quantitatively captured multiple aspects of our experimental data, namely that the monolayers velocity field alternated between inward and outward motion (Fig.4.4 left frame, Fig. 4.5) with a time period equal to that of the oscillations in the monolayer tension (Fig.4.4 middle frame). This wave-like motion is predicted by the model to arise through the chemo-mechanical feedback between the mechanical strain and the internal state variable [110, 115]. The model captures that the direction of local velocity is not

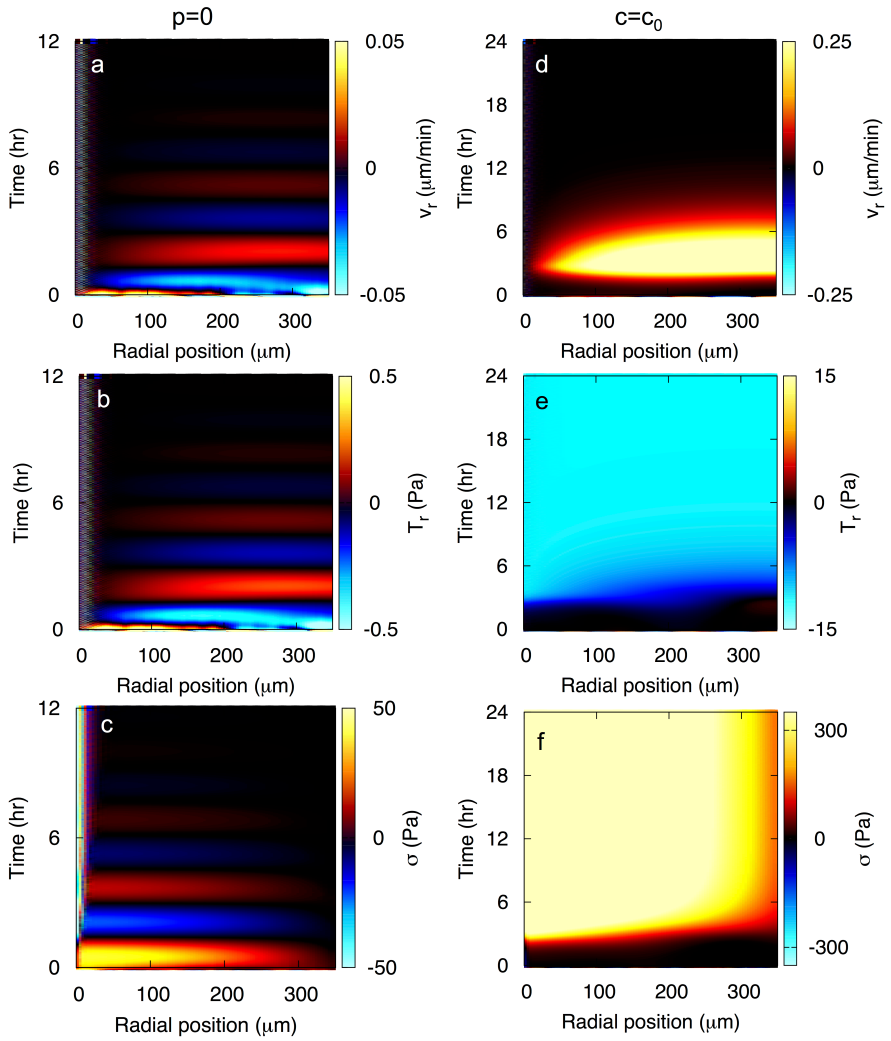

FIGURE 4.6: Limiting cases of the minimal physical model. (a–c) **u**-c model: Deformation **u** is coupled to c only. The polarization field **p** is set to zero and $\tau = 0.12$ hrs. Rest of the parameters are the same as in Table 1. In this case we obtain standing waves seen in the kymograph of velocity (a) qualitatively similar to our experiments. However, the traction (b) is proportional to velocity and is very different from the traction observed in our experiments. The monolayer tension (c) oscillated out of phase with velocity with both positive and negative values in disagreement to our experimental data. (d–f) **u**-**p** model: Deformation **u** is coupled to **p** only with the concentration field c set to its equilibrium value c_0. Simulation parameters are the same as in Table 1. In this case no wave-like behavior is obtained, indicating that the feedback between mechanical strain and the regulatory biochemistry of c is essential to explain the presence of wave-like dynamics.

aligned with the direction of local traction 4.5. In the limiting case $c = c_0$, when the deformation is only coupled to , no oscillatory behavior is observed (Fig. 4.6d-f). However, if the deformation is only coupled to the concentration field, the traction is proportional to velocity, which contradicts our experimental observations (Fig. 4.6a-c). This indicates that the polarization field is crucial to capture the misalignment between traction and velocity. Thus coupling of the deformation to both the concentration field and the polarization field is required to capture the experimentally observed distribution

of tractions, which pointed inwards at the exterior of the cell island and oscillated between outwards and inwards within the bulk of the island (Fig. 4.4 right frame). To test the model's prediction that a feedback between mechanical strain and cellular

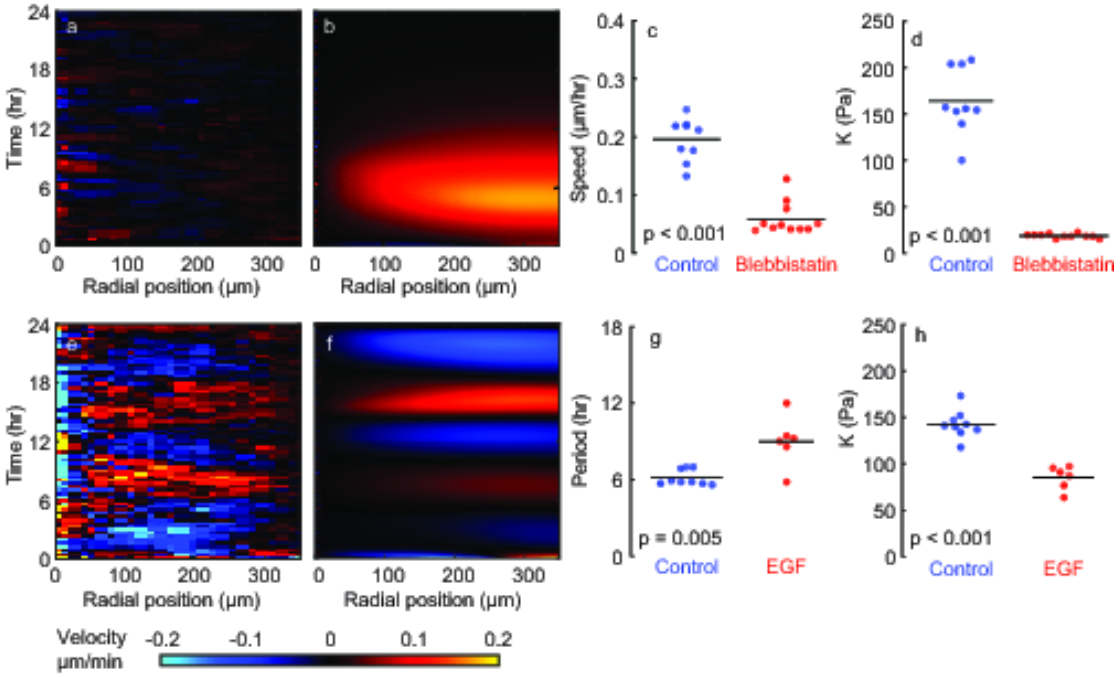

FIGURE 4.7: The waves of collective motion and elasticity in the monolayer depend on the contractile activity of the cells. (a) Kymograph of radial velocity after treatment with blebbistatin shows reduction in speed and elimination of oscillatory waves of radial motion. (b) Simulated kymograph of radial velocity using the model with no feedback between strain and contractility ($\alpha = 0$) also shows elimination of waves. (c, d) Treatment with blebbistatin reduces root-mean-square speed of cells by a factor of ∼4 (c) and reduces the modulus K to a nearly negligible value (d). (e) Kymograph of radial velocity for an island treated with EGF (20 ng/mL) and (f) simulated kymograph with reduced values of the parameters and . (g) Compared with control, EGF increased the period of oscillation. (h) Relative to control, treatment with EGF decreased the effective elastic modulus K. For the plots in (c), (d), (g), and (h) each dot corresponds to a different cell island. P values are computed using a rank sum statistical test.

contraction generates collective oscillations, we inhibited contraction with the myosin-II inhibitor blebbistatin (20 μM). For an expanding island, blebbistatin has no effect on the speed of migration [7], but in confined islands blebbistatin reduced each cells speed (Fig. 4.7a,c). Further, blebbistatin eliminated the multicellular oscillations (Fig. 4.7a), and reduced the modulus K to ∼20 Pa (Fig. 4.7d). This observation is consistent with our model which predicts that the coupling between strain and contractility yields an effective modulus [110]

$$K \approx B + \alpha(\beta\tau + fw/2ah) \tag{4.6}$$

larger than the modulus B of the monolayer in the absence of contractility. Removing the coupling between strain and contractility by setting $\alpha = 0$ eliminated the oscillatory

waves in our model (Fig. 4.7b). These findings suggest that the elasticity is primarily active: the oscillations in motion cause oscillations in cellular strain, which through active contraction cause oscillations in tension. To further test this, we sought to connect changes in elasticity with the motion. We found that EGF (20 ng/mL) increased the period of oscillation (Fig. 4.7e,g). In an oscillatory system, modulus and period are inversely related, and in accord with increasing the period, treatment with EGF decreased the modulus K (Fig. 4.7h). When we reduced the magnitude of the constants that couple tension and strain, we saw, similarly, an increase in the period of oscillations (Fig. 4.7f). From these findings- that the waves require contraction and that the period depends inversely on modulus- we conclude that the elasticity is not passive in nature; rather, it is the result of myosin-driven contractility within the cell.

4.4 Misalignment Between Cellular Tractions and Cellular Velocities

To investigate the relationship between cellular tractions and velocities, we confined monolayers of Madin-Darby Canine Kidney (MDCK) cells to circular islands (diameter = 700 μm) of adhesive collagen type I. We measured cell velocities with particle image velocimetry and simultaneously measured tractions with traction force microscopy [107, 116, 117]. Similar to reports in a previous study [108], we observed sustained oscillations of inward and outward cellular motion comprising waves with a period of 6 hours (Fig. 4.8b). To visualize the data at all points in space and time, we averaged the velocity data over the azimuthal angle to collapse all spatial data onto a single axis specifying the radial position. We then plotted the data over time to generate a kymograph. As shown in the kymograph of velocity (Fig. 4.8d), the cellular motion was highly coordinated with standing waves of outward and inward collective motion, similar to seiches observed in lakes or other confined bodies of water. Surprisingly, even though the monolayer velocity varied little with the radial position at a given time, tractions were organized in a standing wave with finite wavelength (Fig. 4.8e). While the tractions at the perimeter of the island pointed radially inward, tractions at any point within the bulk of the island oscillated radially inward and outward over time akin to the velocity field. At the perimeter of the island all cells applied inward-pointing tractions (Fig. 4.8c), indicating that these cells pulled themselves toward the exterior free space, a behavior called kenotaxis [86]. But across the island the correlation between traction and velocity was negligible (typical correlation coefficient magnitude $|R| < 0.1$, Fig. 4.81b-c). Furthermore, the angles between the directions of velocity and traction showed a nearly uniform distribution across the monolayer (Fig. 4.8f), indicating that the orientation of each cells traction is not linked solely to its velocity. To investigate

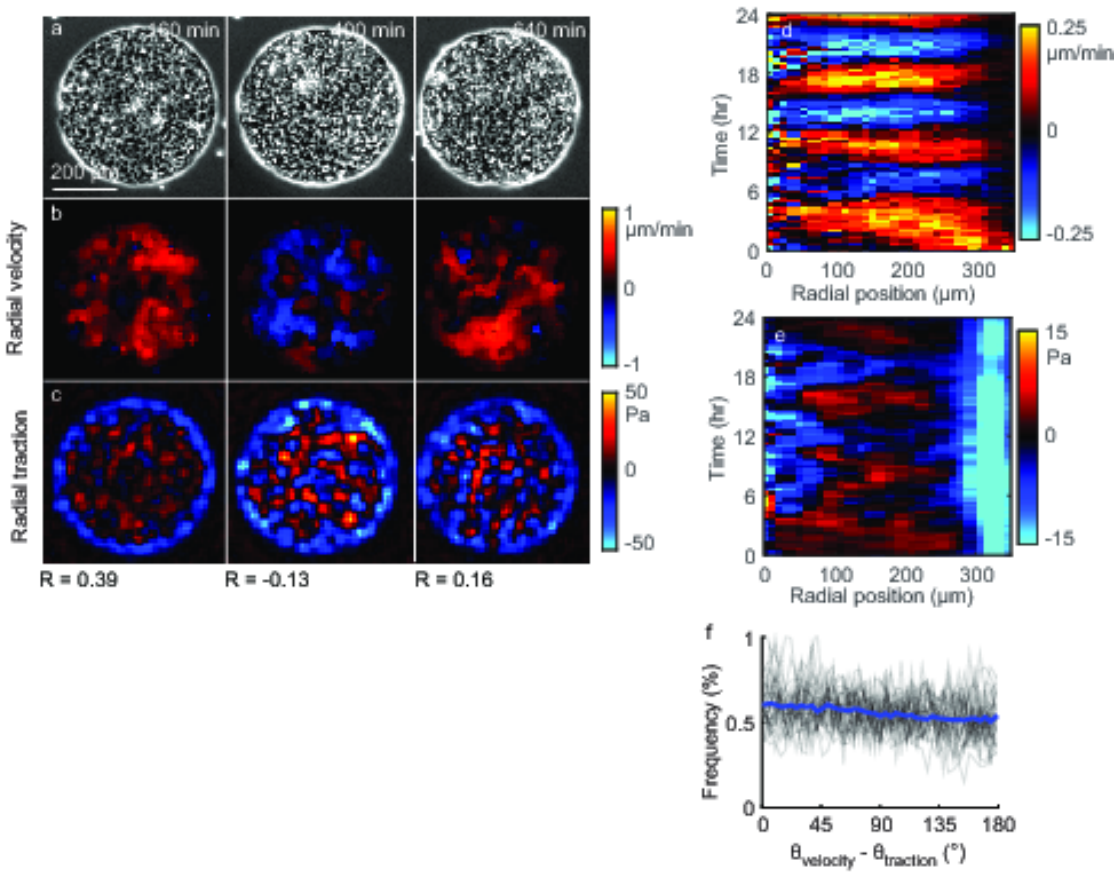

FIGURE 4.8: Tractions do not align with local cellular motions. (a) Phase contrast images of a confined cell monolayer. Time zero corresponds to the first image collected. (b, c) The radial components of velocity (b) and traction (c) are uncorrelated with one another. At some time points (e.g. 160 min), the Pearsons correlation coefficient R is positive, and at other time points (e.g. 400 min) it is negative. (d) The kymograph shows the radial velocity as a function of position and time. Red and blue bands indicate oscillating outward and inward motion. (e) Kymograph of radial traction showing that cells at the perimeter apply tractions that point inward, while cells within the bulk apply tractions that oscillate between inward and outward. (f) Histogram of the angle between the velocity and traction vectors. Each gray line shows a single point in time for the cell island; the blue line shows all points in time.

further the relationship between traction and velocity, we considered cellular motion within an expanding cellular island wherein the cells were not restricted by a boundary. We seeded cells onto a mask with 700 m holes placed atop a compliant polyacrylamide gel coated with collagen type I. As shown previously in Ref. [83], removing this mask induces cell migration into the newly created free space. Upon sensing the free space created by mask removal, cells located at the perimeter of the island migrated first, and their outward motion caused cells just inside the perimeter to follow (Fig. 4.9). Over time, more and more cells began to move, creating a wave of radial motion that propagated from the perimeter to the center of the island (Fig. 4.8b,d), similar to the waves of motion observed for cells in a rectangular monolayer [7]. Much like the cells in the confined islands, the cells near the perimeter of the expanding islands applied inward

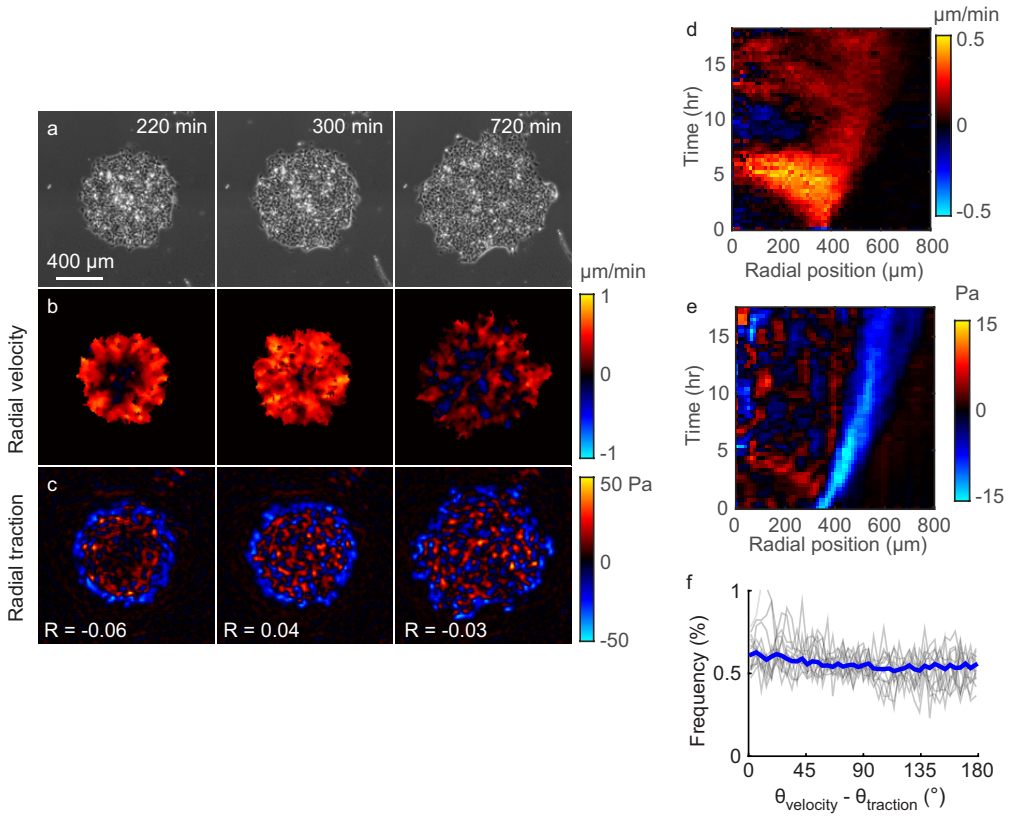

FIGURE 4.9: In expanding cellular monolayers, cellular tractions align in a different direction than cellular velocities. (a) MDCK cells are micropatterned into 700 μm islands using a PDMS mask on a polyacrylamide gel. When the mask is removed, the cells migrate outward. Times are in minutes after removing the mask. (b) Cell velocities are measured using particle image velocimetry, and the radial component of the velocity vector is plotted. The positive direction (red) represents outward motion. At early times (220 min), cells at the periphery move outward; later (300 min), all cells move outward. Once the island is fully spread (720 min), cells move either inward or outward. (c) Radial component of traction applied by the cells to the substrate. Areas in blue indicate regions where the cells pull inward on the substrate; this inward force, if unbalanced, would accelerate the cells outward. The relationship between velocity and traction is evaluated with Pearson's correlation coefficient, R. (d, e) Kymographs of radial velocity (d) and radial traction (e). At all points in time, neither the spatial map of tractions (c) nor the averaged tractions (e) correlate with the velocity. (f) Histogram of the angle between the velocity and traction vectors. Each gray line shows a single point in time for the cell island; the blue line shows all points in time.

tractions so as to pull themselves toward free space (Fig. 4.9c,e). For cells in the bulk of the expanding island, however, we observed no alignment between directions of traction and velocity (Fig. 4.9f). These findings point to the notion that cells tend to apply local propulsive forces in a direction that can deviate systematically from the direction of local cellular motion. In the specific case of cells near the edge of the freely expanding monolayer, local tractions and velocities were aligned, but elsewhere they were not. Why this independence of orientations? In contrast to previous models [15, 118] which predict that cells apply traction along a gradient of cellular density, our data showed no correlations between the orientations of cellular tractions, velocities, or gradients in

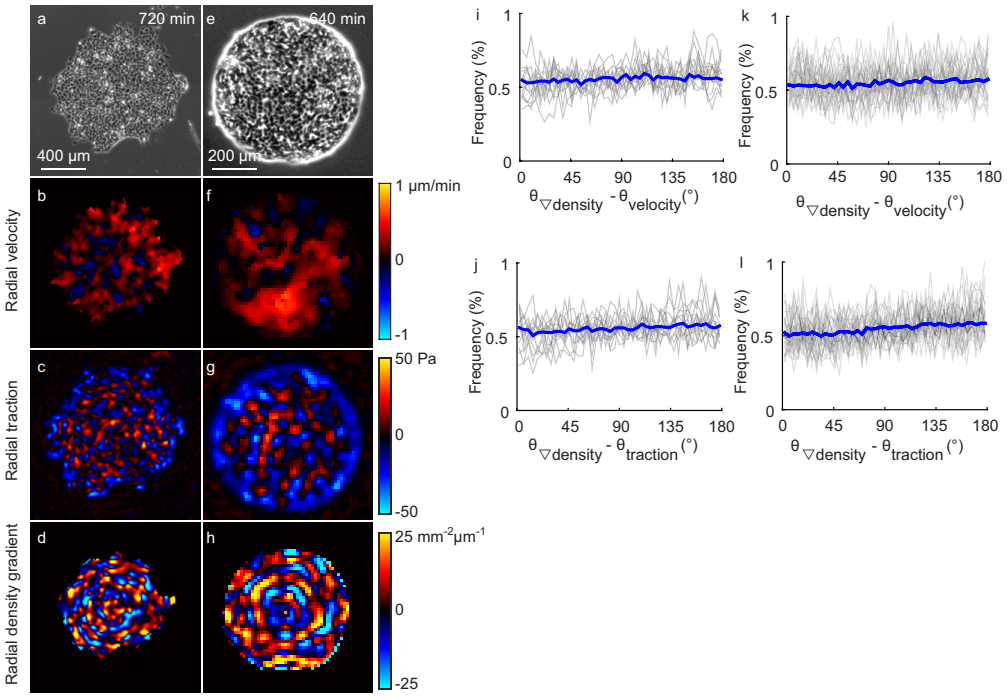

FIGURE 4.10: Gradients in local number density do not drive collective motion in expanding or confined monolayers. (a) Phase contrast image of MDCK cells in an expanding island 720 min after removing the mask. (b–d) The radial components of velocity (b) and traction (c) are uncorrelated with the radial component of the density gradient (d) (Pearson's correlation coefficient R = -0.06 and 0.07, respectively). (e–h) For a confined monolayer (e), radial velocity (f) and radial traction (g) are similarly uncorrelated with the radial component of density gradient (h) (Pearson's correlation coefficient R = 0.03 and -0.12, respectively). (i–l) Histograms of the angle between the directions of density gradient and velocity (i, k) or density gradient and traction (j, l) for the expanding (i, j) or confined (k, l) islands. Each gray line shows the histogram for a single point in time for a cell island; the blue lines show histograms for all points in time. Computation of all density gradients reports data points located at least 50 μm from the boundary of the cell island so as to avoid errors in computing the density gradient near the outside of the island where density is zero.

number density (Fig. 4.10).

4.5 Discussion

Here we have studied motions and forces in a confined monolayer of epithelial cells. Spontaneous oscillations arise wherein cells alternated between outward and inward correlated motions that resemble the sloshing seiches that are observed in confined bodies of water. The direction of local cellular velocity is generally independent of the direction of local traction, thus indicating that the relationship between force and motion requires additional state variables. Two cellular state variables, the concentration of contractile elements and the polarization of cell motion, were introduced to reproduce the experimental results. The coupling between the cellular strain and chemical concentration

generates effective inertia which, together with cellular elasticity, supports the oscillatory waves of motion observed in the experiments. Decreasing the elastic modulus with EGF increased the period of oscillation (Fig. 4.7g,h), in agreement with the theory.

Elasticity of the monolayer has been previously attributed to a passive spring-like behavior of the cytoskeleton, its contractile apparatus, and cell-cell adhesions [7, 108]. In contrast, our model now incorporates a feedback between cellular strain and contractility such that a local increase in cell area induces larger contractility. This mechanism is consistent with recent experiments on single cells [93] and multicellular clusters [85, 119], which show that cells with larger area are more contractile than cells with smaller area. When we suppressed cell contractility with the myosin-II inhibitor blebbistatin, the elastic modulus decreased by an order of magnitude (Fig. 4.7d), and the waves were suppressed (Fig. 4.7a). From this observation we conclude that the elasticity required to generate the waves is not simply a passive spring-like behavior; rather it results from the active contractile elements inside the cell [93]. Adding blebbistatin reduced the average cell speed in these confined islands, but such a reduction in speed is unlikely to be the mechanism that inhibits the oscillations in cellular motion. A previous study showed that blebbistatin in an expanding cellular island has no effect on cell speed, but it does eliminate propagating waves of contractile tension [7]. This observation agrees with our finding that active cell contraction is required to generate the oscillatory waves. The

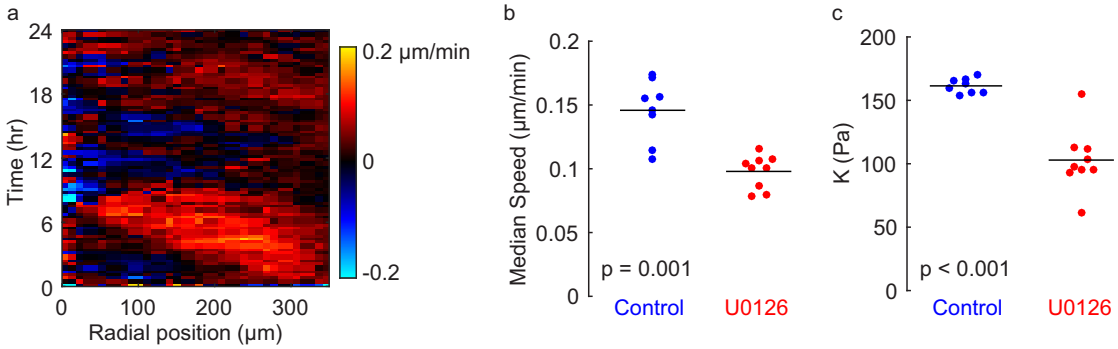

FIGURE 4.11: The ERK inhibitor U0126 (10 μM) decreases the velocity and eliminates the waves. (a) Kymograph of velocity shows no waves of cellular motion are present. (b) Compared to control, cell islands treated with U0126 move at a slower speed. (c) Compared to control, treatment with U0126 reduces the elastic modulus K. For the plots in (b) and (c), each dot corresponds to a different cell island. P values are computed using a rank sum statistical test.

molecular mechanisms that link changes in cellular stretching to changes in contractile tension are unknown, but theoretical studies [18] and experimental evidence point to ERK MAP kinase (ERK1/2) as being associated with extension of muscle tissue [120] and stretching of stress fibers [121]. Moreover, when a monolayer begins to expand into free space, a wave of ERK1/2 phosphorylation propagates from the monolayers free edge into the bulk [122, 123] at a speed approximately the same as that of the waves of

cellular motion that occur in our experiments of expanding cellular islands (Fig. 4.9d) and have been reported elsewhere [7]. This slow-moving wave results not from damage to the monolayer, but rather from the free space offered to the monolayer's edge[123]. When we inhibited ERK1/2 with U0126 (10 M), the effective modulus decreased by a factor of two, and collective oscillations were suppressed (Fig. 4.11).

Collective cellular oscillations similar to the ones described here have been reported by *Deforet et al.* [108], who performed stochastic particle-based simulations that balanced the forces of inertia, friction, intercellular adhesions and active propulsion. In their simulation each cell was given a tendency to adapt its velocity to that of its nearest neighbors. Although the model by Deforet et al. and the one presented here are both based on local force-balance, they differ in spirit. Instead of simulating the dynamics of individual cells, we propose a continuum model formulated in terms of a few coarse-grained fields such as traction and velocity, which are measured directly in the experiments. Our model contains only a small number of parameters that represent effective material properties of the monolayer and describe the combined effect of a number of signaling pathways. The model makes testable predictions that provide a way of correlating the macroscopic parameters of the theory with specific pathways.

Oscillatory or wavelike motion requires second order differential equations in time, corresponding to the tradeoff between two independent time scales. The dynamics of cellular monolayers is overdamped, hence governed by a first order differential equation, with a single time scale determined by the interplay of viscous friction and elasticity. Until now the origin of the second time scale required for oscillatory behavior has remained mysterious. Deforet et al. accounted for the second time scale by introducing cellular inertia [108]. *Serra-Picamal et al.* accounted for the second time scale by assuming stretched cells became fluidized (i.e., they flowed under tensile forces) for a specified period of time [7]. There is evidence that cells fluidize when stretched and unstretched quickly [124–126], but whether stretches due to slow cellular motion induce fluidization remains an open question. Our model and experiments point to a second time scale that comes from the mechanochemical feedback [18] between the local strain and the rate of change in contractile tension. This feedback mechanism results in self-sustained periods of stiffening and fluidization in the cell monolayer [110].

Dynamics of the chemical concentration does not explain the apparent independence between the local orientations of traction and velocity (Fig. 4.8f, Fig. 4.9f, Fig. 4.12). Whereas Kim et al. showed velocity and tractions do not align near to a boundary []Kim2013, we show here that an angle of misalignment between traction and velocity occurs even in the absence of a boundary. The histogram of the angle between traction and velocity at all points in time (Fig. 4.8f, blue line) shows a very small peak near

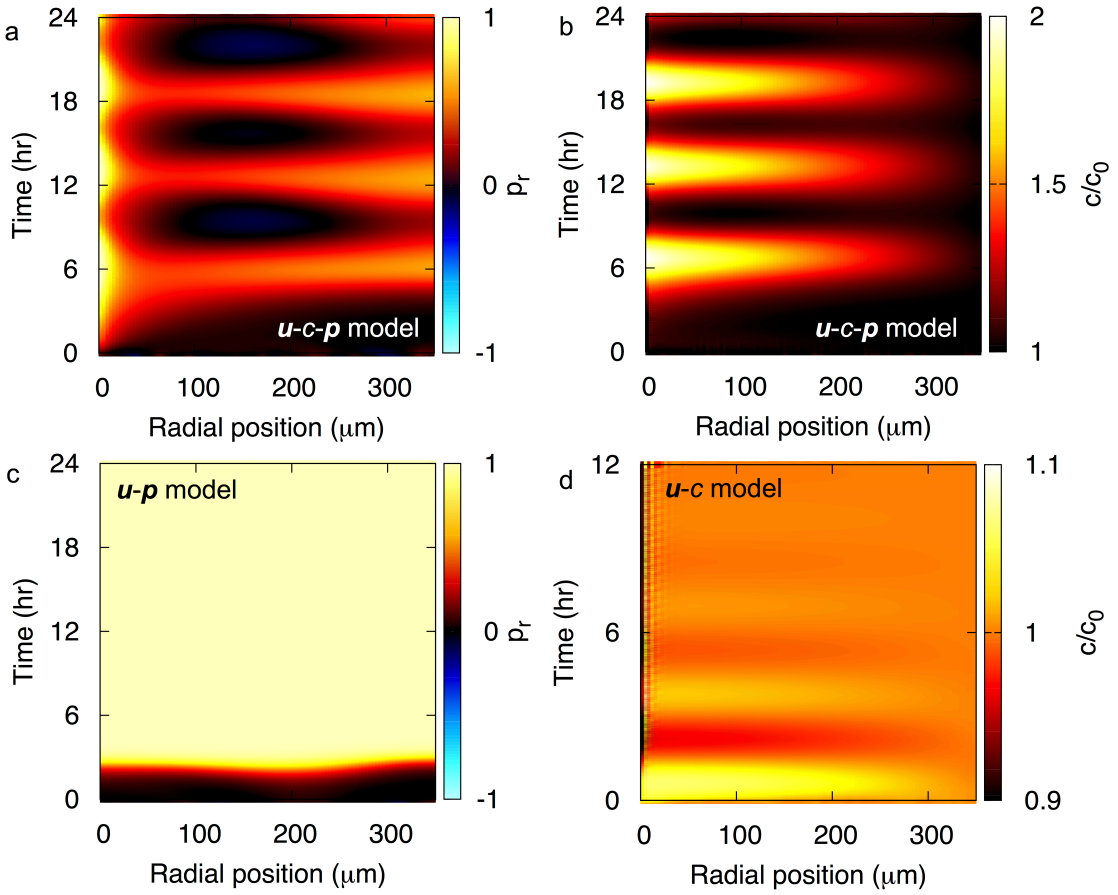

FIGURE 4.12: Dynamics of the internal state variables in the cell monolayer. (a) Kymograph of the polarization field in the full **u**-*c*-**p** model shows that cells at the boundary and at the center of the monolayer are polarized outwards separated by a band of inward polarized cells. (b) Kymograph of the concentration field in the full **u**-*c*-**p** model showing oscillations similar to the monolayer tension. (c) In the absence of coupling to c, the polarization field is uniform and points radially outward. (d) Kymograph of the concentration field in the absence of coupling to polarization field.

zero, indicating a slight tendency for cells to pull on the substrate in the same direction that they move. This occasional alignment between motion and traction is consistent with the presence of a viscous drag exerted by the moving cells onto the substrate, as described by our model and others [18, 89, 90, 110]. In these models the viscous drag term connects tractions to motion, and thus our observation of occasional alignment between traction and velocity serves as a confirmation of this connection. To account for the deviation between the local directions of traction and velocity, we propose a vector polarization field that locally directs the cellular motion. Other theoretical models have also incorporated a cell polarization field defining the orientation of an anisotropic dipole-like contractile stress [89], with dynamics governed by general nonlinear hydrodynamic equations of polar liquid crystals [18, 127]. In contrast, our work considers a minimal model where cell polarization does not generate shear stresses, in agreement with our experimental data that show an isotropic distribution of the monolayer stress

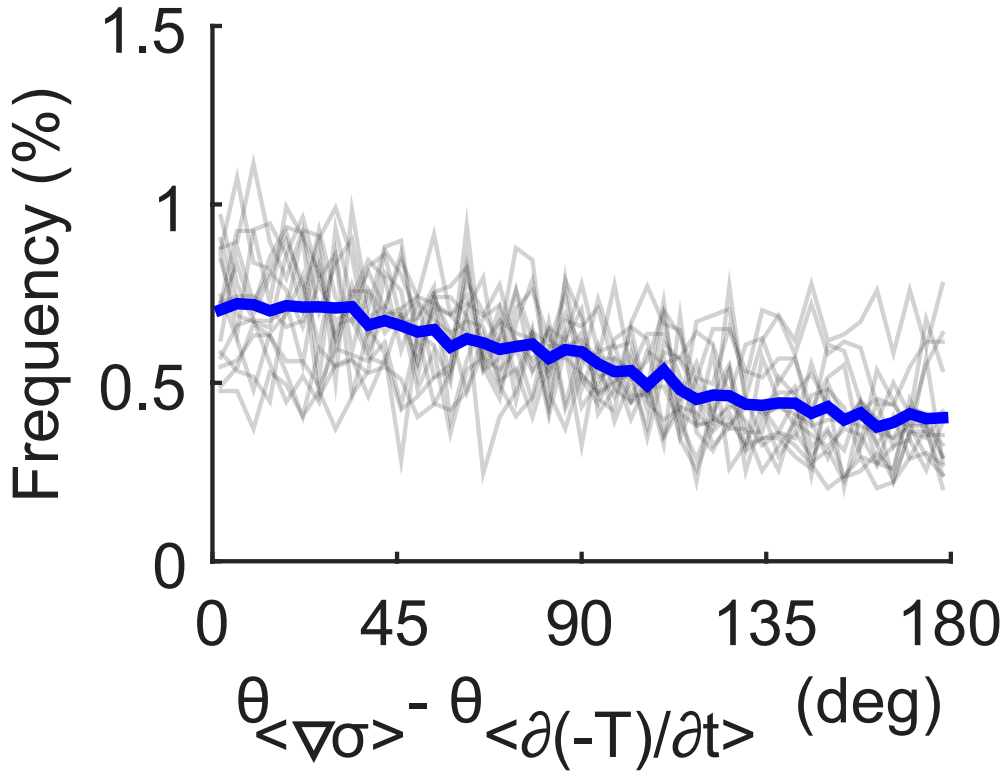

FIGURE 4.13: Cells polarize along gradients of contractility. The difference in the orientations of the gradient of tension, $\theta_{\langle\nabla\sigma\rangle}$, and the opposite of the time derivative of traction, $\theta_{\langle\partial(-\mathbf{T})/\partial t\rangle}$, is plotted as a histogram for various points in time (gray lines) and for all time points (blue line). Here, the angle brackets represent a time average over one period of oscillation. The peak near zero indicates that directions of $\langle\nabla\sigma\rangle$ and $\langle\partial(-\mathbf{T})/\partial t\rangle$ tend to align, in agreement with the model. The alignment between directions of $\langle\nabla\sigma\rangle$ and $\langle\partial(-\mathbf{T})/\partial t\rangle$ means that the cell tractions evolve in time so as to propel the cells towards regions of high tension.

field. Importantly, we identify two physical mechanisms that control the dynamics of cell polarization. First, cells tend to polarize their traction toward free space, consistent with kenotaxis [86]. Our model accounts for kenotaxis in the first term on the right hand side of Eq. (4.5), which tends to polarize the monolayer toward free space. Secondly, the polarization field evolves in time so as to locally align towards regions of high contractile tension in the monolayer (Fig. 4.13). These two tendencies are required to reproduce the spatial patterning of the traction field (Fig. 1e, Fig. 3e), and they provoke the question of what molecular mechanism generates the polarization. The cytoskeletal protein merlin may be involved, as the feedback between merlin and Rac1 has been shown to direct formation of lamellipodia in collective cellular migration [128]. If merlin indeed polarizes the cells, it is likely only one of several molecular mechanisms controlling the forces that drive collective cellular motion.

Here we have found that the various biological mechanisms controlling the waves of collective motion combine together to relate force and motion through two physical

variables, one controlling intracellular contractility and the other polarizing cell motion. These two state variables are present within each cell, but perhaps even more striking is the fact that each cell coordinates these state variables with its neighbors to generate emergent waves of correlated motion that span multiple cell diameters. Emergent phenomena like these multicellular waves control the motion and final positioning of the cellular collective, and thus they are likely to play a key role in development and disease. The two internal variables that we describe here cell contraction and polarization provide a framework for further investigation.

Appendix B

B.1 Materials and Methods

B.1.1 Cell Culture

Madin-Darby Canine Kidney (MDCK) type II cells, expressing GFP with a nuclear localization signal (pAcGFP1-Nuc vector, Clontech), were supplied by A. Pegoraro and D. Weitz (Harvard University). The cells were maintained in low glucose Dulbecco's Modified Eagle's medium (12320-032; Life Technologies, Carlsbad, CA) with 10% fetal bovine serum (Corning) and 1% penicillin-streptomycin (Sigma-Aldrich. St. Luois, MO) in an incubator at 37° C and 5% CO_2.

B.1.2 Preparation of polyacrylamide substrates

Polyacrylamide gels with Young's modulus of 6 kPa and thickness of 100 μm were polymerized by preparing a solution of 5.5% weight/volume (w/v) acrylamide (Biorad Laboratories, Hercules, CA), 0.20% w/v bisacrylamide (Biorad Laboratories), 0.014% w/v fluorescent particles (diameter=0.5 μm, carboxylate-modified; Life Technologies),0.05% w/v ammonium persulfate (Biorad Laboratories), and 1/2000 volume/volume TEMED (Biorad Laboratories). The gel solution was pipetted onto no. 1.5 glass bottom dishes (In Vitro Scientific, Mountain View, CA), a glass coverslip (no. 1 thickness, 18-mm diameter circle) was placed on top, and the dishes were centrifuged upside down so that the fluorescent particles collected at the top surface of the gel. The gels were functionalized with type 1 rat tail collagen (BD Biosciences, Franklin Lakes, NJ; 0.01 mg/mL, 1 mL per 18-mm diameter gel) using the covalent crosslinker sulfo-SANPAH (Pierce Biotechnology, Waltham, MA) as described in Ref. [107].

B.1.3 Micropatterning expanding and confined cellular islands

Masks were prepared with circular holes (diameter = 700 μm) using standard techniques in soft lithography, similar to those described previously in Ref. [7]. Silicon-photoresist masters were custom fabricated (MicroFit, Seongnam-si, Gyeonggi-do, Korea), and Polydimethylsiloxane (PDMS) (Sylgard 184, Dow Corning, Midland, MI) was poured onto the masters to cure overnight on a hot plate at 80°C. The PDMS masks were sterilized with 70% ethanol and incubated at 37°C in 2% Pluronic F-127 (Sigma-Aldrich) for 4 hours to prevent cell adhesion to the masks. For expanding islands, masks were placed on the collagen-coated polyacrylamide gels, and a 200 μL droplet of cell suspension ($4x10^5$ cells total) was placed on each mask. The gels were transferred to a $37°C/5\%$ CO_2 incubator for 45 min for the cells to adhere to the collagen. Afterward, the 200 L droplets were aspirated off of the PDMS masks, the masks were removed with tweezers, and the gels were rinsed with PBS before adding 3 mL fresh medium. For confined islands, masks were placed onto the polyacrylamide gels before functionalizing with collagen, thus leaving a circular island of collagen to which the cells adhered. Imaging of the cell monolayers began approximately one hour after seeding and continued for $\sim$ 30 h.

B.1.4 Microscopy

Images of the cells, nuclei, and beads were captured every 20 minutes using phase contrast (for cells) or fluorescent (for nuclei and beads) microscopy using a DMI6000B microscope with a 5x NA 0.12 objective and a DFC345FX CCD camera (Leica Microsystems, Wetzlar, Germany). Fluorescent particles and cell nuclei were imaged with fluorescence; cells were imaged with phase contrast. The imaging environment was maintained at $37°C/5\%CO_2$ in a heated enclosure (PeCon, Erbach, Germany). For experiments with expanding cellular islands a 2x2 grid of images was captured and stitched together using the freely available Fiji distribution of ImageJ (`http://fiji.sc/Fiji`) [129]. After each time lapse experiment, cells were removed from the polyacrylamide substrates by incubating in 0.05% trypsin for 20 min, and images were collected of the fluorescent particles; these images captured a stress-free reference state of the polyacrylamide substrates for subsequent computation of tractions.

B.1.5 Measuring cell velocity and rate-of-strain

The velocity fields were measured using custom particle image velocimetry (also called digital image correlation) software of phase contrast images written in Matlab (The

Mathworks, Natick, MA). Interrogation windows of 64x64 pixels were used; this window size allowed for a spatial resolution of $\sim$ 16 pixels (14 μm). Boundaries of the cell islands were detected automatically using a previously described protocol [130]. The rate-of-strain tensor was computed by numerically differentiating the velocity fields in space.

B.1.6 Traction force microscopy and monolayer stress microscopy

Displacements of the particles were measured using digital image correlation, and tractions exerted between the cell layer and its substrate were computed using unconstrained Fourier Transform Traction Microscopy [116] taking into account the effects of finite substrate thickness [107, 117]. From these measured tractions we computed the distribution of internal stresses within the cell layer using Monolayer Stress Microscopy (MSM) [109, 113].

MSM rests upon the main assumptions that the cell layer is flat, continuous and thin. Regardless of material properties of the cell layer, including any effects of nonlinearity and viscoelasticity, Newtons laws in one dimension demand that these internal stresses and boundary traction stresses must always remain in precise balance, and the MSM solution in that case is therefore exact [109, 113]. In two dimensions matters are slightly more complicated because the Poisson effect makes the solution inexact. Nevertheless, the sensitivity to the Poisson effect has been shown to be quite small, and the solution has been shown to be insensitive to a remarkably wide range of assumptions about material properties of the cell layer itself, its nonlinearity, and its viscoelasticity [109, 113]; this finding was further validated independently by *Zimmermann et al.* [112], who used a particle-based simulation to show that the stresses in the simulation are recovered by MSM with a high degree of accuracy. In two dimensions, three independent components of the stress tensor within the monolayer are obtained by solving three coupled equations. Two of those equations describe force balance, which make no assumptions about the properties of the monolayer [109, 113]. The third equation is the compatibility of the deformation field. Displacements, tractions, and stresses are measured at the same spatial resolution as the velocity field, 14 μm.

B.1.7 Measuring cell area and density

The position of each cell's nucleus was computed from the fluorescent images of nuclei using the watershed transform in Matlab. For each cell, the distance between its nucleus and the nuclei of the nearest 6 neighbors was computed and averaged; this distance was taken to be the diameter of that cell. From each cells diameter, its area was computed.

Density is computed by taking the inverse of cell area. To compute the gradient in density, each 3x3 window of data points is fit to a linear equation in the x direction and to a second linear equation in the y direction. The slopes give the derivatives in the x and y directions, respectively.

B.1.8 Chemical treatments

Chemical treatments were blebbistatin (20 μM), U0126 (10 μM), and EGF (20 ng/mL). Blebbistatin and U0126 were dissolved in dimethyl sulfoxide (DMSO); EGF was dissolved in phosphate buffered saline (PBS). Blebbistatin and U0126 stock solutions were 20 mM and 10 mM, respectively. They were diluted by a factor of 1000 when added to the medium, leading to a DMSO concentration of 0.1% in the cell culture medium. All comparisons were made to matching concentrations of a vehicle control (DMSO or PBS).

B.2 Model parameters.

While the model parameters are cell-type dependent, they are chosen so as to quantitatively reproduce our experimental data on MDCK cell monolayers for traction, velocity and intercellular stress. Specifically, the radius of the cell monolayer is taken to be $R = 350$ μm and the values of the elastic moduli, B and G, and the contractile stress β are taken to be of the same order of magnitude with the experimentally measured effective elastic modulus K of the monolayer. The values of the timescales regulating the chemical dynamics, τ and α^{-1}, are tuned so as reproduce the experimentally measured time period of oscillations $\sim$6 hrs. The remaining values are chosen within the order of magnitudes reported in prior literature. A complete list of the parameter values is given in Table below.

B.3 Experimental validation of the model predictions.

- *Contractile activity generates effective elasticity and mechanical waves.* Our model predicts that the coupling between contractility and the monolayer strain yields an effective bulk modulus, $K = B + \alpha\tau(\beta + fw/2ah)$ that is greater than the passive bulk elastic modulus of the material [18]. Furthermore, in our model waves arise due to a local feedback between rate of production of c and mechanical strain in the monolayer. This is consistent with our experimental data which shows that the treatment with blebbistatin (an inhibitor of myosin-based contractility) reduces

Table 1: Model parameters.

Parameter	Physical Meaning	Numerical Value
ζ	Viscous friction with the substrate	0.2 Pa hr/μm
f	Propulsion force	10 Pa
R	Monolayer radius	350 μm
h	Monolayer thickness	3 μm
B	Bulk elastic modulus	300 Pa
G	Shear elastic modulus	200 Pa
β	Magnitude of the active stress	600 Pa
τ	Timescale of relaxation of c	1.17 hrs
α	Rate of production of c due to cell stretching	2.14 hr^{-1}
a	Rate of relaxation to a homogeneously polar state	0.78 hr^{-1}
κ	Stiffness constant characterizing the cost of local changes in $\mathbf{p}$	8.75 μm^2/min
w	Controls the rate of alignment of $\mathbf{p}$ with the gradients of c	2.08 μm/min

the effective elastic modulus K of the cell monolayer by an order of magnitude and eliminates the waves (Fig. 4 a–d).

- *Cell polarization aligns with the gradients of contractile tension.* Our minimal model incorporates feedback between $\mathbf{p}$ and c such that $\partial_t \mathbf{p} \propto \nabla(c/c_0)$. Because the active stress σ_a goes as $\log(c/c_0)$, we expect that $\partial_t \mathbf{p} \propto \nabla\sigma$. Furthermore, since $\mathbf{T} = \zeta\mathbf{v} - f\mathbf{p}$, and $\mathbf{v}$ averages to 0 over one period of oscillation, we expect that $\langle \partial(-\mathbf{T})/\partial t \rangle \sim \langle \nabla\sigma \rangle$, where the angular brackets denote time average over one period of oscillations. When we compare directions of $\langle \partial(-\mathbf{T})/\partial t \rangle$ and $\langle \nabla\sigma \rangle$, we find alignment (Fig. 4.13).

- *Cell polarization exists even in the absence of contractility.* Our experimental data show that after treatment with blebbistatin, the traction and the velocity field of the monolayer are misaligned on average, with the traction vectors pointing radially inward at the perimeter of the island and cell motion polarized radially outwards (Fig. B.1).

  This behavior of cells to polarize their motion radially outward is consistent with the results of the *u–p model* that reproduces the anti-alignment between traction and velocity in the absence of contractility (Fig. 4.6d,e).

- *Scaling of the time period with monolayer size.* A linear stability analysis of our continuum model predicts a characteristic frequency of oscillatory waves in the monolayer given by [110],

$$\omega_0(q) \simeq q\sqrt{hK/\tau\zeta}\,, \tag{B.1}$$

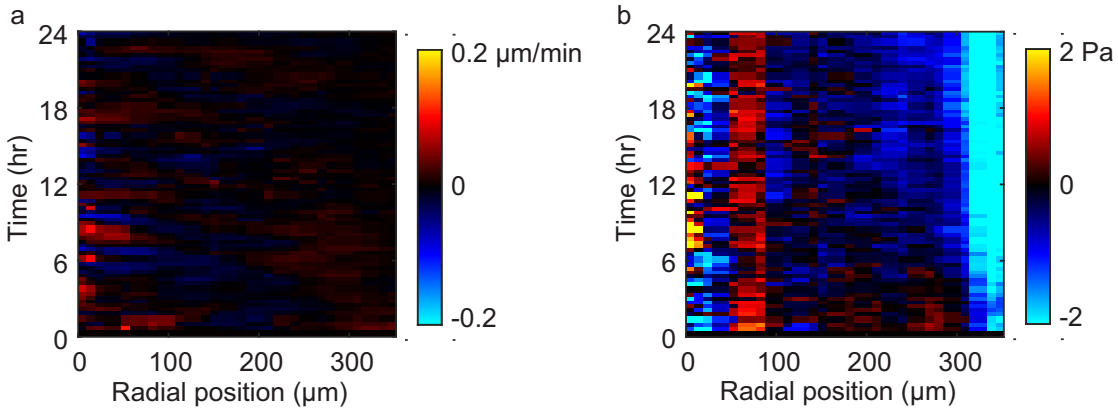

FIGURE B.1: Blebbistatin treatment. Kymographs of (a) radial velocity and (b) radial traction for a cell island treated with blebbistatin (20 μM). The tractions are generally aligned in the opposite direction as the radial velocity. The observed anti-alignment agrees with the model when contractility is inhibited (Fig.4.6d-f). In this figure, panel (a) is the same as Fig. 4.11a.

where q is the radial wave vector. At length scales comparable to the monolayer size, $q \simeq 1/R$, we get the following analytical expression for the time period,

$$T \simeq 2\pi R\sqrt{\tau\zeta/hK}\ . \tag{B.2}$$

Our model thus predicts a linear scaling relation between the time period of oscillations and the monolayer radius, in agreement with experimental measurements [7].

Bibliography

[1] Pramod A. Pullarkat, Pablo A. Fernández, and Albrecht Ott. Rheological properties of the eukaryotic cell cytoskeleton. *Physics Reports*, **449**(13), 29 – 53, 2007. Nonequilibrium physics: From complex fluids to biological systems III. Living systems.

[2] Emad Moeendarbary and Andrew R. Harris. Cell mechanics: principles, practices, and prospects. *Wiley Interdisciplinary Reviews: Systems Biology and Medicine*, **6**(5), 371–388, 2014.

[3] Revathi Ananthakrishnan and Allen Ehrlicher. The forces behind cell movement. *International journal of biological sciences*, **3**(5), 303, 2007.

[4] James E. N. Jonkman, Judith A. Cathcart, Feng Xu, Miria E. Bartolini, Jennifer E. Amon, Katarzyna M. Stevens, and Pina Colarusso. An introduction to the wound healing assay using live-cell microscopy. *Cell Adhesion & Migration*, **8**(5), 440–451, 2014. PMID: 25482647.

[5] Silvia Blacher, Charlotte Erpicum, Bndicte Lenoir, Jenny Paupert, Gustavo Moraes, Sandra Ormenese, Eric Bullinger, and Agnès Noel. Cell invasion in the spheroid sprouting assay: A spatial organisation analysis adaptable to cell behaviour. *PLOS ONE*, **9**(5), 1–10, 05 2014.

[6] Evanthia T. Roussos, Michele Balsamo, Shannon K. Alford, Jeffrey B. Wyckoff, Bojana Gligorijevic, Yarong Wang, Maria Pozzuto, Robert Stobezki, Sumanta Goswami, Jeffrey E. Segall, Douglas A. Lauffenburger, Anne R. Bresnick, Frank B. Gertler, and John S. Condeelis. Mena invasive (menainv) promotes multicellular streaming motility and transendothelial migration in a mouse model of breast cancer. *Journal of Cell Science*, **124**(13), 2120–2131, 2011.

[7] Xavier Serra-Picamal, Vito Conte, Romaric Vincent, Ester Anon, Dhananjay T. Tambe, Elsa Bazellieres, James P. Butler, Jeffrey J. Fredberg, and Xavier Trepat. Mechanical waves during tissue expansion. *Nature Physics*, **8**, 628–634, Jul 2012.

[8] Ray Keller. Shaping the vertebrate body plan by polarized embryonic cell movements. *Science*, **298**(5600), 1950–1954, 2002.

[9] Tadanori Mammoto and Donald E. Ingber. Mechanical control of tissue and organ development. *Development*, **137**(9), 1407–1420, 2010.

[10] Gabriel Fenteany, Paul A Janmey, and Thomas P Stossel. Signaling pathways and cell mechanics involved in wound closure by epithelial cell sheets. *Current Biology*, **10**(14), 831 – 838, 2000.

[11] Takanori Tsuji, Soichiro Ibaragi, and Guo-fu Hu. Epithelial-mesenchymal transition and cell cooperativity in metastasis. *Cancer Research*, **69**(18), 7135–7139, 2009.

[12] Cornelis J. Weijer. Collective cell migration in development. *Journal of Cell Science*, **122**(18), 3215–3223, 2009.

[13] Aaron F. Mertz, Yonglu Che, Shiladitya Banerjee, Jill M. Goldstein, Kathryn A. Rosowski, Stephen F. Revilla, Carien M. Niessen, M. Cristina Marchetti, Eric R. Dufresne, and Valerie Horsley. Cadherin-based intercellular adhesions organize epithelial cellmatrix traction forces. *Proceedings of the National Academy of Sciences*, **110**(3), 842–847, 2013.

[14] M. Lisa Manning, Ramsey A. Foty, Malcolm S. Steinberg, and Eva-Maria Schoetz. Coaction of intercellular adhesion and cortical tension specifies tissue surface tension. *Proceedings of the National Academy of Sciences*, **107**(28), 12517–12522, 2010.

[15] Julia C. Arciero, Qi Mi, Maria F. Branca, David J. Hackam, and David Swigon. Continuum model of collective cell migration in wound healing and colony expansion. *Biophysical Journal*, **100**(3), 535 – 543, 2011.

[16] Pernille Rørth. Collective cell migration. *Annual Review of Cell and Developmental Biology*, **25**(1), 407–429, 2009. PMID: 19575657.

[17] Peter Friedl and Darren Gilmour. Collective cell migration in morphogenesis, regeneration and cancer. *Nat Rev Mol Cell Biol*, **10**, 445–457, Jul 2009.

[18] Michael H. Köpf and Len M. Pismen. A continuum model of epithelial spreading. *Soft Matter*, **9**, 3727–3734, 2013.

[19] Jonathon Howard. *Mechanics of Motor Proteins and the Cytoskeleton*. Sinauer Associates, Inc, Sunderland, MA, 1 edition, 2001.

[20] Bruce Alberts, Alexander Johnson, Julian Lewis, Martin Raff, Keith Roberts, and Peter Walter. *Molecular Biology of the Cell*. Garland Science, 2002.

[21] Andrew R. Harris, Loic Peter, Julien Bellis, Buzz Baum, Alexandre J. Kabla, and Guillaume T. Charras. Characterizing the mechanics of cultured cell monolayers. *Proceedings of the National Academy of Sciences*, **109**(41), 16449–16454, 2012.

[22] Robert David, Olivia Luu, Erich W. Damm, Jason W. H. Wen, Martina Nagel, and Rudolf Winklbauer. Tissue cohesion and the mechanics of cell rearrangement. *Development*, **141**(19), 3672–3682, 2014.

[23] Thomas D. Pollard and William C. Earnshaw. *Cell Biology*. Elsevier, 2002.

[24] Daniel A. Fletcher and R. Dyche Mullins. Cell mechanics and the cytoskeleton. *Nature*, **463**, 485–492, Jan 2010.

[25] Masao Doi and Edwards Sam F. *The Theory of Polymer Dynamics*, volume 73. Oxford University Press, 1988.

[26] F Gittes, B Mickey, J Nettleton, and J Howard. Flexural rigidity of microtubules and actin filaments measured from thermal fluctuations in shape. *The Journal of Cell Biology*, **120**(4), 923–934, 1993.

[27] M. L. Gardel, J. H. Shin, F. C. MacKintosh, L. Mahadevan, P. A. Matsudaira, and D. A. Weitz. Scaling of f-actin network rheology to probe single filament elasticity and dynamics. *Physical Review Letters*, **93**, 188102, Oct 2004.

[28] B. Wagner, R. Tharmann, I. Haase, M. Fischer, and A. R. Bausch. Cytoskeletal polymer networks: The molecular structure of cross-linkers determines macroscopic properties. *Proceedings of the National Academy of Sciences*, **103**(38), 13974–13978, 2006.

[29] Rudolf Winklbauer. Cell adhesion strength from cortical tension – an integration of concepts. *Journal of Cell Science*, **128**(20), 3687–3693, 2015.

[30] Carmela Pasternak, James A. Spudich, and Elliot L. Elson. Capping of surface receptors and concomitant cortical tension are generated by conventional myosin. *Nature*, **341**, 549–551, Oct 1989.

[31] Jean-Yves Tinevez, Ulrike Schulze, Guillaume Salbreux, Julia Roensch, Jean-Franois Joanny, and Ewa Paluch. Role of cortical tension in bleb growth. *Proceedings of the National Academy of Sciences*, **106**(44), 18581–18586, 2009.

[32] Martin P. Stewart, Jonne Helenius, Yusuke Toyoda, Subramanian P. Ramanathan, Daniel J. Muller, and Anthony A. Hyman. Hydrostatic pressure and the actomyosin cortex drive mitotic cell rounding. *Nature*, **469**, 226–230, Jan 2011.

[33] Guillaume Salbreux, Guillaume Charras, and Ewa Paluch. Actin cortex mechanics and cellular morphogenesis. *Trends in Cell Biology*, **24**, 536–545, Oct 2012.

[34] Andrew G. Clark, Ortrud Wartlick, Guillaume Salbreux, and EwaK. Paluch. Stresses at the cell surface during animal cell morphogenesis. *Current Biology*, **22**, R484–R494, May 2014.

[35] Wanda Strychalski and RobertD. Guy. Intracellular pressure dynamics in blebbing cells. *Biophysical Journal*, **110**, 1168–1179, Mar 2016.

[36] AlexanderX. Cartagena-Rivera, JeremyS. Logue, ClareM. Waterman, and RichardS. Chadwick. Actomyosin cortical mechanical properties in nonadherent cells determined by atomic force microscopy. *Biophysical Journal*, **110**, 2528–2539, Jun 2016.

[37] F. C. MacKintosh, J. Käs, and P. A. Janmey. Elasticity of semiflexible biopolymer networks. *Physical Review Letters*, **75**, 4425–4428, Dec 1995.

[38] Cornelis Storm, Jennifer J. Pastore, F. C. MacKintosh, T. C. Lubensky, and Paul A. Janmey. Nonlinear elasticity in biological gels. *Nature*, **435**, 191–194, Mar 2005.

[39] Ovijit Chaudhuri, Sapun H. Parekh, and Daniel A. Fletcher. Reversible stress softening of actin networks. *Nature*, **445**, 295–298, Jan 2007.

[40] E L Elson. Cellular mechanics as an indicator of cytoskeletal structure and function. *Annual Review of Biophysics and Biophysical Chemistry*, **17**(1), 397–430, 1988. PMID: 3293593.

[41] Arne Schäfer and Manfred Radmacher. Influence of myosin {II} activity on stiffness of fibroblast cells. *Acta Biomaterialia*, **1**(3), 273 – 280, 2005.

[42] Jochen Guck, Stefan Schinkinger, Bryan Lincoln, Falk Wottawah, Susanne Ebert, Maren Romeyke, Dominik Lenz, Harold M. Erickson, Revathi Ananthakrishnan, Daniel Mitchell, Josef Käs, Sydney Ulvick, and Curt Bilby. Optical deformability as an inherent cell marker for testing malignant transformation and metastatic competence. *Biophysical Journal*, **88**(5), 3689 – 3698, 2005.

[43] Sarah E. Cross, Yu-Sheng Jin, Jianyu Rao, and James K. Gimzewski. Rnanomechanical analysis of cells from cancer patients. *Nature Nanotechnology*, **2**, 780–783, Dec 2007.

[44] Marija Plodinec, Marko Loparic, Christophe A. Monnier, Ellen C. Obermann, Rosanna Zanetti-Dallenbach, Philipp Oertle, Janne T. Hyotyla, Ueli Aebi, Mohamed Bentires-Alj, Roderick Y. H. Lim, and Cora-Ann Schoenenberger. The

nanomechanical signature of breast cancer. *Nature Nanotechnology*, **7**, 757–765, Aug 2012.

[45] Christian Rotsch and Manfred Radmacher. Drug-induced changes of cytoskeletal structure and mechanics in fibroblasts: An atomic force microscopy study. *Biophysical Journal*, **78**(1), 520 – 535, 2000.

[46] Sarah E Cross, Yu-Sheng Jin, Qing-Yi Lu, JianYu Rao, and James K Gimzewski. Green tea extract selectively targets nanomechanics of live metastatic cancer cells. *Nanotechnology*, **22**(21), 215101, 2011.

[47] Karen E Kasza, Amy C Rowat, Jiayu Liu, Thomas E Angelini, Clifford P Brangwynne, Gijsje H Koenderink, and David A Weitz. The cell as a material. *Current Opinion in Cell Biology*, **19**(1), 101 – 107, 2007. Cell structure and dynamics.

[48] R.E. Mahaffy, S. Park, E. Gerde, J. Käs, and C.K. Shih. Quantitative analysis of the viscoelastic properties of thin regions of fibroblasts using atomic force microscopy. *Biophysical Journal*, **86**(3), 1777 – 1793, 2004.

[49] S. Park, D. Koch, R. Cardenas, J. Käs, and C.K. Shih. Cell motility and local viscoelasticity of fibroblasts. *Biophysical Journal*, **89**(6), 4330 – 4342, 2005.

[50] Jordi Alcaraz, Lara Buscemi, Mireia Grabulosa, Xavier Trepat, Ben Fabry, Ramon Farré, and Daniel Navajas. Microrheology of human lung epithelial cells measured by atomic force microscopy. *Biophysical Journal*, **84**(3), 2071 – 2079, 2003.

[51] Michael J. Rosenbluth, Wilbur A. Lam, and Daniel A. Fletcher. Force microscopy of nonadherent cells: A comparison of leukemia cell deformability. *Biophysical Journal*, **90**(8), 2994 – 3003, 2006.

[52] Andrew R Harris and G T Charras. Experimental validation of atomic force microscopy-based cell elasticity measurements. *Nanotechnology*, **22**(34), 345102, 2011.

[53] Michael P Sheetz. *Laser Tweezers in Cell Biology*, volume 55. Academic Press, San Diego, CA, 1998.

[54] Martial Balland, Alain Richert, and François Gallet. The dissipative contribution of myosin ii in the cytoskeleton dynamics of myoblasts. *European Biophysics Journal*, **34**(3), 255–261, 2005.

[55] Daniel Choquet, Dan P Felsenfeld, and Michael P Sheetz. Extracellular matrix rigidity causes strengthening of integrincytoskeleton linkages. *Cell*, **88**(1), 39 – 48, 1997.

[56] T. G. Mason, K. Ganesan, J. H. van Zanten, D. Wirtz, and S. C. Kuo. Particle tracking microrheology of complex fluids. *Physical Review Letters*, **79**, 3282–3285, Oct 1997.

[57] Soichiro Yamada, Denis Wirtz, and Scot C. Kuo. Mechanics of living cells measured by laser tracking microrheology. *Biophysical Journal*, **78**(4), 1736 – 1747, 2000.

[58] Yiider Tseng, Thomas P. Kole, and Denis Wirtz. Micromechanical mapping of live cells by multiple-particle-tracking microrheology. *Biophysical Journal*, **83**(6), 3162 – 3176, 2002.

[59] A. W. C. Lau, B. D. Hoffman, A. Davies, J. C. Crocker, and T. C. Lubensky. Microrheology, stress fluctuations, and active behavior of living cells. *Physical Review Letters*, **91**, 198101, Nov 2003.

[60] Brenton D. Hoffman, Gladys Massiera, Kathleen M. Van Citters, and John C. Crocker. The consensus mechanics of cultured mammalian cells. *Proceedings of the National Academy of Sciences*, **103**(27), 10259–10264, 2006.

[61] John C. Crocker and Brenton D. Hoffman. Multipleparticle tracking and twopoint microrheology in cells. In *Cell Mechanics*, volume 83 of *Methods in Cell Biology*, pages 141 – 178. Academic Press, 2007.

[62] Linhong Deng, Xavier Trepat, James P. Butler, Emil Millet, Kathleen G. Morgan, David A. Weitz, and Jeffrey J. Fredberg. Fast and slow dynamics of the cytoskeleton. *Nature Materials*, **5**, 636–640, Aug 2006.

[63] Gaudenz Danuser and Clare M. Waterman-Storer. Quantitative fluorescent speckle microscopy of cytoskeleton dynamics. *Annual Review of Biophysics and Biomolecular Structure*, **35**(1), 361–387, 2006. PMID: 16689641.

[64] Predrag Bursac, Guillaume Lenormand, Ben Fabry, Madavi Oliver, David A. Weitz, Virgile Viasnoff, James P. Butler, and Jeffrey J. Fredberg. Cytoskeletal remodelling and slow dynamics in the living cell. *Nature Materials*, **4**, 557–561, Jul 2005.

[65] Guoying Jiang, Angela H. Huang, Yunfei Cai, Monica Tanase, and Michael P. Sheetz. Rigidity sensing at the leading edge through v3 integrins and rptp. *Biophysical Journal*, **90**(5), 1804 – 1809, 2006.

[66] Benjamin D. Matthews, Darryl R. Overby, Robert Mannix, and Donald E. Ingber. Cellular adaptation to mechanical stress: role of integrins, rho, cytoskeletal tension and mechanosensitive ion channels. *Journal of Cell Science*, **119**(3), 508–518, 2006.

[67] Pablo Fernández, Pramod A. Pullarkat, and Albrecht Ott. A master relation defines the nonlinear viscoelasticity of single fibroblasts. *Biophysical Journal*, **90**(10), 3796 – 3805, 2006.

[68] Ning Wang, Iva Marija Tolić-Nørrelykke, Jianxin Chen, Srboljub M. Mijailovich, James P. Butler, Jeffrey J. Fredberg, and Dimitrije Stamenović. Cell prestress. i. stiffness and prestress are closely associated in adherent contractile cells. *American Journal of Physiology - Cell Physiology*, **282**(3), C606–C616, 2002.

[69] Jianping Fu, Yang-Kao Wang, Michael T Yang, Ravi A Desai, Xiang Yu, Zhijun Liu, and Christopher S Chen. Mechanical regulation of cell function with geometrically modulated elastomeric substrates. *Nature Methods*, **7**, 733–736, Sep 2010.

[70] Benedikt Sabass, Margaret L. Gardel, Clare M. Waterman, and Ulrich S. Schwarz. High resolution traction force microscopy based on experimental and computational advances. *Biophysical Journal*, **94**(1), 207 – 220, 2008.

[71] Jochen Guck, Revathi Ananthakrishnan, Hamid Mahmood, Tess J. Moon, C. Casey Cunningham, and Josef Käs. The optical stretcher: A novel laser tool to micromanipulate cells. *Biophysical Journal*, **81**(2), 767 – 784, 2001.

[72] Xavier repat, Zaozao Chen, and Ken Jacobson. Cell migration. *Comprehensive Physiology*, Oct 2012.

[73] Anne J. Ridley, Martin A. Schwartz, Keith Burridge, Richard A. Firtel, Mark H. Ginsberg, Gary Borisy, J. Thomas Parsons, and Alan Rick Horwitz. Cell migration: Integrating signals from front to back. *Science*, **302**(5651), 1704–1709, 2003.

[74] Peter J. M. Van Haastert and Peter N. Devreotes. Chemotaxis: signalling the way forward. *Nat Rev Mol Cell Biol*, **5**, 626–634, Aug 2004.

[75] Peter Devreotes and Alan Rick Horwitz. Signaling networks that regulate cell migration. *Cold Spring Harbor perspectives in biology*, **7**(8), 8 2015.

[76] Anna Huttenlocher. Cell polarization mechanisms during directed cell migration. *Nat Cell Biol*, **7**, 336–337, Apr 2005.

[77] Yoshio Fukui. Mechanistics of amoeboid locomotion: Signal to forces. *Cell Biology International*, **26**(11), 933–944, 2002.

[78] D. Humphrey, C. Duggan, D. Saha, D. Smith, and J. Käs. Active fluidization of polymer networks through molecular motors. *Nature*, **416**, 413–416, Mar 2002.

[79] Peter Friedl and Stephanie Alexander. Cancer invasion and the microenvironment: Plasticity and reciprocity. *Cell*, **147**(5), 992 – 1009, 2011.

[80] GregoryF. Weber, MaureenA. Bjerke, and DouglasW. DeSimone. A mechanoresponsive cadherin-keratin complex directs polarized protrusive behavior and collective cell migration. *Developmental Cell*, **22**(1), 104 – 115, 2012.

[81] Paul Martin and Susan M. Parkhurst. Parallels between tissue repair and embryo morphogenesis. *Development*, **131**(13), 3021–3034, 2004.

[82] Lilianna Solnica-Krezel. Conserved patterns of cell movements during vertebrate gastrulation. *Current Biology*, **15**(6), R213 – R228, 2005.

[83] M. Poujade, E. Grasland-Mongrain, A. Hertzog, J. Jouanneau, P. Chavrier, B. Ladoux, A. Buguin, and P. Silberzan. Collective migration of an epithelial monolayer in response to a model wound. *Proceedings of the National Academy of Sciences*, **104**(41), 15988–15993, 2007.

[84] Geneviève Chazal, Pascale Durbec, Aleksandar Jankovski, Geneviève Rougon, and Harold Cremer. Consequences of neural cell adhesion molecule deficiency on cell migration in the rostral migratory stream of the mouse. *Journal of Neuroscience*, **20**(4), 1446–1457, 2000.

[85] Romaric Vincent, Elsa Bazellières, Carlos Pérez-González, Marina Uroz, Xavier Serra-Picamal, and Xavier Trepat. Active tensile modulus of an epithelial monolayer. *Physical Review Letters*, **115**, 248103, Dec 2015.

[86] Jae Hun Kim, Xavier Serra-Picamal, Dhananjay T. Tambe, Enhua H. Zhou, Chan Young Park, Monirosadat Sadati, Jin-Ah Park, Ramaswamy Krishnan, Bomi Gweon, Emil Millet, James P. Butler, Xavier Trepat, and Jeffrey J. Fredberg. Propulsion and navigation within the advancing monolayer sheet. *Nature Materials*, **12**, 856–863, Jun 2013.

[87] L.D. Landau and E.M. Lifshitz. *Theory of Elasticity (Third Edition)*, volume 7. Butterworth-Heinemann, 1986.

[88] Jacob Notbohm, Shiladitya Banerjee, KazageJ.C. Utuje, Bomi Gweon, Hwanseok Jang, Yongdoo Park, Jennifer Shin, JamesP. Butler, JeffreyJ. Fredberg, and M.Cristina Marchetti. Cellular contraction and polarization drive collective cellular motion. *Biophysical Journal*, **110**(12), 2729 – 2738, 2016.

[89] Pilhwa Lee and Charles W. Wolgemuth. Crawling cells can close wounds without purse strings or signaling. *PLOS Computational Biology*, **7**(3), 1–8, 03 2011.

[90] Markus Basan, Jens Elgeti, Edouard Hannezo, Wouter-Jan Rappel, and Herbert Levine. Alignment of cellular motility forces with tissue flow as a mechanism for efficient wound healing. *Proceedings of the National Academy of Sciences*, **110**(7), 2452–2459, 2013.

[91] S. Banerjee and M. C. Marchetti. Substrate rigidity deforms and polarizes active gels. *EPL (Europhysics Letters)*, **96**(2), 28003, 2011.

[92] Peter Atkins. *The Laws of Thermodynamics: A Very Short Introduction*. Oxford University Press, New York, USA, 2010.

[93] PatrickW. Oakes, Shiladitya Banerjee, M.Cristina Marchetti, and MargaretL. Gardel. Geometry regulates traction stresses in adherent cells. *Biophysical Journal*, **107**(4), 825 – 833, 2014.

[94] Marco Salm and L M Pismen. Chemical and mechanical signaling in epithelial spreading. *Physical Biology*, **9**(2), 026009, 2012.

[95] David P. Stonko, Lathiena Manning, Michelle Starz-Gaiano, and Bradford E. Peercy. A mathematical model of collective cell migration in a three-dimensional, heterogeneous environment. *PLOS ONE*, **10**(4), 1–19, 04 2015.

[96] B. Szabó, G. J. Szöllösi, B. Gönci, Zs. Jurányi, D. Selmeczi, and Tamás Vicsek. Phase transition in the collective migration of tissue cells: Experiment and model. *Phys. Rev. E*, **74**, 061908, Dec 2006.

[97] Michael J. Plank and Matthew J. Simpson. Models of collective cell behaviour with crowding effects: comparing lattice-based and lattice-free approaches. *Journal of The Royal Society Interface*, **9**(76), 2983–2996, 2012.

[98] Robert T. Tranquillo and J.D. Murray. Continuum model of fibroblast-driven wound contraction: Inflammation-mediation. *Journal of Theoretical Biology*, **158**(2), 135 – 172, 1992.

[99] Anna Q. Cai, Kerry A. Landman, and Barry D. Hughes. Multi-scale modeling of a wound-healing cell migration assay. *Journal of Theoretical Biology*, **245**(3), 576 – 594, 2007.

[100] Shirley Mark, Roie Shlomovitz, Nir S. Gov, Mathieu Poujade, Erwan Grasland-Mongrain, and Pascal Silberzan. Physical model of the dynamic instability in an expanding cell culture. *Biophysical Journal*, **98**(3), 361 – 370, 2010.

[101] Kruse, K., Joanny, J. F., Jülicher, F., Prost, J., and Sekimoto, K. Generic theory of active polar gels: a paradigm for cytoskeletal dynamics. *Eur. Phys. J. E*, **16**(1), 5–16, 2005.

[102] Justin S. Bois, Frank Jülicher, and Stephan W. Grill. Pattern formation in active fluids. *Phys. Rev. Lett.*, **106**, 028103, Jan 2011.

[103] M. C. Marchetti, J. F. Joanny, S. Ramaswamy, T. B. Liverpool, J. Prost, Madan Rao, and R. Aditi Simha. Hydrodynamics of soft active matter. *Rev. Mod. Phys.*, **85**, 1143–1189, Jul 2013.

[104] K. Vijay Kumar, Justin S. Bois, Frank Jülicher, and Stephan W. Grill. Pulsatory patterns in active fluids. *Phys. Rev. Lett.*, **112**, 208101, May 2014.

[105] Shiladitya Banerjee and M. Cristina Marchetti. Instabilities and oscillations in isotropic active gels. *Soft Matter*, **7**, 463–473, 2011.

[106] M.H. Kpf and L.M. Pismen. Non-equilibrium patterns in polarizable active layers. *Physica D: Nonlinear Phenomena*, **259**, 48 – 54, 2013.

[107] Xavier Trepat, Michael R. Wasserman, Thomas E. Angelini, Emil Millet, David A. Weitz, James P. Butler, and Jeffrey J. Fredberg. Physical forces during collective cell migration. *Nature Physics*, **5**, 426–430, May 2009.

[108] M. Deforet, V. Hakim, H.G. Yevick, G. Duclos, and P. Silberzan. Emergence of collective modes and tri-dimensional structures from epithelial confinement. *Nature Communications*, **5**, 3747, May 2014.

[109] Dhananjay T. Tambe, C. Corey Hardin, Thomas E. Angelini, Kavitha Rajendran, Chan Young Park, Xavier Serra-Picamal, Enhua H. Zhou, Muhammad H. Zaman, James P. Butler, David A. Weitz, Jeffrey J. Fredberg, and Xavier Trepat. Collective cell guidance by cooperative intercellular forces. *Nature Materials*, **10**, 469–475, May 2011.

[110] Shiladitya Banerjee, Kazage J. C. Utuje, and M. Cristina Marchetti. Propagating stress waves during epithelial expansion. *Physical Review Letters*, **114**, 228101, Jun 2015.

[111] Alexandre J. Kabla. Collective cell migration: leadership, invasion and segregation. *Journal of The Royal Society Interface*, **9**(77), 3268–3278, 2012.

[112] Juliane Zimmermann, RyanL. Hayes, Markus Basan, JosN. Onuchic, Wouter-Jan Rappel, and Herbert Levine. Intercellular stress reconstitution from traction force data. *Biophysical Journal*, **107**(3), 548 – 554, 2014.

[113] Dhananjay T. Tambe, Ugo Croutelle, Xavier Trepat, Chan Young Park, Jae Hun Kim, Emil Millet, James P. Butler, and Jeffrey J. Fredberg. Monolayer stress microscopy: Limitations, artifacts, and accuracy of recovered intercellular stresses. *PLOS ONE*, **8**(2), 1–12, 02 2013.

[114] Assaf Zaritsky, Erik S. Welf, Yun-Yu Tseng, M. Angeles Rabadn, Xavier Serra-Picamal, Xavier Trepat, and Gaudenz Danuser. Seeds of locally aligned motion and stress coordinate a collective cell migration. *Biophysical Journal*, **109**(12), 2492 – 2500, 2015.

[115] Kai Dierkes, Angughali Sumi, Jérôme Solon, and Guillaume Salbreux. Spontaneous oscillations of elastic contractile materials with turnover. *Phys. Rev. Lett.*, **113**, 148102, Oct 2014.

[116] James P. Butler, Iva Marija Tolić-Nørrelykke, Ben Fabry, and Jeffrey J. Fredberg. Traction fields, moments, and strain energy that cells exert on their surroundings. *American Journal of Physiology - Cell Physiology*, **282**(3), C595–C605, 2002.

[117] Juan C. del Alamo, Ruedi Meili, Baldomero Alonso-Latorre, Javier Rodrguez-Rodrguez, Alberto Aliseda, Richard A. Firtel, and Juan C. Lasheras. Spatio-temporal analysis of eukaryotic cell motility by improved force cytometry. *Proceedings of the National Academy of Sciences*, **104**(33), 13343–13348, 2007.

[118] Bo Li and SeanX. Sun. Coherent motions in confluent cell monolayer sheets. *Biophysical Journal*, **107**(7), 1532 – 1541, 2014.

[119] Aaron F. Mertz, Shiladitya Banerjee, Yonglu Che, Guy K. German, Ye Xu, Callen Hyland, M. Cristina Marchetti, Valerie Horsley, and Eric R. Dufresne. Scaling of traction forces with the size of cohesive cell colonies. *Phys. Rev. Lett.*, **108**, 198101, May 2012.

[120] Louis C. Martineau and Phillip F. Gardiner. Insight into skeletal muscle mechanotransduction: Mapk activation is quantitatively related to tension. *Journal of Applied Physiology*, **91**(2), 693–702, 2001.

[121] Cynthia T. Hsu, Danica F. Patton, Ralph E. Mistlberger, and Andrew D. Steele. Palatable meal anticipation in mice. *PLOS ONE*, **5**(9), 1–13, 09 2010.

[122] Yutaka Matsubayashi, Miki Ebisuya, Sakiko Honjoh, and Eisuke Nishida. {ERK} activation propagates in epithelial cell sheets and regulates their migration during wound healing. *Current Biology*, **14**(8), 731 – 735, 2004.

[123] Djordje L. Nikolić, Alistair N. Boettiger, Dafna Bar-Sagi, Jeffrey D. Carbeck, and Stanislav Y. Shvartsman. Role of boundary conditions in an experimental model of epithelial wound healing. *American Journal of Physiology - Cell Physiology*, **291**(1), C68–C75, 2006.

[124] Xavier Trepat, Linhong Deng, Steven S. An, Daniel Navajas, Daniel J. Tschumperlin, William T. Gerthoffer, James P. Butler, and Jeffrey J. Fredberg. Universal physical responses to stretch in the living cell. *Nature*, **447**, 592–595, May 2007.

[125] Ramaswamy Krishnan, Chan Young Park, Yu-Chun Lin, Jere Mead, Richard T. Jaspers, Xavier Trepat, Guillaume Lenormand, Dhananjay Tambe, Alexander V. Smolensky, Andrew H. Knoll, James P. Butler, and Jeffrey J. Fredberg. Reinforcement versus fluidization in cytoskeletal mechanoresponsiveness. *PLOS ONE*, **4**(5), 1–8, 05 2009.

[126] Ramaswamy Krishnan, Elizabeth Peruski Canović, Andreea L. Iordan, Kavitha Rajendran, Greeshma Manomohan, Athanassios P. Pirentis, Michael L. Smith, James P. Butler, Jeffrey J. Fredberg, and Dimitrije Stamenović. Fluidization, resolidification, and reorientation of the endothelial cell in response to slow tidal stretches. *American Journal of Physiology - Cell Physiology*, **303**(4), C368–C375, 2012.

[127] P. G. de Gennes and J. Prost. *The Physics of Liquid Crystals*. Clarendon Press, Oxford, UK, 1995.

[128] Tamal Das, Kai Safferling, Sebastian Rausch, Niels Grabe, Heike Boehm, and Joachim P. Spatz. A molecular mechanotransduction pathway regulates collective migration of epithelial cells. *Nature Cell Biology*, **17**, 276–287, Feb 2015.

[129] Johannes Schindelin, Ignacio Arganda-Carreras, Erwin Frise, Verena Kaynig, Mark Longair, Tobias Pietzsch, Stephan Preibisch, Curtis Rueden, Stephan Saalfeld, Benjamin Schmid, Jean-Yves Tinevez, Daniel James White, Volker Hartenstein, Kevin Eliceiri, Pavel Tomancak, and Albert Cardona. Fiji: an open-source platform for biological-image analysis. *Nature Methods*, **9**, 676–682, Jun 2007.

[130] Katrina K. Treloar and Matthew J. Simpson. Sensitivity of edge detection methods for quantifying cell migration assays. *PLOS ONE*, **8**(6), 1–10, 06 2013.

KAZAGE J. CHRISTOPHE UTUJE

1302 Ivy Ridge Road, Apt 12 ◇ Syracuse, NY 13210
(315) · 289 · 5570 ◇ kutuje@syr.edu

EDUCATION

Syracuse University, New York *August 2011 - August 2017*
Ph.D in Theoretical Soft Matter and Biological Physics
Advisor: Prof. M. Cristina Marchetti

African Institute for Mathematical Sciences, Cape Town/S. Africa *August 2010 - June 2011*
Post Graduate Diploma in Mathematical Sciences
Grade: Distinction
Thesis : *Nanoscale Sensors Using Graphene and Carbon Nanotubes*
Advisor: Prof. Willem Jacobus Perold

National University of Rwanda, Butare/Rwanda *January 2005 - November 2008*
Bachelor of Science in Physics
Grade: Distinction
Thesis : *Résolution Numérique du Système d'Equations de Navier Stokes pour Etudier l'Ecoulement Visqueux d'un Fluide Incompressible de Couette.*
Advisor: Prof. Fidèle Ndahayo

TEACHING EXPERIENCE

Syracuse University August 2014 - May 2017
Teaching Assistant of General Physics I & II *Syracuse, NY*

· Taught General Physics I Recitations for 80+ students from various STEM majors and General Physics II Recitations for an average of fifteen students per semester from Honors & Majors Program.
· Evaluated students by grading their homework, quizzes and exams.
· Scheduled regular one-on-one meetings with students to assist with homework and class material.
· Gave lectures to students in General Physics II on several occasions.
· Tutored students from various majors taking classes in the Physics department, as part of the Physics Clinic Program.

Syracuse University August 2011 - May 2013
Teaching Assistant of Astronomy *Syracuse, NY*

· Prepared Astronomy labs and taught hundreds of students with various skill levels, including non-science majors.
· Evaluated students by grading their lab reports and exams.
· Co-organized teaching assistant lab meetings to discuss lab set-up with other teaching assistants.
· Tutored students from various majors taking classes in the Physics department, as part of the Physics Clinic Program.

Agahozo Shalom Youth Village February 2010 - August 2010
High School Teacher for Physics *Rwamagana, Rwanda*

· Developed a special Physics curriculum for under-privileged 10th and 11th graders who were in danger of dropping out.
· Taught Physics for hundreds of students in 10th and 11th grade.
· Personally mentored tens of high school students.

Lycée Notre Dame de Cîteaux February 2009 - February 2010
High School Teacher for Physics and Mathematics *Kigali, Rwanda*

· Taught Mathematics for 60+ students in 10th grade and Physics for hundreds of students in 11th and 12th grade.
· Created a school choir for an all girls school as part of extra-curricular activities.

RESEARCH EXPERIENCE

Syracuse University May 2013 - July 2017
Research Assistant in Prof. Marchetti's Group *Syracuse, NY*

· Designed a minimum viscoelastic model to describe the mechanical response of adherent single cells to step strain.
· Modified an existent computational algorithm in C to model collective cell migration in expanding and confined cell monolayers.
· Created scripts in Mathematica, Matlab and Python to analyze data collected from various models.
· Presented results in weekly group meetings and in regional and international conferences.
· Collaborated with theorists and experimentalists to study collective cell migration and viscoelastic cell responses upon substrate stretching.

Stellenbosch University February 2011 - June 2011
Research Assistant in Prof. Perold's Lab *Cape Town, South Africa*

· Gave an in-depth review of how graphene and carbon nanotube sensing devices are fabricated, their possible application and how they are tested.
· Fabricated a graphene film sensor by self-assembly approach and analyzed its surface using Atomic Force Microscope and Scanning Electron Microscope.

PUBLICATIONS

Published

· Cellular contraction and polarization drive collective cellular motion. J. Notbohm, S. Banerjee, K.J.C. Utuje, B. Gweon, H. Jang, Y. Park, J. Shin, J.P. Butler, J.J. Fredberg, M.C. Marchetti, *Biophysical journal, 110 (12), 2729-2738, 2016.*
· Propagating stress waves during epithelial expansion. S. Banerjee, K.J.C. Utuje, M.C. Marchetti, *Physical review letters, 114(22), 228101, 2015* (**Selected as editor's choice**).
· Two stand-out models of physics education and outreach in South Africa. A. Marais, K.J.C. Utuje, A. Sajadi, *Physics Today, 19 February 2015.*

In Preparation

· Viscoelastic response of adherent cells to substrate deformation . R. Boltyanskiy, K.J.C. Utuje, K. A. Rosowski, E.R. Dufresne, M.C. Marchetti

PRESENTATIONS

2016 · Poster at Active and Smart Matter International Conference, held in Syracuse, NY: *Mechanical Coordination in Epithelial Monolayers.*

2016 · Contributed talk at American Physical Society March Meeting in Baltimore, MD: *Cellular Polarization and Contraction in Collective Cell Migration.*

2015 · Poster at Soft Interface IGERT Retreat in Syracuse, NY: *Mechanical Coordination in Epithelial Monolayers*

2015 · Poster at Boulder Summer School on Soft Matter In and Out of Equilibrium in Boulder, CO: *Mechanical Coordination in Epithelial Monolayers.*

2015 · Contributed talk at American Physical Society March Meeting in San Antonio, TX: *Propagating Stress Waves in Spreading and Confined Cell Monolayers.*

2014 · Poster and Contributed talk at Inter-Continental Advanced Materials for Photonics (I-CAMP) Summer School on Geometry and Topology in Soft Matter in Cape Town, South Africa: *Wave Propagation in Expanding Cell Layers.*

2014 · Poster at Soft Interface IGERT Retreat in Syracuse, NY: *Wave Propagation in Expanding Cell Layers.*

2014 · Contributed talk at American Physical Society March Meeting in Denver, CO: *Wave Propagation in Expanding Cell Layers.*

2013 · Poster at Stevenson Biomaterials Lecture Series in Syracuse, NY: *Collective Motility of Migrating Cell Layers* (**Third Best Poster Award Winner**).

2013 · Poster at Soft Solids and Complex Fluids Summer School in Amherst, MA: *Collective Motility of Migrating Cell Layers.*

TECHNICAL STRENGTHS

Programming Languages	Python, C
Software	Matlab, Octave, Mathematica, R, Sage, LaTeX, Linux.

SCHOLARSHIPS, AWARDS AND DISTINCTIONS

2016 · APS March Meeting Travel Grant by Syracuse University

2015 · Shirley Chan Student Travel Award, Division of Biological Physics of American Physical Society.

2015 · Boulder Summer School Fellowship, University of Colorado.

2015 · APS March Meeting Travel Grant by Syracuse University

2014 · I-CAMP Fellowship, Stellenbosch University, South Africa.

2014 · APS March Meeting Travel Grant by Syracuse University

2013 · UMass Summer School Fellowship, University of Massachusetts Amherst.

2013 · Third Best Poster Presentation Award, Syracuse Biomaterials Institute.

2013 · APS March Meeting Travel Grant by Syracuse University

2011 · Stephen Hawking Scholarship for outstanding academic achievement in Physics, African Institute for Mathematical Sciences.

2011 · PI Scholarship, Perimeter Institute, declined

2005-2008 · Academic Excellence Scholarship, Student Financing Agency for Rwanda.

1997 · Top Student Countrywide in National Examinations for Primary Level.

LEADERSHIP EXPERIENCE

2007-2008 · Vice Representative, Student Body at the Faculty of Sciences - National University of Rwanda.

2002-2003 · Unit Leader, Scout Organization - Petit Seminaire Saint Léon de Kabgayi.

LANGUAGES

English · Fluent

French · Fluent

Kinyarwanda · Fluent